

ALMA MATER STUDIORUM - UNIVERSITY OF BOLOGNA

School of Science
Department of physics and astronomy
Master Degree Program in Astrophysics and Cosmology

Reconstructing the history of Terzan 5 through hydrodynamical N -body simulations

Graduation Thesis

Presented by:

Marco Gherardelli

Supervisor:

Chiar.mo Prof. F. R. Ferraro

Co-supervisors:

Dr. F. Calura

Dr. R. Pascale

Academic Year 2023/2024

Graduation date 27/03/2025 - Session V

*Yes, and how many years must a mountain exist
Before it is washed to the sea?
And how many years can some people exist
Before they're allowed to be free?
Yes, and how many times can a man turn his head
And pretend that he just doesn't see?*

Blowin' In The Wind, Bob Dylan (1962)

Abstract

The discovery of the complex stellar populations hosted in two massive stellar systems in the Galactic Bulge, namely Terzan 5 and Liller 1, posed intriguing questions about their origin and their possible connection with the formation and early evolution of the Bulge itself. Indeed, despite their Globular Cluster appearance, the fact that they host subpopulations with significantly different ages (several Gyrs) and metallicities (about 1 dex) potentially indicates that these stellar systems could not be genuine globular, which conversely are characterized by a single age and minor (if any) metallicity spread. These surprising properties can be naturally explained in the context of the self-enrichment scenario, thus opening the fascinating possibility that they could be the remnants of primordial massive structures capable of retaining supernova ejecta within their potential well. At the moment a few alternative hypotheses about their origin have been suggested in the literature. However, while some of them have been naturally discarded by the discovered properties of these two systems, a viable alternative possibility remains: a massive genuine Globular Cluster that accreted a Giant Molecular Cloud.

The specific aim of this thesis is to explore the scenario in the case of Terzan 5 using a customized version of the high-resolution hydrodynamical N -body code, called RAMSES [Teyssier \(2002\)](#). The simulation setup follows the "wind-tunnel" scheme as implemented in [Calura et al. \(2019\)](#), where a Giant Molecular Cloud within the Milky Way's Galactic Bulge interacts with a self-gravitating stellar system (the proto-Terzan 5) situated in a medium with physical conditions similar to those of the Bulge. The simulations implement three key physical processes: star formation, using the classical criteria implemented in RAMSES [Rasera & Teyssier \(2006\)](#) coupled with the star formation model adopted by [Calura et al. \(2022, 2024\)](#); a star-by-star feedback model; and a cooling model.

The main result of this work is that, independently on the initial mass of the accreting star cluster and the velocity infall of the GMC, the mass of the new stellar population formed from the accretion of the Cloud always remains orders of magnitude below the mass of the young sub-population observed in Terzan 5, thus severely challenging the hypothesis that this could be the formation channel of this stellar system.

Contents

1	Introduction	1
1.1	General properties of genuine globular clusters	2
1.2	Terzan 5: a complex stellar system in the Galactic Bulge	6
1.3	A new class of stellar systems?	13
1.4	Terzan 5 Formation Scenarios	17
1.5	Aim of this Thesis	21
2	Numerical methods	23
2.1	Numerical methods for Hydrodynamics	24
2.1.1	Eulerian codes	25
2.1.2	Lagrangian codes	26
2.2	Numerical methods in RAMSES	29
2.2.1	Adaptive Mesh Refinement	30
2.2.2	Gravity and Particle methods	32
2.2.3	Gravitational solver in RAMSES	36
2.2.4	Hydrodynamics in RAMSES	38
2.2.5	Time step constraints	39
3	Simulations set-up	41
3.1	Star formation, stellar feedback models and gas cooling	42
3.1.1	Star formation	42
3.1.2	The role of the star formation efficiency	44
3.1.3	Stellar Feedback	45
3.1.4	Cooling prescriptions	46
3.2	Initial conditions	49
3.2.1	Gas	49
3.2.2	FG Stars	53

3.2.3	Generation of the FG stars	55
3.3	Simulation parameters	59
3.3.1	Resolution	59
3.3.2	Physical parameters	60
3.3.3	Tests	61
4	Results	69
4.1	Simulation model M6	70
4.1.1	Gas Evolution Maps in the M6-v10-L8 model	71
4.1.2	Gas Evolution Maps in the M6-v20-L8 model	74
4.1.3	Density and cumulative mass profiles	76
4.1.4	SFHs	77
4.2	Simulation model M7	80
4.2.1	Gas Evolution Maps in the M7-v10-L8 model	80
4.2.2	Gas Evolution Maps in the M7-v20-L8 model	81
4.2.3	Density and cumulative mass profiles	83
4.2.4	SFHs	85
4.3	Lower resolution models	87
4.4	Limitation of the model	89
4.5	Comparison with McKenzie & Bekki (2018)	91
5	Conclusions	95
5.1	Summary	95
5.2	Conclusions	96
5.3	Future perspectives	97

Chapter *1*

Introduction

In this chapter, I present the main topics of the thesis, offering a concise overview of the main properties of genuine globular clusters (GCs; Section 1.1). Next, I describe the discovery and properties of the peculiar stellar system Terzan 5 in the Galactic Bulge (Section 1.2) and discuss this discovery in the context of the definition of a new class of stellar systems (the “Bulge Fossil Fragments”, BFFs) highlighting their unique traits (Section 1.3; Ferraro et al., 2021). Finally, I review the possible formation scenarios for Terzan 5 and outline the main motivations and the aim of this thesis (Section 1.4).

1.1 General properties of genuine globular clusters

Most stars were born within stellar clusters or other types of stellar aggregates, such as groups (Lada & Lada, 2003; Rodríguez et al., 2020). In general, stellar clusters are divided into two categories: GCs and open clusters (OCs). OCs are groups of young, loosely bound stars, typically containing from 10^2 to 10^3 members, and are mostly found in the disc of spiral galaxies. The lack of old OCs results from dynamical effects, as their weak gravitational pull makes them easy to break apart, a key effect in their evolution known as *infant mortality effect*. On the contrary, GCs are more massive, denser, and dynamically stable systems, held together by a deeper gravitational potential well. The Milky Way (MW) hosts around 160 GCs. As an example, in Figure 1.1, I show Hubble Space Telescope (HST) observations of a selection of 9 Galactic GCs, with masses ranging from 10^4 to a few $10^6 M_\odot$ and an average mass of $2 \times 10^5 M_\odot$. Assuming an average stellar mass value of $0.5 M_\odot$, this corresponds to approximately 10^{5-6} stars. Most GCs in the MW are ranking among the oldest objects in the galaxy, older than 10 Gyr, with ages that approach the Hubble time. The majority of the GCs are associated with the MW's halo and they are mainly metal-poor ($-2.5 \leq [\text{Fe}/\text{H}]^1 \leq -0.8$) and old stellar populations. A distinct population of GCs is associated with the Galactic Disc/Bulge, characterised by higher metallicities ($[\text{Fe}/\text{H}] \geq -0.8$) compared to the Halo population. About 30% of the total population of Galactic GCs is located in the Bulge. The Bulge is one of the least accessible regions in the MW and its structure, formation and evolution are still the subject of intense debate (see, for example, Rich, 1998; Ness et al., 2013a; Origlia, 2014; Zoccali & Valenti, 2016). The Galactic Bulge contains about one-quarter ($6 \times 10^{10} M_\odot$) of the total stellar mass of the MW and represents the oldest massive component of the Galaxy, made of 12 – 13 Gyr old stars. Understanding its structure and the properties of its stellar population is therefore of great relevance for all the theoretical models that aim at describing how the MW bulge and any galaxy spheroid formed and evolved with cosmic time.

The long-standing idea that GCs are Simple Stellar Populations, where all stars form simultaneously from a single burst and share nearly identical chemical compo-

¹The abundance of an element X is expressed as $[\text{X}/\text{H}] = \log(\text{X}/\text{H})_\star - \log(\text{X}/\text{H})_\odot$. The iron abundance is generally used as an indicator of the metallicity, i.e., the abundance of all elements heavier than He.

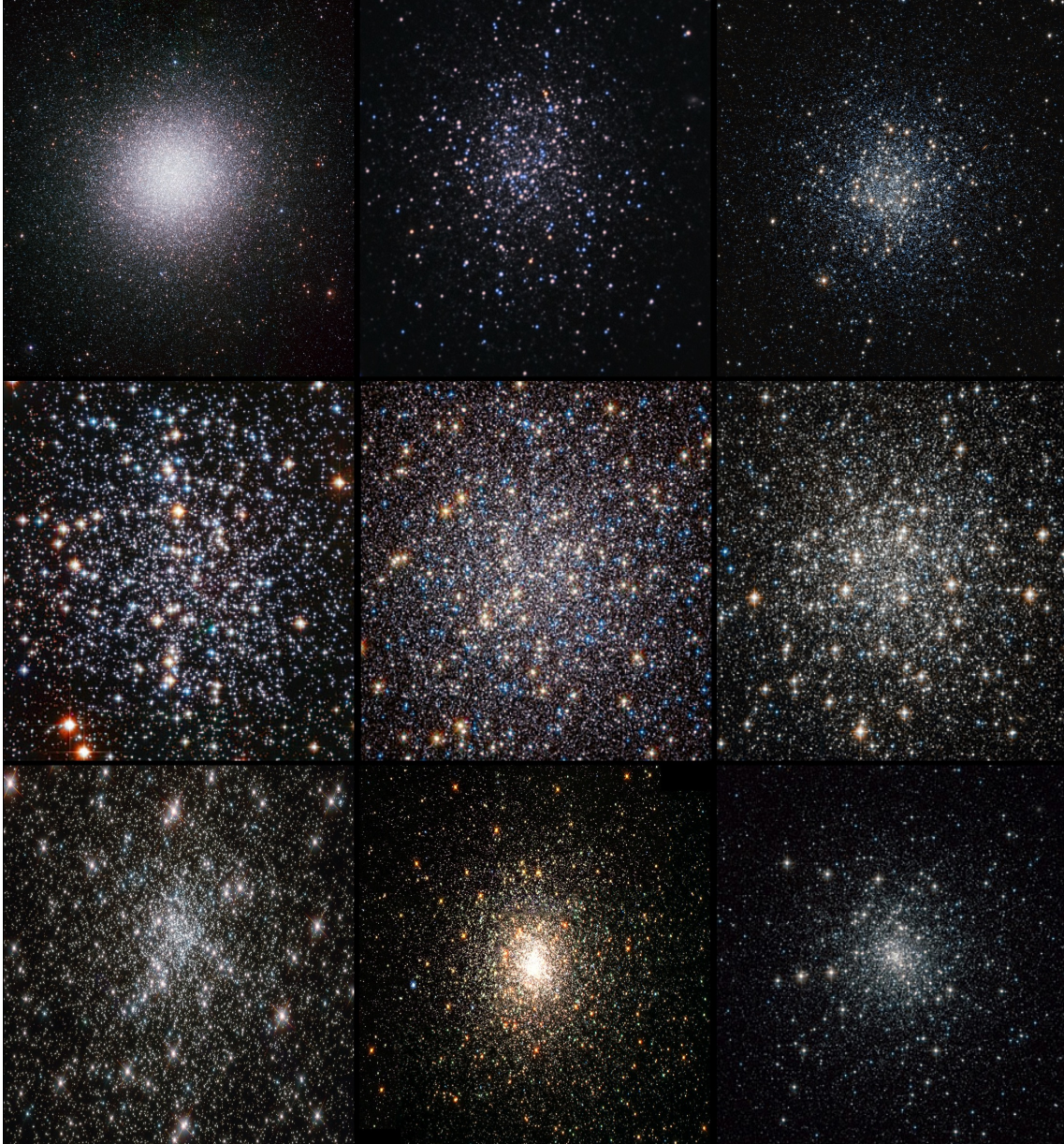


Figure 1.1: Mosaic of images of 9 GCs ranked in order of increasing dynamical age. From top-left to bottom-right: omega Centauri, NGC 288, M55, M4, M13, M10, NGC6752, M80, M30. Credits to http://www.cosmic-lab.eu/Cosmic-Lab/image_gallery.html.

sitions except for minor variations, has been overturned (Renzini & Buzzoni, 1986). It is now well established that GCs exhibit significant complexity, with many showing substantial variations in stellar abundances. In particular, spectroscopic studies have revealed that while stars in GCs generally have uniform iron content, they display star-to-star differences in the abundances of light elements such as C, N, O, Na, Mg, and Al. These variations, known as Light-Element Multi Populations (LE-MPs), challenge the traditional view of GCs as chemically homogeneous sys-

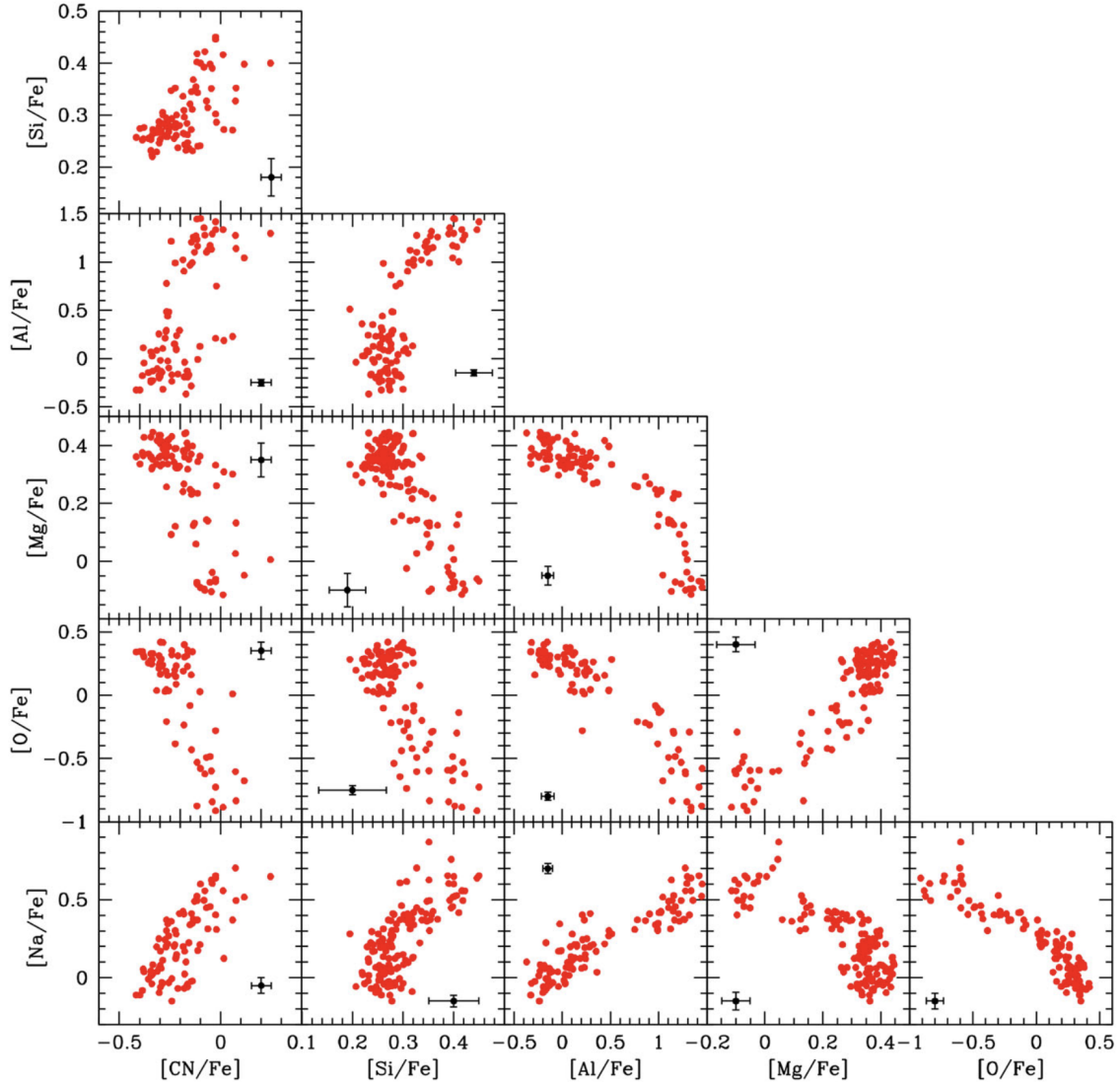


Figure 1.2: (Anti)correlations of light elements in Red Giant Branch stars (RGB) of the GC NGC 2808. Image from Gratton et al. (2019). Data of O, Na, Si and Mg are from Carretta (2015) and Al, CN from Carretta et al. (2018).

tems (Gratton et al., 2004; Carretta et al., 2009a,b,c; Gratton et al., 2012, 2019). Ground-based spectroscopy of thousands of stars in GCs has mapped detailed abundance patterns, while space-based photometric observations, including observations of Galactic GCs from the HST have demonstrated that LE-MP can be efficiently distinguished adopting appropriate photometric bands (Massari et al., 2015) and Gaia (Baumgardt et al., 2019). This demonstrates that essentially all genuine GCs exhibit a consistent pattern of stellar population enrichment, characterized by enhancements in He, N, and Na, and depletions in O and C, regardless of the Galactic component to which the cluster belongs (Halo, Disc, or Bulge). As a result, these

chemical anomalies are not randomly distributed but follow well-defined anticorrelations, in Figure 1.2 are reported some of these (anti)correlations observed in RGB stars.

One of the commonly accepted scenarios to explain the origin of the LE-MP is the self-enrichment scenario, according to that the First Generation (FG) stars have polluted the system with chemically enriched gas that is subsequently used to form a Second Generation (SG) of stars. Several theoretical models have been proposed to explain this process, considering different mechanisms responsible for the pollution, including the AGB scenario (D’Ercole et al., 2008; Calura et al., 2019; Lacchin et al., 2021; Yaghoobi et al., 2022a), the Fast Rotating Massive Stars scenario (FRMS; Decressin et al., 2007; Krause et al., 2013), the Massive Interacting Binary (MIB) scenario (de Mink et al., 2009), and the Super Massive Star (SMS) scenario (Denissenkov & Hartwick, 2014). Furthermore, the James Webb Space Telescope (JWST) is now providing crucial follow-up data, facilitating studies of high-redshift galaxies (Vanzella et al., 2021, 2022; Adamo et al., 2024) and delivering unprecedented detail in the examination of local GC populations (Marino et al., 2021). Further insights into the appearance of GCs at the time of their formation have emerged from recent observations of gravitationally lensed fields, as reported by Calura et al. (2022). Characterising high-redshift systems is essential for understanding the formation of GCs, particularly the old clusters like those found in the MW.

However, it is important to summarize here the major properties characterizing genuine GCs:

1. they do show evidence of LE-MP but they are highly homogeneous in iron, hence, no relevant evidence of multi-iron sub-populations (I-MPs) are detected. This suggest that the original potential well in which they formed was not deep enough to retain the high-velocity ejecta from the SN;
2. they do not show any evidence of multi-age populations: this means that (in the case of self-enrichment) the enrichment process occurred very rapidly over a time scale which is not detectable at the main sequence Turnoff (MS-TO)-level ($\leq 10^8$ yrs).

This is key in order to distinguish the genuine GC population from stellar systems that appear as GCs, but show much more complex stellar population. In this respect one famous case in the Galactic Halo is ω Centauri. In fact, despite its original

classification of GC, this stellar system has been found to host I-MPs (Norris et al., 1996; Pancino et al., 2000; Ferraro et al., 2004; Johnson & Pilachowski, 2010; Bellini et al., 2017; Alvarez Garay et al., 2022, 2024), and its properties suggest that it is the remnant of a nuclear star cluster of an accreted dwarf galaxy (Bekki & Freeman, 2003; Romano et al., 2007). Recently, the panorama of complex stellar systems under the appearance of genuine GCs has enriched of new exciting discoveries into the Galactic Bulge.

1.2 Terzan 5: a complex stellar system in the Galactic Bulge

Terzan 5 is a massive stellar system in the Galactic Bulge discovered in 1968 by the French astronomer Agop Terzan. It is situated at a distance of ~ 2 kpc from the Galactic centre in one of the most extincted region of the Galaxy. It exhibits an average colour excess of $E(B-V)$ of approximately 2.38 mag and a differential reddening (DR) that varies across a range of about 0.7 mag (Massari et al., 2012). Terzan 5 has been considered a genuine GC for more than 50 years. However, recent investigations have demonstrated that at odds with genuine GCs (see the previous Section) this stellar system hosts I-MP with large (several Giga-years) age differences.

In fact, a detailed photometric investigation with the HST, combined with high-resolution imaging in the K and J bands obtained using a Multi-Conjugate Adaptive Optics demonstrator instrument, MCAO², at the Very Large Telescope (VLT) of the European Southern Observatory (ESO) (see Ferraro et al., 2009, 2016 and Figure 1.3), has provided compelling evidence for the presence of multiple populations with the identification of two distinct Red Clumps (RC) (Ferraro et al., 2009, 2016). In Figure 1.4 it is shown the DR-corrected (K, I-K) color-magnitude diagram (CMD) of Terzan 5 (top panel), with a focus on the old and young Turnoff regions, along with its metallicity distribution with three peaks and the corresponding $[\alpha/Fe]$ abundance ratio as a function of the iron abundance (bottom panel). The metallicity measured in the two RC stars was again a surprise. The brightest RC was populated by super-solar $[Fe/H] \simeq +0.3$, twice the solar abundance, thus being one of the most metal-rich populations of the entire Galaxy, while the faintest RC was at sub-solar-

²MCAO operates in the near-infrared, enabling detection of stellar radiation that penetrates the dust clouds obscuring the Galactic Bulge.

metallicity ($[\text{Fe}/\text{H}] \simeq -0.3$).

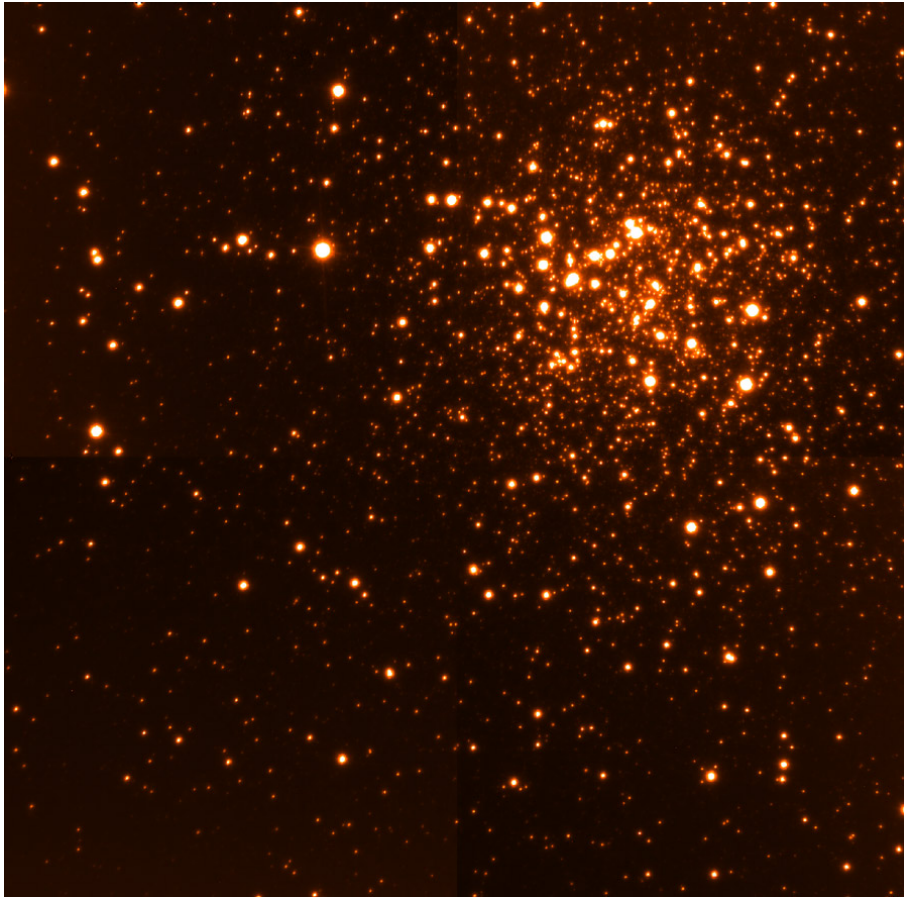


Figure 1.3: K-band image of Terzan 5 from the Multi-Conjugate Adaptive Optics Demonstrator (MAD), a prototype adaptive optics system used to demonstrate the feasibility of different techniques in the framework of the E-ELT and the second generation VLT Instruments. The star colours are from the Hubble image of the same star field. Credits to ESO/F. R. Ferraro.

The super-solar RC stars have been found to be more centrally concentrated than the metal-poor population (Ferraro et al., 2009; Lanzoni et al., 2010; Massari et al., 2015). The quantitative study of the stellar content also provide a direct estimate of the stellar system mass fully confirming that Terzan 5 is a very massive system of about $\sim 2 \times 10^6 M_{\odot}$ (Lanzoni et al., 2010), in agreement with what reported in Baumgardt et al. (2018) ($1.09 \pm 0.8 \times 10^6 M_{\odot}$) and the size of the two components. The metal-rich component has been found to contain a substantial fraction of the cluster mass ($\sim 40\%$) corresponding to $M \sim 8 \times 10^5 M_{\odot}$, the same mass of the GC 47 Tucanae, one of the massive GC in the MW (Marks & Kroupa, 2010). The acquisition of additional HST images allowed the accurate measure of the proper motions, thus performing adequate decontamination from field stars, and provided

the detection of two distinct MS-TO and sub-giant branch (SGB) populations, with the super-solar component to be several Gyr younger than the sub-solar one (Ferraro et al., 2016). As an example, the top panel of Figure 1.4 shows Terzan 5 CMD in the (K,I-K) bands where the old and young Turnoff regions are highlighted with different colors. On the other hand, a massive spectroscopic campaign (Origlia et al., 2011, 2013, 2019; Massari et al., 2014) has fully characterized the chemistry of the system, confirming the existence of two major stellar sub-populations from different formation epochs:

- the older population, 12 ± 1 Gyr old with sub-solar metallicity ($[\text{Fe}/\text{H}] \approx -0.30$ and a $[\alpha/\text{Fe}] \approx +0.30$), formed on a short timescale (< 1 Gyr) with a mass of $1.2 \times 10^6 M_{\odot}$ ($\sim 60\%$ of the total mass of the system);
- the younger population, formed 4.5 ± 0.5 Gyr ago (approximately ~ 7.5 Gyr after the first one) exhibits super-solar metallicity ($[\text{Fe}/\text{H}] \approx +0.30$, $[\alpha/\text{Fe}] \approx +0.03$) with a mass of $8 \times 10^5 M_{\odot}$, accounting for $\sim 40\%$ of the total mass of the system.

Additionally, a minor secondary peak, or tail, is present, associated with the lower-metallicity population, at $[\text{Fe}/\text{H}] \simeq -0.80$ and $[\alpha/\text{Fe}] \simeq +0.36$ (see Origlia et al., 2013, 2019; Massari et al., 2014). The metallicity distribution is shown in the bottom panel of Figure 1.4.

One of the major notable features emerging from the detailed spectroscopic investigation of the I-MP in Terzan 5 is the striking chemical similarity with the Galactic Bulge. This is particularly relevant because the atmospheres of the stars that we observe today keep memory of the chemical composition of the interstellar medium (ISM) from which they formed. In turn, the chemical abundances of the ISM vary in time if more than one burst of star formation occurs, owing to the ejecta of each stellar generation. Thus, stars formed at different times in the same system have different chemical compositions, and by analyzing the chemistry of each stellar population, one can univocally trace the enrichment process.

The $[\alpha/\text{Fe}]$ vs $[\text{Fe}/\text{H}]$ pattern is particularly relevant in this respect, since it compares elements that are produced by quite different processes. The α -elements (like O, Mg, etc.) are synthesized by massive stars and released to the ISM over a short timescale (a few million years) by the explosion of core collapse, Type II supernovae (TypeII SNe). The majority of iron-peak elements are, instead, produced in SNeIa explosions that occur over longer timescales. The injection of such a large

amount of iron-peak elements in the ISM implies that the (initially nearly constant) $[\alpha/\text{Fe}]$ ratio set by TypeII SNe starts to decrease when the first generation of SNeIa explodes, thus producing the characteristic "knee" in the $[\alpha/\text{Fe}]$ – $[\text{Fe}/\text{H}]$ diagram, see the distribution in the bottom panel of Figure 1.4.

Therefore, the knee flags the metallicity $[\text{Fe}/\text{H}]$ reached by the ISM (due to SNeII only) at the epoch of the first TypeIa SN explosions. This implies that the $[\alpha/\text{Fe}]$ – $[\text{Fe}/\text{H}]$ pattern is a powerful indicator of the star formation rate (SFR) in the environment where the stars formed: the faster a stellar system forms its stars (high SFR), the larger is the contribution of SNeII to the chemical enrichment before SNeIa explode, thus the larger is the metallicity of the knee in the diagram (Matteucci & Brocato, 1990). The chemical DNA of Terzan 5, as traced by their stellar populations with measured α -element abundance (large squares for Terzan 5 in Figure 1.4), manifestly follows the pattern measured in the Bulge (grey dots from Ness et al., 2013a, Johnson et al., 2014), while it is incompatible with those of the MW Disk/Halo and dwarf galaxies. The result of the chemical test is therefore indisputable: Terzan 5 and the Galactic Bulge share the same chemical DNA, which shows that they experienced the same general chemical enrichment history. In addition, recent measurements of radial velocities and proper motions (PMs) from HST (Massari et al., 2015) and more recently from Gaia (Massari et al., 2018; Baumgardt et al., 2019) allowed to determine the orbital parameters of Terzan 5, finding an apocenter - the farthest point of the orbit with respect to the MW center - of 2.8 kpc. Indeed, the reconstructed orbit of the system in the meridional plane of the MW, as shown in Figure 1.5, turns out to be well confined within the Bulge, showing that Terzan 5 spent its entire life into the Bulge, thus strongly suggesting an in-situ origin rather than an external accretion.

For the sake of completeness, I report in Table 1.1 the fundamental quantities of Terzan 5 that have been used throughout this thesis (see Chapter 3). The data are taken mostly from the following references Valenti et al. (2007), Ferraro et al. (2009), Harris (2010), Lanzoni et al. (2010), Baumgardt & Vasiliev (2021). It is relevant to notice that in the Table are reported the values of the actual mass of the FG as M_{FG} and the mass of the SG as M_{SG} of Terzan 5. These defined values are extremely important to the use of this thesis work, as a reference value to the results presented in Chapter 4.

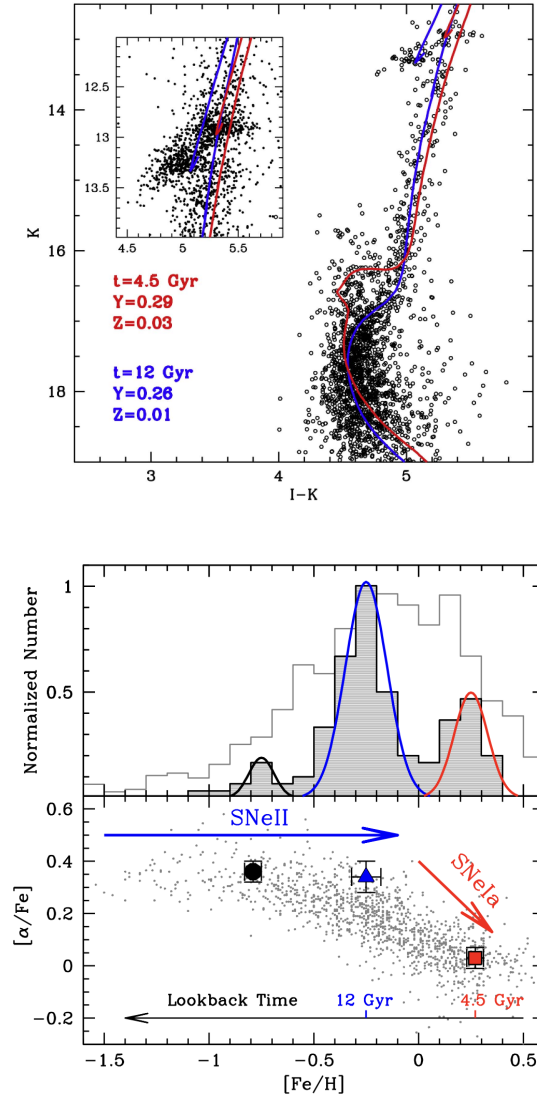


Figure 1.4: Top panel: DR-corrected (K, I-K) CMD of Terzan 5 obtained by combining the deepest VLT-MAD K-band and HST-ACS I-band images. The CMD clearly shows the presence of two distinct MS-TO/SGBs, indicative of two stellar sub-populations with different ages. The blue line traces the 12 Gyr old isochrone of the metal-poor population; the red line traces the younger 4.5 Gyr isochrone of the metal-rich population (super-solar). The inset shows a zoom of the CMD at the Red Clump level, with all the detected stars. Bottom panels: iron distribution of the three sub-populations of Terzan 5 (shaded histogram and coloured lines) compared to that of the Galactic Bulge field stars from the literature (light grey histogram on the background) (Ness et al., 2013b; Johnson et al., 2014); $[\alpha/\text{Fe}]$ - $[\text{Fe}/\text{H}]$ distribution of the three sub-populations of Terzan 5 compared to that of the bulge field stars from the literature (grey dots). Image from Ferraro et al. (2016). The formation epoch of the two major Terzan 5 sub-populations is also labelled.

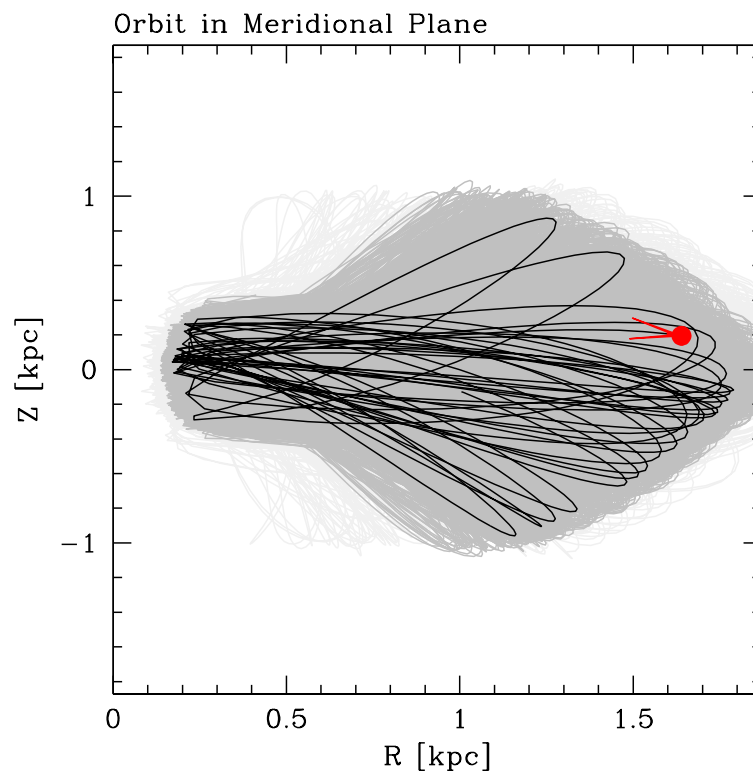


Figure 1.5: Reconstructed orbit of Terzan 5 in the MW meridional plane. The orbit cover the latest 500 Myr. Image from <https://people.smp.uq.edu.au/HolgerBaumgardt/globular>.

Parameter	Value	Reference
Cluster TOTAL Mass, M_{TOT}	$2 \times 10^6 M_{\odot}$	Lanzoni et al. (2010)
Old-population Mass, M_{FG}	$1.2 \times 10^6 M_{\odot}$	Lanzoni et al. (2010)
Young population Mass, M_{SG}	$8 \times 10^5 M_{\odot}$	Lanzoni et al. (2010)
M/L ratio	$3.0 \pm 0.3 M_{\odot}/L_{\odot}$	Maraston (1998)
Central velocity dispersion, σ_0	15.6 km s^{-1}	Baumgardt & Vasiliev (2021)
Distance from Sun, R_{\odot}	$5.9 \pm 0.5 \text{ kpc}$	Valenti et al. (2007)
Galactocentric distance, R_{GC}	$2 \pm 0.13 \text{ kpc}$	Valenti et al. (2007)
Right ascension, α_{J2000}	$17^h 48^m 04.85^s$	Harris (2010)
Declination, δ_{J2000}	$-24^{\circ} 46' 45''$	Harris (2010)
Color excess E(B-V)	2.38 ± 0.055	Valenti et al. (2007)
Half-mass radius, r_h	1.00 pc	Lanzoni et al. (2010)
Core radius, r_c	0.26 pc	Lanzoni et al. (2010)
Concentration, c	1.49 pc	Lanzoni et al. (2010)
Central mass density, ρ_0	$4.1 \times 10^6 M_{\odot}/\text{pc}^3$	Lanzoni et al. (2010)
Age, t_{age}	12 Gyr	Ferraro et al. (2009)

Table 1.1: Table containing the Terzan 5 main characteristics.

1.3 A new class of stellar systems?

Because of its uniqueness, Terzan 5 has been considered for years just a single, isolated, bizarre object. The perspective has completely changed after the discovery (Ferraro et al., 2021) that another GC-like object in the Bulge (Liller 1) hosts two distinct stellar populations with remarkably different ages: 12 Gyr for the oldest one, just 1 – 2 Gyr for the youngest component, which draw a well-populated blue plume (BP) in the CMD (Figure 1.6, left panel) and a more centrally concentrated component than the other populations (Figure 1.6, right panel). As in the case of

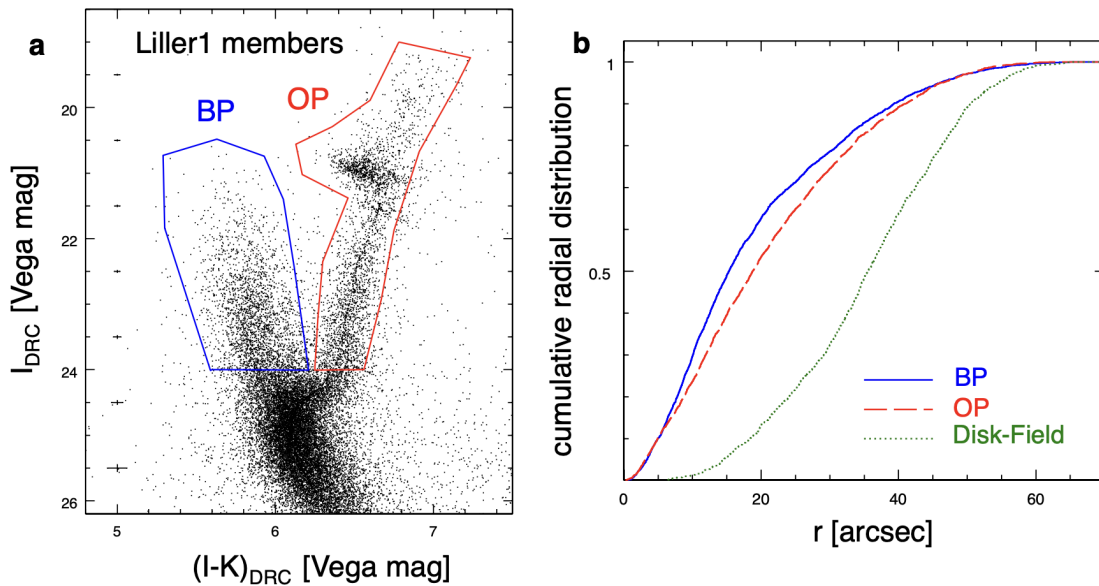


Figure 1.6: The properties of the Liller 1 stellar populations. In the left panel, it is shown the CMD of the PM-selected members of Liller 1 with magnitudes (I_{DRC}) and colours ($(I - K)_{DRC}$) corrected for DR. The selection boxes of the BP (in blue) and old population (in red) used for the study of their radial distribution are also shown. The mean errors (1 standard error of the mean) in magnitude and colour are reported on the left for 1 magnitude-wide bins. In the right panel, instead is shown the Cumulative radial distributions of the three sub-populations observed in the PM-selected CMDs of Liller 1. The number of stars counted in the selected components is: 2480 in the BP, 2916 in the OP, and 1109 in the Disk-Field. Image from Ferraro et al. (2021).

Terzan 5, Liller 1 is also a well-known stellar system, affected by an extinction as large as 10 magnitudes in the optical band, repeatedly observed in the past both from the ground and from space. Once more, only with an appropriate combination of high-resolution HST optical images, and MCAO-corrected NIR observations

(performed this time at the GEMINI South Telescope), we have been able to reveal its complexity: the presence of two distinct stellar populations clearly appeared in the PM-selected and DR-corrected CMDs. The first spectroscopic screening of its central region (obtained with MUSE) showed a clear bimodal iron distribution, with a sub-solar and a super-solar component (see Figure 1.7; Crociati et al., 2023). The

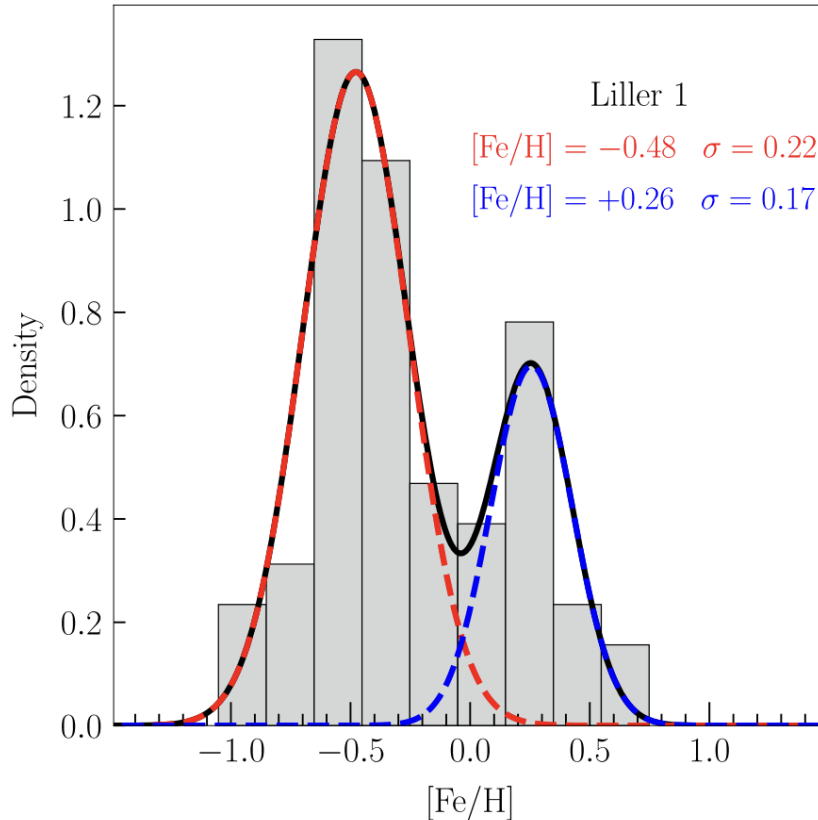


Figure 1.7: Metallicity distribution of Liller 1 obtained with bona fide targets (gray histogram). The solid black line shows the function that best reproduces the observed distribution. It is the combination of the two Gaussian functions shown as red and blue dashed lines and indicating the presence, respectively, of MP and MR subpopulations in Liller 1. The mean $[\text{Fe}/\text{H}]$ values and the standard deviations of the two individual Gaussian components are also labeled in the panel. Image from Crociati et al. (2023).

subsequent spectroscopic campaign allowed to reconstruct the $[\alpha/\text{Fe}]-[\text{Fe}/\text{H}]$ pattern (Alvarez Garay et al., 2024; Fanelli et al., 2024). These findings have finally confirmed the existence of a 12 Gyr-old α -enhanced ($[\alpha/\text{Fe}] \simeq 0.35$) sub-solar component at $[\text{Fe}/\text{H}] \simeq -0.3$ and a very young (1 – 2 Gyr-old) solar-scaled ($[\alpha/\text{Fe}] \simeq 0$) super-solar ($[\text{Fe}/\text{H}] = +0.3$) sub-population. Similarly to the case of Terzan 5 the striking similarity of the $[\alpha/\text{Fe}]-[\text{Fe}/\text{H}]$ abundance pattern with the Bulge field stars strongly supports the deep connection of Liller 1 to the Galactic Bulge. This is also

supported by the reconstructed orbit that testifies that Liller 1 also spent the vast majority of its lifetime into the Bulge.

Thus, as a general result, these evidences demonstrated the deep connection between Liller 1 and Terzan 5: they likely originated at the same epoch (12 Gyr ago) apparently from gas clouds with similar chemistry $[\text{Fe}/\text{H}] \simeq -0.3$, (with $[\alpha/\text{Fe}] \simeq 0.35$) at that time enriched by only TypeII SNe. The observed differences between the young populations detected in the two systems suggest that the subsequent star formation events occurred on different timescales, likely reflecting distinct histories of interactions with the local environment and, potentially, different orbital histories within the Galactic Bulge. However, in both cases the SG of stars was formed by a gas enriched also by TypeIa SNe, as clearly testified by the solar α -enhancement ($[\alpha/\text{Fe}] \simeq 0$). It is important to note that the younger populations, corresponding to the metal-rich ones, are also more centrally concentrated compared to the older populations. These evidences support the self-enrichment scenario, outlined in Section 1.1, potentially confirming that these systems were sufficiently massive to retain SN ejecta. Recent chemical models, specifically computed for the case of Terzan 5 (Romano et al., 2023), have indeed demonstrated that a self-enrichment evolution of a progenitor with a mass of $4 \times 10^7 M_{\odot}$ can nicely reproduce all the observed chemical patterns. Moreover both these peculiar systems display chemical patterns fully consistent with those measured in the Bulge, thus they share the same overall chemical enrichment history.

The genesis of galaxy bulges is still highly debated (e.g., Nataf, 2017) and possibly more complex than previously thought, with a first phase characterized by the merging of primordial massive clumps of gas and stars (like those observed in high-redshift "chain and clumpy galaxies"; e.g., Elmegreen et al., 2009; Genzel et al., 2011) followed by the formation and secular evolution of the disk, bar and other substructures like those currently observed in the Galactic Bulge (see Combes et al., 1990; Zoccali et al., 2014; Wegg et al., 2015). Although most of these massive primordial clumps are predicted to dissolve and form the Bulge, a few of them could have survived the total disruption (Laurikainen et al., 2016) and still be present in the inner regions of the host galaxy, appearing roughly as massive GCs. Despite their appearance as genuine GCs, these fossil relics are also expected to host multi-iron and multi-age sub-populations. Indeed, their progenitors were massive enough to retain the iron-enriched SN ejecta, and they likely experienced multiple bursts of star formation. Terzan 5 and Liller 1 showed exactly these properties, hence they are really ideal candidates to be the BFFs, two fragments of those primordial systems

that 12 Gyr ago contributed to form the Galactic Bulge.

It is also possible that the formation history of these two stellar systems is even more complex with respect to that traced by the sub-populations detected so far in the CMDs, and that additional stellar components formed in different cosmic epochs may be present in these systems. Indeed, the preliminary star formation histories (SFHs) reconstructed for these systems - specifically, for Liller 1 as presented by [Dalessandro et al. \(2022\)](#) in Figure 1.8, and for Terzan 5 as shown by [Crociati et al. \(2024\)](#) in Figure 1.9 - suggest that this is likely the case. In fact, the reconstructed SFH seems to be characterized by at least three significant star formation events in both Terzan 5 and Liller 1. The first and most prominent episode spans a prolonged period of 1–2 Gyr; a feature distinctly inconsistent with the typically short duration of star formation observed in genuine GCs. This initial burst is followed by a continuous star formation that proceeds with very low intensity and two additional bursts. Interestingly, the second episode seems to have occurred at the same epoch in the two systems (8–9 Gyr ago), while the subsequent one is significantly more recent in Liller 1 (1–2 Gyr ago) than in Terzan 5 (3–4 Gyr ago), possibly reflecting distinct histories of interactions with the local environment and, potentially, different orbital histories within the Galactic Bulge. Note that star formation histories characterised by extended periods of quiescence (or low intensity activity) as those shown in Figure 1.8 and Figure 1.9 are not rare either in the universe ([VandenBerg et al., 2015](#)), typical of Dwarf spheroidal galaxies or nuclear star clusters.

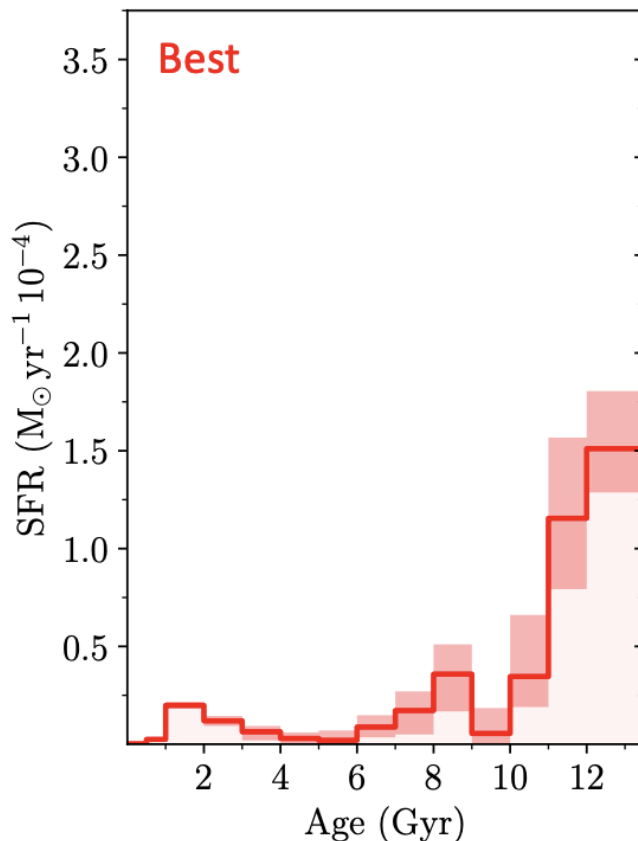


Figure 1.8: Reconstructed SFH of Liller 1 exploiting the synthetic CMD fitting technique (Tosi et al., 1991). SFH obtained through the code Star Formation Evolution Recovery Algorithm (SFERA; Cignoni et al., 2015) best fit solution. The red shaded areas are the uncertainties associated to the model computed from a bootstrap method, and they mark the 5th and 95th confidence level. Image from Dalessandro et al. (2022).

1.4 Terzan 5 Formation Scenarios

The discovery of the complex stellar content of Terzan 5 and Liller 1 poses the problem of their origin. Several hypotheses have been proposed to explain their formation, each suggesting a different evolutionary path. For the sake of clarity, since most of the proposed formation scenarios concern the case of Terzan 5, hereafter I will refer specifically to it. However, because of the striking aforementioned similarity between Terzan 5 and Liller 1, the proposed scenarios can be naturally applied also to Liller 1. The main scenarios suggested in the literature for the origin of Terzan 5 can be summarized as follows. Terzan 5 can be either

1. the remnant of a dwarf galaxy accreted from outside the MW (Brown et al., 2018);

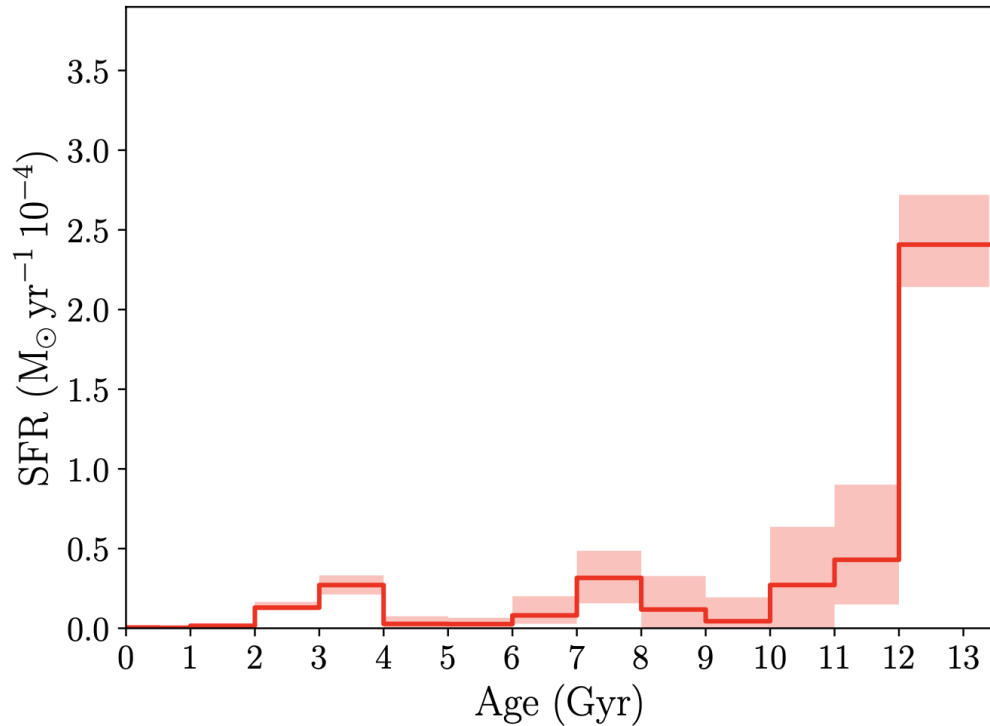


Figure 1.9: SFH of Terzan 5 associated to the SFERA best fit solution. The red shaded areas are the uncertainties associated to the model computed from a bootstrap method, and they mark the 5th and 95th confidence level. To obtain this result, an average foreground extinction of $E(B - V) = 2.5$ and distance modulus $\mu_0 = 13.75$ were adopted. Image from [Crociati et al. \(2024\)](#).

2. the outcome of a merger between two genuine GCs [Pfeffer et al. \(2020\)](#);
3. the BFF of one of the primordial clumps that contributed to the earliest phases of the MW Bulge formation ([Ferraro et al., 2009, 2016](#));
4. the outcome of the accretion of a Giant Molecular Cloud (GMC) by a genuine GC ([McKenzie & Bekki, 2018](#); [Bastian & Pfeffer, 2021](#)).

The first two hypotheses can be excluded on the basis of the Terzan 5 properties collected so far.

Hypothesis (1): The suggestion that Terzan 5 could be the former nuclear star cluster (NSC) of an accreted dwarf galaxy (e.g., [Brown et al., 2018](#)) is disproved by the observed $[\alpha/\text{Fe}] - [\text{Fe}/\text{H}]$ pattern. In fact, the probability that a NSC formed within a galaxy with a low-star forming rate would share the same chemical pattern observed (only) in the MW Bulge is admittedly very small. In addition, the reconstructed orbit (Figure 1.5) strongly disfavors the accretion scenario.

Hypothesis (2): The possibility of a merger between two genuine Galactic GCs (Pfeffer et al., 2020) is also very unlikely, since not a single GC as young (4.5 Gyr old) as the metal-rich ($[\text{Fe}/\text{H}] = +0.3$) sub-population of Terzan 5 is known in the MW. Moreover more than two sub-populations can be present in Terzan 5 as shown by the metallicity distribution and the reconstructed SFH (Figure 1.9).

Hypothesis (3): The possibility that Terzan 5 is the remnant of the primordial fragments that 12 Gyr ago contributed to form the bulge remains one of the most fascinating hypotheses. All the observational facts collected so far and characterizing the stellar content of Terzan 5 have been interpreted (Ferraro et al., 2016) in the context of the self-enrichment process of a very massive (a few $10^7 M_{\odot}$) progenitor system (the proto-Terzan 5) that experienced very intense star formation, generating (and retaining) iron-enriched gas ejected from TypeII SNe. Note that this picture would naturally explain the huge populations of millisecond pulsar (the largest in the entire GC system) hosted in Terzan 5. In fact the large number of neutron stars originated by the TypeII SNe explosions are recycled into millisecond pulsars thanks to the high collision rate of the system (the highest in the Galaxy; Lanzoni et al., 2010). From the retained gas, ejected by both TypeII and TypeIa SNe, a new generation of stars, with $[\text{Fe}/\text{H}] = +0.3$ and $[\alpha/\text{Fe}] = 0$, has formed. Such a massive progenitor, with such a high SFR (characteristic of the Bulge only) and with an in-situ origin, naturally fits into the scenario (e.g., Immeli et al., 2003; Elmegreen et al., 2008; Bournaud & Elmegreen, 2009) proposing that the formation of galaxy bulges starts with the merging of primordial massive clumps of gas and stars. In fact, although most of these massive clumps are predicted to dissolve and form the bulge, a few of them could survive the total disruption (Bournaud, 2016) and be still present in the inner regions of the host galaxy, roughly appearing as massive GCs. At odds with genuine GCs, however, these fossil relics are expected to host multi-iron and multi-age sub-populations, because their progenitors were massive enough to retain the iron-enriched ejecta of SN explosions and they likely experienced multiple bursts of SF. Hence, Terzan 5 could be a BFF, the fossil remnant of one of the primordial clumps that contributed to the earliest phases of the MW Bulge formation (concurring with subsequent processes, as the secular evolution of the disk, bar, and other substructures, to give the Bulge its current appearance). Of course, confirming this possibility would be of paramount importance to shed new light on the formation mechanism(s) of galaxy bulges, which is still one of the most debated topics in astrophysics (e.g. Barbuy et al., 2018).

Hypothesis (4): Before drawing any solid conclusions about the origin of Terzan

5, hypothesis (4) must be explored in detail. Specifically, [McKenzie & Bekki \(2018\)](#) and [Bastian & Pfeffer \(2021\)](#) suggested that the younger stellar component could have formed via the accretion of a field GMC onto a pre-existing genuine GC. The aim of this thesis work is to perform a detailed investigation, through a set of appropriate hydrodynamical N -body simulations, of the plausibility of such a mechanism.

Indeed, although in principle it could be considered a viable alternative, it requires a number of ad hoc conditions. Moreover, a single accretion is not fully compatible with the complex stellar content of Terzan 5 as emerging from the preliminary SFH. Also the timescale of the reconstructed SFH is not reconcilable with the short timescales (< 10 Myr) predicted by [McKenzie & Bekki \(2018\)](#) for star formation following the accretion of a GMC by a GC.

In their hydrodynamical numerical simulations [McKenzie & Bekki \(2018\)](#) suggest that this process is not exceptionally rare. However, verifying these findings requires highly specific and finely tuned conditions. Such events are expected to produce a single, short-lived burst of star formation. The simulations further suggest that massive clusters in the inner galaxy must achieve precise orbital alignments with close tolerances in both position and velocity relative to GMCs to facilitate such interactions.

The merging of a GMC onto a pre-existing GC would occur only when the cluster orbit crosses the Galactic Bulge with a sufficiently low relative velocity, lower with respect to the escape velocity of Terzan 5 itself ([McKenzie & Bekki, 2018](#)). Notably, both Terzan 5 and Liller 1 have orbits largely confined to the Galactic Disc plane, typically reaching no more than ~ 200 pc above it ([Massari et al., 2015](#); [Baumgardt et al., 2019](#)), potentially increasing the likelihood of such encounters. When such alignments occur - a probability significantly dependent on the cluster mass - the massive cluster may rapidly accrete a significant amount of gas or dust from the GMC.

1.5 Aim of this Thesis

The work presented in this thesis focuses on the stellar system Terzan 5, located in the MW's bulge, with the aim of testing the validity of the formation scenario described in hypothesis (4): i.e. that the SG of stars - the young component at $t = 4.5$ Gyr, with $[\text{Fe}/\text{H}] = +0.3$ and $[\alpha/\text{Fe}] = 0$ and a mass of $8 \times 10^5 M_{\odot}$ - can be originated from the infall of a GMC into an initial system of FG stars, the 12 Gyr-old component characterized by $[\text{Fe}/\text{H}] = -0.3$ and $[\alpha/\text{Fe}] = +0.35$.

This thesis extends previous studies such as Bekki (2017) and McKenzie & Bekki (2018), in which the authors used hydrodynamical N -body simulations to investigate the interaction between a progenitor system of Terzan 5 and a GMC. However, a key difference lies in the fact that their work did not account for pre-SN feedback, whereas the model adopted in this thesis does. They concluded that an AGB wind model is not necessary in a simulation which spans only a 14 Myr evolution.

To this aim, the thesis relies on the model proposed in a few previous works (see Calura et al., 2019; Lacchin et al., 2021; Calura et al., 2022; Yaghoobi et al., 2022a; Calura et al., 2024; Yaghoobi et al., 2024), enhancing the resolution with respect to what was done by McKenzie & Bekki (2018), and fine-tuning critical parameters to more accurately model the dynamics of Terzan 5 and its interaction with a GMC. Following the feedback model proposed by Calura et al. (2024), where it is considered the feedback of individual stars (for a detailed description see Section 3.1.3), we find substantial differences with respect to McKenzie & Bekki (2018), showing how the stellar feedback is playing a major role in the formation of Terzan 5's SG.

The analysis performed in this work focuses on the interaction between a stellar FG system, which is influencing the surrounding ambient medium through its gravitational potential, and an infalling denser gas reservoir representing an infalling GMC. Specifically, the simulations are intended to study how the formation of a SG stars can be influenced by two critical parameters:

- the relative velocity of the infalling GMC (v_{GMC}) with respect to Terzan 5, explored through two different sets of simulations, 10 km s^{-1} and 20 km s^{-1} ;
- the mass of the FG star system, considering two other sets of simulations with initial FG star masses of $10^6 M_{\odot}$ and $10^7 M_{\odot}$.

A detailed characterization of the setup is presented in Chapter 3.

The Thesis is organised as follows:

- In **Chapter 2**, I present a detailed overview of the RAMSES code, outlining the numerical methods employed in the thesis.
- **Chapter 3** is dedicated to presenting an in-depth description of the sub-grid stellar feedback model integrated into the customized version of RAMSES, which includes radiative cooling, a novel method that models the formation of individual stars, and the consequent stellar feedback from individual stars. Finally, I describe the specific set-up of the simulations, including the initial conditions and the configuration of the grid, as well as the parameters governing the interaction between Terzan 5 and its surrounding environment.
- In **Chapter 4**, I present the results of the simulations performed, analyzed using Python codes developed independently.
- Lastly, in **Chapter 5**, I present the conclusions of this thesis and explore potential paths for future research that could extend and build upon this work.

Chapter 2

Numerical methods

In modern astrophysics, it is essential to account for the fact that astrophysical phenomena are inherently non-linear, making it is generally impossible to derive analytical solutions to the equations governing their evolution. Instead, numerical methods are required to approximate these solutions. In this chapter, I present the main features of RAMSES, the Eulerian N -body hydrodynamical code adopted in this thesis to run simulations. RAMSES is written in FORTRAN90, and it has been introduced by Teyssier (2002). At first, in Section 2.1, I introduce the Euler equations, which describe fluid dynamics in an astrophysical context, and the numerical techniques used to solve them, distinguishing also between Eulerian and Lagrangian codes. In Section 2.2.1, I focus on RAMSES and I describe the Adaptive Mesh Refinement (AMR) technique, which optimizes computational efficiency by dynamically refining the spatial resolution where needed. Section 2.2.2 is dedicated to the treatment of particle-based methods in the code. Section 2.2.3 presents the gravity and N -body solver, which computes the dynamics of collisionless particles. The hydrodynamical solver used in RAMSES is detailed in Section 2.2.4. Finally, in Section 2.2.5, I discuss the constraints that limit the time step in RAMSES, ensuring numerical stability and accuracy.

2.1 Numerical methods for Hydrodynamics

Astrophysical fluids are typically composed of gas particles, which, while not truly continuous, can be treated as such under certain conditions. Specifically, when the mean free path¹, λ , is much smaller than the size of a fluid element \mathcal{L}_{el} ,

$$\lambda \ll \mathcal{L}_{el} , \quad (2.1)$$

the gas behaves as a continuous distribution of particles, where each fluid element contains a sufficiently large number of gas particles. In this conditions one can neglect fluctuations due to the finite number of particles

$$n\mathcal{L}_{el}^3 \gg 1 , \quad (2.2)$$

yet \mathcal{L}_{el} remains small relative to the characteristic scale L

$$\mathcal{L}_{el} \ll L . \quad (2.3)$$

A definition for the characteristic scale of the system is

$$L \sim \frac{q}{\|\nabla q\|} , \quad (2.4)$$

where q is any characterizing component of the fluid (density, pressure, temperature, or velocity; Clarke & Carswell 2014).

Eq. 2.1 and Eq. 2.3 justify treating fluids in the Universe as a continuous fluid, which is essential for hydrodynamic modeling. Under the typical conditions of temperature, density, and pressure found in galaxy and cluster evolution, it can be approximated as an ideal gas. This approximation allows us to neglect viscosity so that the gas evolution is governed by the Euler equations for a compressible fluid, which, in their conservative form, are expressed as:

$$\begin{cases} \frac{\partial \rho}{\partial t} + \nabla \cdot (\rho \mathbf{u}) = 0 \\ \frac{\partial}{\partial t}(\rho \mathbf{u}) + \nabla \cdot (\rho \mathbf{u} \otimes \mathbf{u}) + \nabla P = -\rho \nabla \Phi \\ \frac{\partial}{\partial t}(\rho e) + \nabla \cdot \left[\rho \mathbf{u} \left(e + \frac{P}{\rho} \right) \right] + \nabla P = -\rho \mathbf{u} \cdot \nabla \Phi + \frac{\Gamma - \Lambda}{\rho} \end{cases} , \quad (2.5)$$

where ρ is the gas mass density, \mathbf{u} is the velocity field, e is the specific (per unit mass) total energy, P is the thermal pressure, Φ is the gravitational potential, Γ

¹Average distance between two particles before collision.

and Λ are the heating and cooling rates, respectively. ∇ is known as the *nabla operator*, is a differential operator used to compute the gradient of a scalar field, the divergence of a vector field, and the curl of a vector field. In Cartesian coordinates, it is defined as:

$$\nabla = \left(\frac{\partial}{\partial x}, \frac{\partial}{\partial y}, \frac{\partial}{\partial z} \right). \quad (2.6)$$

Then, \otimes is the *dyadic product* (or *dyadic tensor*) of two vectors, which is a second-order tensor. Unlike the \cdot product, which produces a scalar, or the \times product, which results in a vector, the dyadic product yields a matrix that represents linear transformations in vector spaces.

In the above equations, the specific total energy e can be split into kinetic and internal energy (ϵ) components as follows:

$$e = \frac{\mathbf{u}^2}{2} + \epsilon. \quad (2.7)$$

Furthermore, the thermal pressure can be linked to the mass density, specific energy, and velocity by

$$P = (\gamma - 1)\rho \left(e - \frac{1}{2} \|\mathbf{u}\|^2 \right) = (\gamma - 1)\rho\epsilon, \quad (2.8)$$

called the equation of state (EOS). In the above equation γ is the adiabatic index, which is equal to 5/3 for a monoatomic gas, representing the ratio of internal energy to gas pressure. Considering the EOS as a fourth equation to add to Eq. 2.5 is necessary to fully determine the description of the gas evolution.

It should be noted that usually the Eq. 2.5 are referred to as the equations of conservation of mass, momentum, and energy, from top to bottom, respectively. To solve the hydrodynamic Eq. 2.5 various numerical methods have been developed over the years. In general, these methods fall into two categories: Eulerian and Lagrangian. I give a brief description of the two methods in the following Sections.

2.1.1 Eulerian codes

The Eulerian codes discretise the simulated volume on a mesh, formed by cells, and the evolution of the fluid is obtained by studying the variables that define the state of the fluid. Specifically, this is done by solving the Eq. 2.5, using variables that describe the state of the system, such as the primitive variables $\mathbf{W} = (\rho, P, \mathbf{u})$ or the conservative variables $\mathbf{Q} = (m, \mathbf{p}, E)$, where: m is the mass of the fluid within the cell, \mathbf{p} is the momentum of the fluid, while the other quantities are defined as in Eq. 2.5. These variables are used to describe the fluid state within each grid

cell volume, with exchanges of mass, momentum, and energy occurring across the interfaces of these cells.

There are different types of Eulerian methods, which can be grouped into two main categories. Finite difference methods (Ryu & Jones, 1995) approximate differential operators by discretizing derivatives using function values at discrete grid points, which can be located at cell centers or edges, depending on the chosen scheme. Finite volume methods (e.g., Zachary & Colella, 1992; Dai & Woodward, 1994; Janhunen, 2000; Ziegler, 2005; Balsara, 2004) instead, work with volume-averaged quantities, ensuring flux conservation across cell interfaces.

Today, a widely used approach in numerical hydrodynamics is the finite-volume Godunov method (Godunov & Bohachevsky, 1959). In this method, fluxes across cell interfaces are computed by solving Riemann problems, an initial value problem for a hyperbolic partial differential equation (PDE) (for a detailed description see Section 2.2.4) and these interfaces and the variables are updated consequently with a conservative scheme.

If one considers constant values for the variables inside the cells, the method has a first-order accuracy; to reach the second-order it is possible to use extrapolation methods. Early Eulerian codes, such as ZEUS (Stone & Norman, 1992), divided the computational box into cells of uniform size. This simple approach, while effective, struggled to achieve high resolution in detailed studies of small spatial scales.

To address this limitation, advancements such as AMR (Berger & Olinger, 1984; Berger & Colella, 1989) have been introduced. AMR dynamically increases resolution in user-defined regions of interest, making it particularly effective for studying in detail small areas while reducing computational costs. Despite the added complexity of handling cells of different sizes, AMR has become a crucial technique in hydrodynamic simulations and is implemented in several widely used codes, including ART (Kravtsov et al., 1997), FLASH (Fryxell et al., 2000), RAMSES (Teyssier, 2002), NIRVANA (Ziegler, 2005), and PLUTO (Mignone et al., 2007), ENZO (Bryan et al., 2014), ATHENA++ (Stone et al., 2020).

2.1.2 Lagrangian codes

Lagrangian methods follow the motion of individual fluid elements, represented as particles, within the computational domain. Unlike Eulerian methods, Lagrangian codes do not discretize the simulation volume into a fixed grid. Instead, fluid variables and their derivatives are computed in a reference frame that moves with the

particles, allowing for a natural adaptation of resolution to the flow.

The most commonly adopted Lagrangian approach is Smoothed Particle Hydrodynamics (SPH), first introduced by [Lucy \(1977\)](#) and [Gingold & Monaghan \(1977\)](#). In SPH, a discrete number of particles sample the continuum fluid, and the gas properties at any point in the computational box are derived by smoothing their quantities over a specified number of surrounding particles. This inherent adaptability makes SPH particularly attractive for applications requiring modelling over a large dynamic range of spatial scales, such as cosmological simulations. Since the resolution automatically follows the distribution of particles, there is no need to explicitly adjust it in different regions of the simulation. Despite its advantages, SPH has some limitations. One of its main drawbacks is its difficulty in accurately representing discontinuities, such as shock waves or contact instabilities, which are common in astrophysical problems. Several widely used Lagrangian codes implement SPH techniques, including GADGET ([Springel et al., 2001](#)), GASOLINE ([Wadsley et al., 2004](#)), GEAR ([Revaz & Jablonka, 2012](#)), CHANGA ([Menon et al., 2014](#)), GIZMO ([Hopkins, 2015](#)), and PHANTOM ([Price et al., 2018](#)).

These codes have played a pivotal role in advancing simulations of complex astrophysical systems. More recently, hybrid approaches have emerged, combining the strengths of grid-based Eulerian methods and mesh-free Lagrangian techniques. One example is AREPO ([Springel, 2010](#)), which solves the hydrodynamic equations on a moving unstructured mesh generated through Voronoi tessellation on a set of discrete points. In [Figure 2.1](#) I show the differences among the various codes discussed.

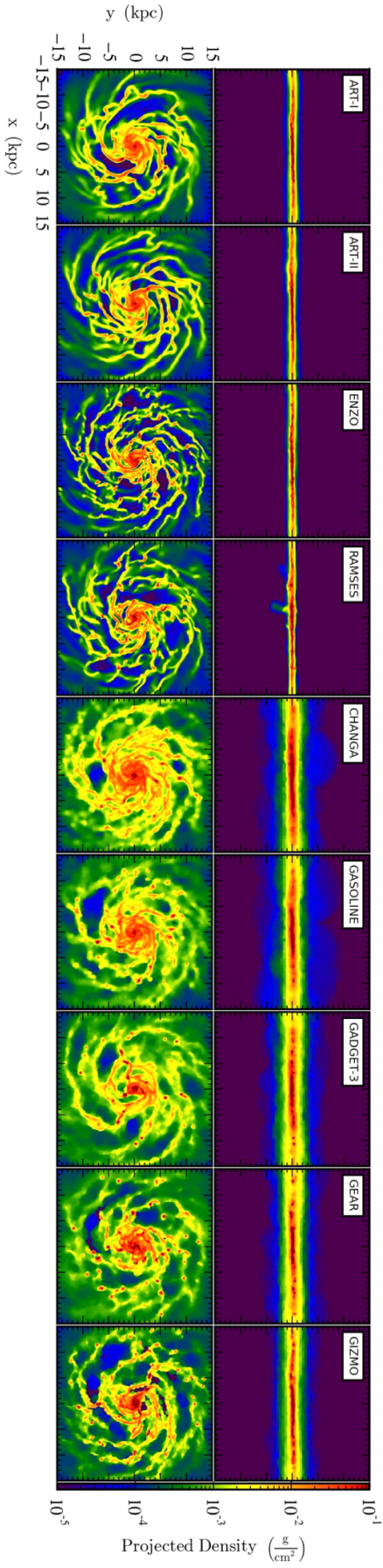


Figure 2.1: The disc surface density of the gas component at 500 Myr is presented for isolated MW-like galaxy simulations using nine different hydrodynamic codes, shown in edge-on (top panel) and face-on (bottom panel) views. The Eulerian, mesh-based codes include ART-I, ART-II, ENZO, and RAMSES, while the Lagrangian, particle-based codes include CHANGA, GASOLINE, GADGET-3, GEAR, and GIZMO. These simulations incorporate common physical processes such as star formation, feedback, radiative cooling, UV background, metal enrichment, and a pressure floor, ensuring a consistent modeling framework. The resolution is uniform across all runs; however, intrinsic differences between AMR and SPH methods lead to discrepancies. The most significant variations appear between mesh-based and particle-based codes, particularly in the inter-arm regions. This figure is adapted from the AGORA code comparison project [Kim et al. \(2016\)](#)

2.2 Numerical methods in RAMSES

As outlined in the previous sections, all the studies presented in this thesis involving hydrodynamics have been conducted using the Eulerian code RAMSES (Teyssier, 2002). The architecture of RAMSES is structured around five principal components: the AMR routines, which manage the hierarchical grid structure by dynamically refining and coarsening cells to enhance resolution where needed; the Particle-Mesh routines, responsible for handling interactions between particles and the computational grid; the Poisson solver routines, which solve the Poisson equation to compute the gravitational potential from the mass distribution; the hydrodynamics routines, which solve the Euler equations to model fluid dynamics, including shocks, turbulence, and gas flows; and, regarding the particles, an N -body scheme similar in many aspects to the ART code of Kravtsov et al. (1997). This aspect is elaborated upon in the following section. Figure 2.2 outlines the general structure, including components not covered in this thesis, such as magnetohydrodynamics (MHD) and radiative transfer (RT), as well as aspects discussed in Chapter 3, such as cooling and other physical mechanisms. The following sections provide a concise overview

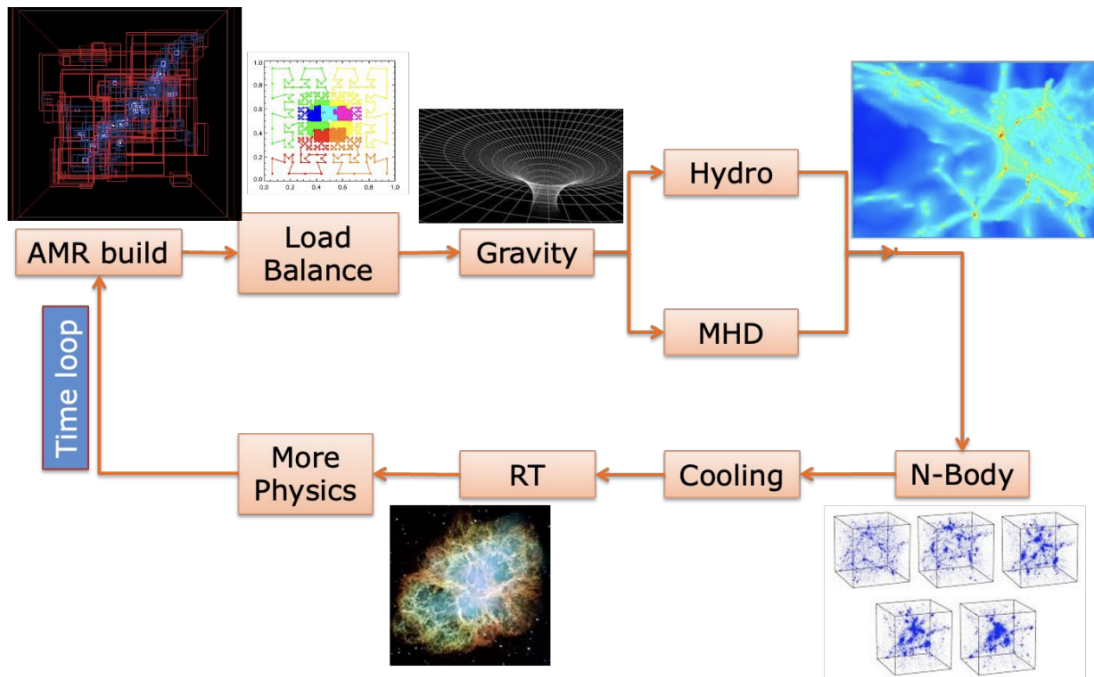


Figure 2.2: Basic functioning of RAMSES, from a presentation by https://indico.ict.inaf.it/event/2752/contributions/17477/attachments/8105/16771/Raffaele_Pascale_presentation.pdf.

of each part, concluding with a description of the time integration method.

2.2.1 Adaptive Mesh Refinement

Some parts of this section are directly based on the work of Teyssier (2002). The RAMSES code adopts an Eulerian framework and a tree-based AMR technique by means of the Fully Threaded Tree (FTT) data structure introduced by Khokhlov (1998). RAMSES considers groups of 2^{dim} cells as a fundamental element, where dim is set to 3 in this thesis work. These groups of cells are called octs; see Figure 2.3 for an oct representation, where the mesh and graph description, considering the cell splitting are visualized. Each oct is assigned a refinement level, denoted by l . The refinement follows a hierarchical structure, a tree structure that originates from a regular Cartesian grid, known as the *coarse grid*, corresponding to $l = 0$. To enable efficient access to octs at any level, they are arranged in a doubly linked list. Each oct at level l is connected to its previous and subsequent octs within the same level, its parent cell at level $l - 1$, and to $2 \times \text{dim}$ neighbouring parent cells at level $l - 1$, and the 2^{dim} child octs at level $l + 1$, allowing for adaptive resolution in different regions of the simulation domain.

The refinement process begins by marking cells according to *user-defined* criteria while following a strict rule: every oct in the tree must be surrounded by $3^{\text{dim}} - 1$ neighbouring parent cells. This constraint ensures a seamless transition in spatial resolution across levels, as illustrated in Figure 2.4, where the grid hierarchy in 2D is visualized. Operationally, the refinement process involves three steps through all levels, starting from the finest level, l_{max} , and progressing down to the coarse grid at $l = 0$:

1. if a split cell contains a child cell that is marked or already refined, then mark it for refinement;
2. then mark the $3^{\text{dim}} - 1$ neighboring cells;
3. finally, if any cell satisfies the user-defined refinement criteria, mark it for refinement.

Lastly, the next step consists in splitting or destroying "children" cells according to the refinement map. RAMSES performs two steps through each level, starting from the coarse grid $l = 0$, up to the finer grid l_{max} :

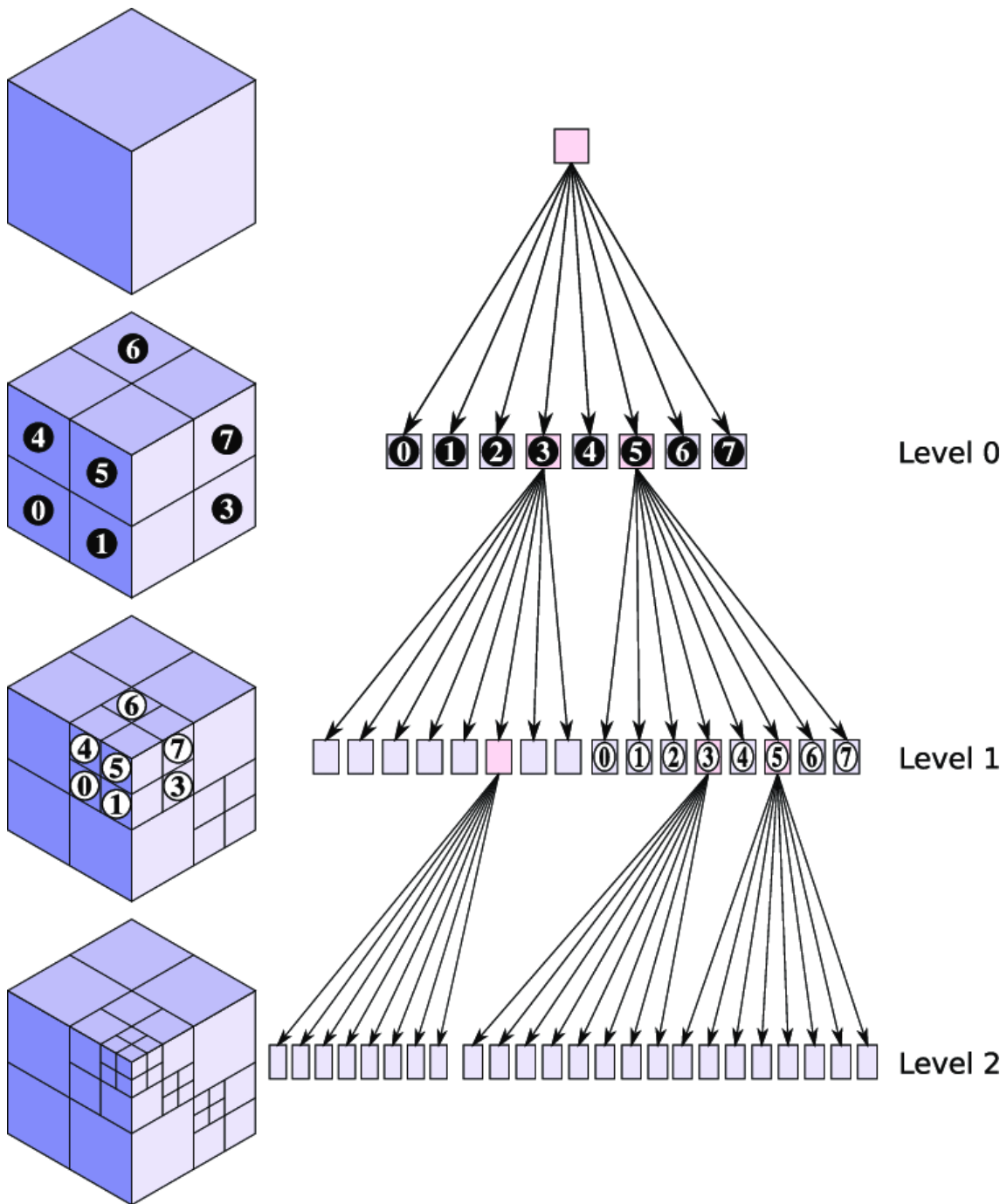


Figure 2.3: Representation of the oct-tree structure (see Section 2.2.2 for a detailed description) as a mesh (left) and as a graph (right). Everytime a cell in the octree is split into 8 cells, the corresponding node, identified in pink in the graph gets 8 children nodes. The leaf nodes in the graph, shown in purple, are the computational cells in the mesh. Image from Laurmaa et al. (2016).

- identify a leaf cell (cell without child octs) marked for refinement, then create its child oct;
- identifying if a split cell is not marked for refinement and destroying its corresponding child oct.

In RAMSES, the time integration can be performed in principle for each level independently; two time stepping algorithms have been presented in [Teyssier \(2002\)](#), a single timestep scheme and an adaptive timestep scheme. The single one consists in integrating the equations from t to $t + \Delta t$, with the same time step Δt for all levels. On the other hand, in the adaptive time step algorithm, each level is evolved in time with its own time step, determined by a level-dependent Courant-Friedrichs-Lewy (CFL) stability condition (see Section 2.2.5).

2.2.2 Gravity and Particle methods

Gravity

Solving for the gravitational evolution of a system of N particles is a complex problem, in particular the N -body problem can only be solved analytically for $N = 2$, while for $N > 2$, it requires numerical approaches. The numerical integration of a collisionless N -body system basically amounts to recursively solving (for a set of subsequent timesteps) the Vlasov-Poisson equations, which are written as follows:

$$\ddot{\mathbf{x}}_i = -\nabla_i \Phi(\mathbf{x}_i), \quad (2.9)$$

$$\nabla^2 \Phi = 4\pi G \rho(\mathbf{x}). \quad (2.10)$$

The quantity $\ddot{\mathbf{x}}$ represents the second derivative with respect to the time of the position vector, i.e. the acceleration, Φ the potential, G the gravitational constant and ρ the density.

Particle methods

There are different numerical methods that can be used to solve the collisionless N -body problem:

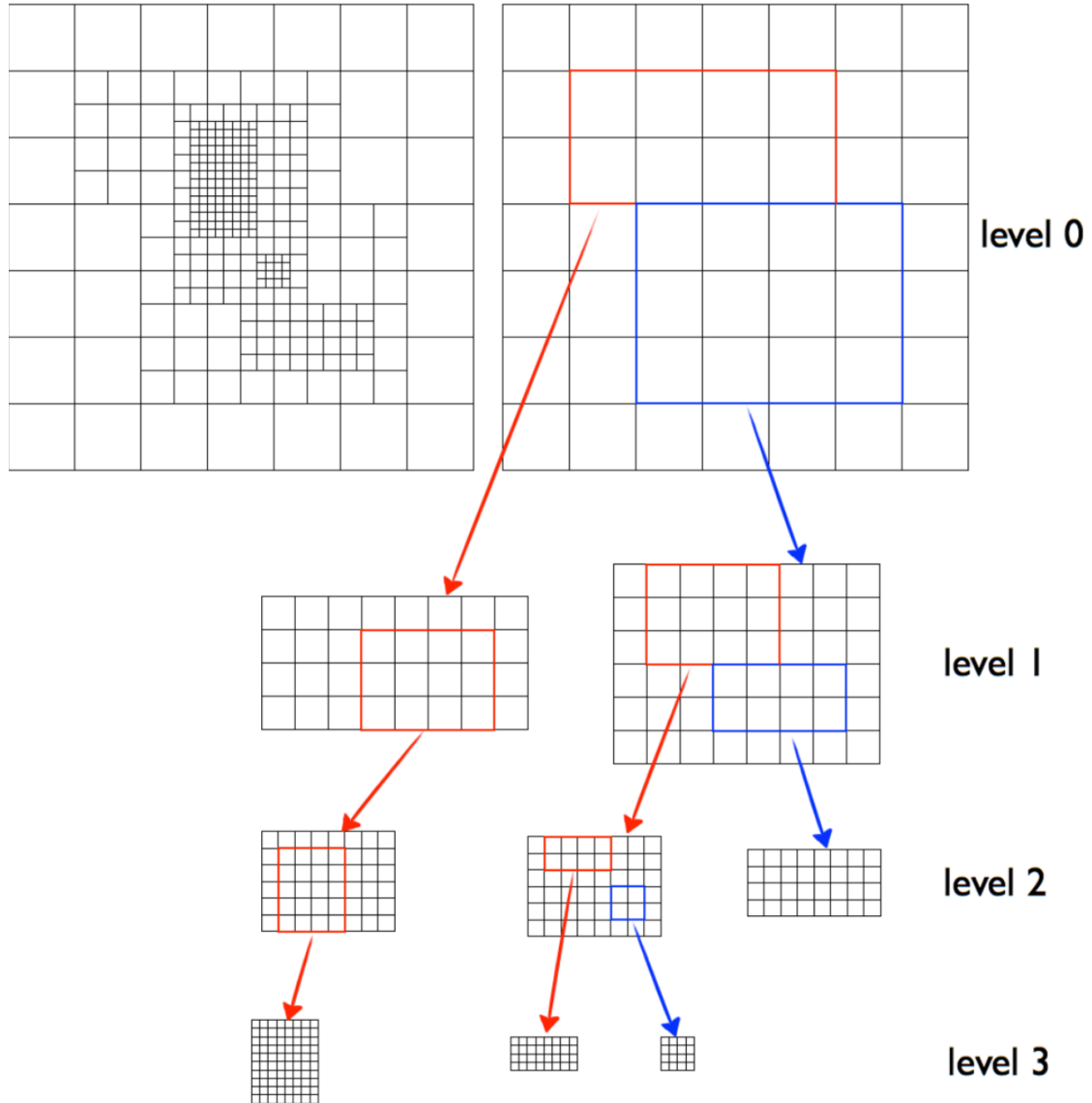


Figure 2.4: The grid hierarchy in $2D$ starts from the coarser grid, level 0 (top right), represented by a Cartesian grid, to the subsequent refined levels. As shown on the top left grid the refinement must be gradual so that neighbouring cells cannot have refinement levels that differ more than one. Credits: <https://2dshocks.wordpress.com/author/becerrafernando/>.

- The first one is the particle-particle (PP) method, where the gravitational force acting on each particle is calculated by summing the contributions from all other particles in the system. However, this is a direct summation technique, where it is necessary to compute the force on the i -th particle given by all other particles $i \neq j$ in the simulation domain. Once obtained the gravitational potential from Eq. 2.12, one can compute the evolution of velocity and position of the particles solving for each particle i Eq. 2.9 and

$$\dot{\mathbf{x}}_i = \mathbf{v}_i . \quad (2.11)$$

When particles are point masses, the potential becomes:

$$\Phi(\mathbf{x}) = -G \sum_{j=1}^N \frac{m_j}{\left[(\mathbf{x} - \mathbf{x}_j)^2 + \varepsilon^2 \right]^{1/2}} \quad (2.12)$$

where ε is the gravitational softening or smoothing length that prevents accelerations from diverging as the distance between two particles approaches zero, thus necessary to ensure the collisionless behaviour of the system of particles. The gravitational force, and consequently the potential, naturally diverges when the separation between particles tends to zero, requiring significantly smaller timesteps for these interactions compared to the rest of the system. The set of Eq. 2.9 and Eq. 2.11 can be solved numerically with different ordinary differential equation (ODE) solving methods, but a widely used method is the Leapfrog scheme, its use in RAMSES is accurately described in Section 2.2.3. Even though the PP method is the simplest approach, its computational time scales as $\mathcal{O}(N^2)$, meaning that the number of operations per timestep is proportional to the square of the system's number of bodies, quickly becoming computationally prohibitive. As a result, this method heavily limits the number of particles that can be used in simulations, with 10^6 particles generally representing the maximum achievable with direct N -body simulations. Nonetheless, this method is well-suited and highly efficient for low and intermediate-mass stellar clusters, where it is even possible to model individual stars rather than star particles. The complexity of these calculations has led to the development of a variety of methods and algorithms to enhance computational efficiency and accuracy.

- An alternative way to solve the collisionless N -body problem is a faster approach commonly used in the literature called the particle-mesh (PM) method,

where the density field is interpolated onto a grid (or mesh), and the Poisson Eq. 2.10 is solved in Fourier space using a Fast Fourier Transform (FFT) algorithm (Hockney & Eastwood, 1981; Klypin & Shandarin, 1983). The main advantage of the PM method is that it is fast and simple; in fact, its complexity scales with the number of particles $\mathcal{O}(N)$. The disadvantage is that the spatial resolution is limited to the mesh size; the force resolution cannot go beyond the size of a single mesh cell. This is a serious problem in cosmological simulations, where a high dynamic range of scales is present; the system of interest could be unresolved as they cluster below the mesh scale. For this reason, the method is particularly suited to compute the force field from almost homogeneous distributions of matter on a large scale (Springel, 2014). The PM method cannot be effective for simulating short-range interactions; thus, it can be enhanced by adding a small-scale component to the PM force, directly computed using the PP approach. This enhancement is called P³M and achieves higher spatial resolution (Hockney et al., 1974; Efsthathiou & Eastwood, 1981). Another improvement to this method is the Adaptive P³M (AP³M) (Couchman, 1991), where higher refinement is applied to grid cells in high-density regions, reducing the number of particles per cell and allowing the PP method to operate on a smaller subset of particles.

- The Tree method (Barnes & Hut, 1986) is based on the recursive division of the simulation domain into sub-domains (tree nodes) that form different levels of a hierarchical tree structure; see Figure 2.3 for a representation of the octree structure. The main goal of such a procedure is to group distant particles together in the computation of the potential and approximate their gravitational potential with a multipole expansion, speeding up the calculation with respect to a direct summation approach. For its nature, this method is well-suited for computing gravitational forces from highly clustered particles and for cases requiring high force resolution. In particular, the resolution increases in regions with a higher concentration of matter, ensuring accurate force calculations on small scales. The main disadvantage of this method is that for highly homogenous matter distributions (e.g., the cosmic density field at high redshifts) the almost vanishing force on each particle is the result of the cancellation of many larger contributions, making the method numerically expensive to obtain high accuracy in the force calculation. This method reduces the complexity that one could obtain with the other described method, and

also the computational cost, scaling as $\mathcal{O}(N \log N)$.

- The last method presented here is the Tree-PM method (Bagla, 2002), which combines the Tree and PM algorithms in order to overcome the latter disadvantage of the Tree method and to exploit the high speed of the PM method. Many N -body codes implement a combination of these methods. In this method, the computational box is organised into a hierarchical tree structure of cells, with the gravitational potential divided into a short-range component, computed thanks to the Tree method, and a long-range component, computed with a PM method. This method is the one used in RAMSES.

2.2.3 Gravitational solver in RAMSES

In RAMSES solving the Poisson equation Eq. 2.10 is done on an adaptive grid using a *one-way interface* scheme (Jessop et al., 1994; Kravtsov et al., 1997), where the solution from a coarser grid provides the boundary conditions and initial guess for the finer grids; the coarse grid solution does not account for the effects of the finer grids. This ensures that the accuracy is the same as if the coarse grid were used alone. The coarsest level, a uniform Cartesian grid that covers the computational box, employs the FFT technique (Hockney & Eastwood, 1981) to efficiently solve the Poisson equation. This approach is much faster than the relaxation methods typically used on finer grids, followed by the Gauss-Seidel method with Red-Black Ordering and Successive Over Relaxation (Press et al., 1992) used for computing the potential.

Once the potential is computed, the acceleration is determined using a 5-point difference algorithm to derive the cell-centered gradient of the potential. Then, an inverse "Cloud-In-Cell" (CIC) scheme is applied to assign the acceleration to each particle.

RAMSES employs a particular version of the PM algorithm to compute the gravitational forces acting on particles (Teyssier, 2002, see also Kravtsov et al., 1997). Although efficient, the PM approach lacks accuracy in modelling short-range forces, as reported in Section 2.2.2. To overcome this, an adaptive grid is implemented, refining cells until a user-defined particle threshold is met. This strategy allows reaching a high resolution locally but can substantially affect the code's performance. Standard grid-based N -body schemes, such as the PM method, typically follow these steps:

1. at first, they compute the mass density ρ on the mesh using a CIC interpolation scheme.
2. ρ is used to solve the Poisson equation to derive the potential Φ on the mesh. The CIC method, introduced by [Hockney & Eastwood \(1981\)](#), is a widely used algorithm for projecting mass onto a mesh, executed in two steps. Instead of simply assigning a particle's mass to the nearest cell, the CIC method treats particles as finite-sized clouds. This approach allows their mass to be distributed across adjacent cells, irrespective of refinement levels. The algorithm is applied consistently across all refinement levels, with the mass allocated to each cell based on the fraction of the cell volume overlapped by the particle's associated cloud. This approach enhances the representation of particle mass by accounting for spatial distributions, ensuring a smoother transition between discrete grid points within the mesh.
3. Calculate the acceleration on the mesh using a standard finite-difference method to approximate the gradient of the potential.
4. Calculate the acceleration for each particle using an inverse CIC interpolation method.
5. Update the velocity of each particle based on its calculated acceleration through a leapfrog algorithm.
6. Update each particle's position according to its velocity.

Leapfrog scheme

In RAMSES, the second-order midpoint scheme with adaptive time stepping is well-suited for AMR grids. However, RAMSES enables synchronization across all levels to operate at the finest timestep, improving accuracy. While this approach is more computationally expensive, it reduces the second-order midpoint method to a standard second-order leapfrog scheme ([Hockney & Eastwood, 1981](#)).

The standard predictor-corrector leapfrog method is an iterative approach for solving ordinary differential equations, involving two steps: the predictor step estimates the next time step, and the corrector step refines this estimate for a more accurate solution. However, this method cannot handle variable timesteps, which

are often required for hyperbolic PDEs due to stability conditions (e.g., CFL condition). The leapfrog integration scheme is defined as

$$\begin{cases} \mathbf{v}_{i+\frac{1}{2}} = \mathbf{x}_i + \frac{1}{2}\mathbf{a}(x_i)\Delta t \\ \mathbf{x}_{i+1} = \mathbf{x}_i + \mathbf{v}_{i+\frac{1}{2}}\Delta t \\ \mathbf{v}_{i+1} = \mathbf{v}_{i+\frac{1}{2}} + \frac{1}{2}\mathbf{a}(x_{i+1})\Delta t \end{cases}, \quad (2.13)$$

where \mathbf{x} are the positions, \mathbf{v} are the velocities, and \mathbf{a} the accelerations of the particles.

2.2.4 Hydrodynamics in RAMSES

In RAMSES, the hydrodynamic equations are solved using a second-order Godunov method based on the Harten, Lax, and van Leer 'Contact' (HLLC) solver (Harten et al., 1983), which is widely used because it accurately captures shocks and discontinuities at cell interfaces by solving local Riemann problems. A Riemann problem is an initial value problem for the Euler equations (describing the conservation of mass, momentum, and energy in an ideal gas) in which two piecewise constant states (left and right) are separated by a single discontinuity and interact at an interface at $t = 0$. The problem is solved numerically using a Riemann solver (Toro et al., 1994), a class of numerical methods that approximate the solution of the Riemann problem at cell interfaces.

The standard first-order Godunov method assumes piecewise constant states within each computational cell. To achieve higher accuracy, RAMSES employs the second-order HLLC scheme, which improves upon the first-order method by providing better resolution of shocks and discontinuities. The HLLC method is a more advanced version of the classical HLL (Harten, Lax, and van Leer) scheme, introducing an additional contact wave to improve the resolution of contact discontinuities, which results in better performance for problems involving shocks and strong discontinuities. A comprehensive overview of Godunov methods is provided in Toro (1977). The current implementation builds upon the methodologies described in Colella (1990) and Saltzman (1994). The approach relies on a conservative discretization of the Euler Eq. 2.5 to accurately capture fluid dynamics.

These equations take the form of a system of hyperbolic PDEs and can be expressed in a compact way using the state vector

$$\mathbf{U} = \begin{pmatrix} \rho \\ \rho\mathbf{u} \\ \rho e \end{pmatrix} = \begin{pmatrix} \rho \\ \rho\mathbf{u} \\ \rho u + \frac{1}{2}\rho\mathbf{u}^2 \end{pmatrix}. \quad (2.14)$$

These quantities, defined in Eq. 2.5 and 2.7, depend on spatial coordinates \mathbf{x} and time t , i.e., $\mathbf{U} = \mathbf{U}(\mathbf{x}, t)$. Based on \mathbf{U} , one can define a flux function

$$\mathbf{F}(\mathbf{U}) = \begin{pmatrix} \rho \mathbf{u} \\ \rho \mathbf{u} \mathbf{u}^T + P \\ (\rho e + P) \mathbf{u} \end{pmatrix} \quad (2.15)$$

where P is the pressure, defined by the equation of state Eq. 2.8, that gives the pressure of the fluid. The Euler equations can then be written in the compact form

$$\frac{\partial \mathbf{U}}{\partial t} + \nabla \cdot \mathbf{F} = 0. \quad (2.16)$$

This compact form highlights the conservative nature of the Euler equations, ensuring mass, momentum, and energy are properly conserved throughout the system.

In RAMSES, the Euler equations discretization takes the following form:

$$\frac{U_i^{n+1} - U_i^n}{\Delta t} + \frac{F_{i+1/2}^{n+1/2} - F_{i-1/2}^{n+1/2}}{\Delta x} = S_i^{n+1/2} \quad (2.17)$$

where U_i^n is the numerical approximation to the cell-averaged values of ρ , $\rho \mathbf{u}$ and ρe at time t^n for the cell i and S represents a generic source term. The time-centered fluxes at the cell edges, $F_{i+1/2}^{n+1/2}$, are computed using a Riemann solver, which does not exactly solve the Riemann problem. In this approach, the cell is initially assumed to have uniform values of U at both interfaces, but in practice, neighboring cell information is used to derive the value within the cell, thus creating a gradient. The gravitational source terms are computed using a time-centred fractional step approach

$$S_i^{n+1/2} = \left(0, \frac{\rho_i^n \nabla \Phi_i^n + \rho_i^{n+1} \nabla \Phi_i^{n+1}}{2}, \frac{(\rho u)_i^n \nabla \Phi_i^n + (\rho u)_i^{n+1} \nabla \Phi_i^{n+1}}{2} \right). \quad (2.18)$$

2.2.5 Time step constraints

Introducing a variable timestep Δt for hydrodynamics is fundamental. Indeed, a timestep that is too large can cause instability, particularly because hydrodynamic equations are inherently hyperbolic and prone to instability.

The first timestep criterion valid for hydrodynamics is the CFL condition (Courant et al., 1967), generally written as

$$\Delta t \leq C_{CFL} \frac{r_{\text{cell}}}{v_{\text{signal}}}, \quad (2.19)$$

which ensures that no information moves more than a cell length within a single timestep. The term C_{CFL} is the Courant factor, a free parameter generally < 1 to grant stability, $r_{cell} = l$ is the cell size, V the volume of the cell and v_{signal} is the maximum signal velocity in the fluid, corresponding to the sound velocity

$$c_s = v_{signal} = \left(\gamma \frac{P}{\rho} \right)^{1/2} . \quad (2.20)$$

In RAMSES, the stability of the timestep is kept by accounting for constraints imposed by both the N -body and hydrodynamic solvers. The first constraint comes from the gravitational evolution of the coupled N -body and hydrodynamic system, which dictates that Δt_1^l must be smaller than a fraction $C_1 < 1$ of the minimum free-fall time (Δt_{ff}) in the cell

$$\Delta t_1^l = C_1 \times \min_l(\Delta t_{ff}) . \quad (2.21)$$

An additional constraint is imposed by the particle dynamics within the AMR grid, requiring that particles move by no more than a fraction $C_2 < 1$ of the local cell size

$$\Delta t_2^l = C_2 \times \frac{\Delta x^l}{\max_l(v_p)} . \quad (2.22)$$

Finally, the last constraint is imposed by the CFL stability condition, which states that the time step should be smaller than

$$\Delta t_3^l = C_{CFL} \times \Delta x^l / \max_l(|u_x| + c, |u_y| + c, |u_z| + c) , \quad (2.23)$$

where the $C_{CFL} < 1$ is the previously defined Courant factor. In the coupled N -body and hydrodynamics case, the actual time step is equal to $\min(\Delta t_1^l, \Delta t_2^l, \Delta t_3^l)$.

Chapter 3

Simulations set-up

In hydrodynamical simulations, capturing key processes like star formation, SN feedback, and chemical enrichment requires high spatial resolution, which is computationally expensive and necessitates a balance between accuracy and feasibility. To address this challenge, hydrodynamical simulations often employ subgrid models, i.e., simplified prescriptions that approximate the effects of unresolved small-scale processes. In this Chapter, I present the set-up of the simulations that are object of this thesis. In particular, the subgrid model adopted to describe star formation is described in Section 3.1.1 while the stellar feedback model adopted is described in Section 3.1.3. In Section 3.2 I outline the set-up of the simulations. Finally, in Section 3.3 I summarize the main parameters used and the tests performed in this work.

3.1 Star formation, stellar feedback models and gas cooling

3.1.1 Star formation

Gaining a deep insight into the formation of cosmic structures requires understanding how star formation progresses across different environments. However, the resolution of cluster-scale simulations is insufficient to resolve the formation of individual stars. To address this limitation, star formation is modeled using sub-grid prescriptions, which can vary between different simulation codes.

In this thesis work, I employ the classical star formation criteria as implemented in the RAMSES code, as detailed in [Rasera & Teyssier \(2006\)](#), coupled with the star formation model adopted by [Calura et al. \(2022, 2024\)](#). The adopted model enables studying the feedback of individual stars, distributed according to a specific initial mass function (IMF). This represents a significant difference from classical simulations, where stellar particles typically represent Simple Stellar Populations. Our star-by-star feedback model approach offers an advantage, such as capturing the properties of the ISM affected by the feedback of single high-mass stars, which is highly sensitive to local gas conditions (density, temperature, turbulence) and thus subject to random fluctuations. Specifically, [Revaz et al. \(2016\)](#) demonstrated that below a critical particle mass of $10^3 M_{\odot}$, stochasticity is an important effect and only a direct star-by-star sampling of the IMF provides a realistic representation of the stellar component in hydrodynamic simulations ([Emerick et al., 2018](#)).

According to the star formation model I adopted, star formation is allowed only in gas cells that satisfy specific criteria: the gas temperature must drop below 2×10^4 K, ensuring that star formation occurs exclusively in neutral gas regions. The star formation is actually active only at the highest refinement level. Once the cells eligible for star formation are identified, gas is converted into stars following the [Schmidt \(1959\)](#) law, where the star formation rate (SFR) is proportional to the gas density divided by a characteristic timescale of star formation

$$\dot{\rho}_{\star} = \frac{\rho}{t_{\star}}, \quad (3.1)$$

where ρ is the gas density in the cell, ρ_{\star} is the stellar density, t_{\star} is the star formation timescale and $\dot{\rho}_{\star}$ is the rate at which stars are formed. This timescale is parametrized

as proportional to the local free-fall time according to

$$t_{\star} = \frac{t_{\text{ff}}}{\varepsilon_{\text{ff}}}, \quad (3.2)$$

where t_{ff} is the local free-fall time, defined as

$$t_{\text{ff}} = \sqrt{\frac{3\pi}{32G\rho}}. \quad (3.3)$$

In the above equations, G is the gravitational constant, ε_{ff} represents the so-called star formation efficiency per free-fall time, a key parameter that quantifies the fraction of gas converted into stars during each star formation episode, given a fixed free-fall time.

It is worth noting that, while the original Schmidt law had a dependence of ρ^2 , the formulation adopted here is observationally justified by the well-established correlation between the SFR surface density and the gas surface density observed in numerous galaxies (Kennicutt & Evans, 2012).

In this thesis I assume that the IMF is a Kroupa (2001), $\xi_{\text{K01}}(m)$. Formally, the IMF is defined as

$$\Phi(m) = \frac{dN}{d\log m}, \quad (3.4)$$

and it represents the number of stars within a given mass interval of width dm in a target stellar system. A Kroupa IMF is defined as

$$\xi_{\text{K01}}(m) = \begin{cases} Am^{-0.3} & \text{if } m < 0.5 M_{\odot} \\ Bm^{-1.3} & \text{if } m \geq 0.5 M_{\odot} \end{cases}, \quad (3.5)$$

where the normalization constants A and B are computed by imposing continuity at $m = 0.5M_{\odot}$ and that

$$\int_{0.1M_{\odot}}^{100M_{\odot}} \xi_{\text{K01}}(m) dm = 1, \quad (3.6)$$

where the two extremes of integration represent the minimum and maximum mass considered in the distribution and the minimum has been set to a different value with respect to the one adopted by Kroupa (2001) in which they use $0.08 M_{\odot}$.

The total mass available for star formation within a cell is distributed among individual stars, following the method of Sormani et al. (2017). The IMF is decomposed into N discrete mass intervals, where each interval is assigned a mass fraction f_i such that

$$\sum_{i=1}^N f_i = 1. \quad (3.7)$$

For the i -th mass interval, the number of individual stars n_i is drawn from a Poisson distribution, with a probability P_i given by

$$P_i(n_i) = \frac{\lambda_i^{n_i}}{n_i!} \exp(-\lambda_i) , \quad (3.8)$$

where the expected value λ_i is defined as

$$\lambda_i = f_i \frac{M}{m_i} . \quad (3.9)$$

Here, M represents the total gas mass available for star formation in the cell, however, in line with [Calura et al. \(2022\)](#), no more than 90% of the total gas in a cell can be converted into stars, while m_i denotes the average stellar mass in the i -th mass bin. To provide a more accurate representation of the IMF, the adopted Poisson distribution employs $N = 100$ linearly spaced mass bins. Within each bin, the calculation of mass fraction f_i requires the assumption of the stellar IMF Eq. 3.5 as

$$f_i = \frac{\int_{M_{ini}}^{M_{max}} m \xi_{K01}(m) dm}{\int_{M_{ini}}^{M_{max}} m \xi_{K01}(m) dm} , \quad (3.10)$$

where the integral denotes the integral over the i -th bin, and the terms M_{ini} and M_{max} are the same as in Eq. 3.6. This condition also implies, as discussed in [Yaghoobi et al. \(2022a\)](#), a minimum density threshold for star formation, given by

$$\rho_{th} = \frac{m_\star}{0.9(\Delta x)^3} \simeq 2.2 \times 10^{-21} \text{ g cm}^{-3} , \quad (3.11)$$

where Δx represents the size of gas cell and m_\star denotes the base star particle mass. The total particle mass in a cell will be an integer multiple of m_\star , determined by a Poisson sampling method as described in Eq. 3.8. As I discussed in Section 3.3.2, I run simulations at two different maximum levels of resolution, thus Δx can be either 0.15pc or 0.30pc depending on the simulation. Also, in this thesis work, I follow [Calura et al. \(2022\)](#) and adopt

$$m_\star = 0.1 \times M_\odot . \quad (3.12)$$

3.1.2 The role of the star formation efficiency

Observations in the local Universe indicate that star formation is an inefficient process, with typical values of ϵ_{ff} of the order of one or a few percent on the scales of individual giant molecular clouds (GMCs, e.g., [Myers et al., 1986](#); [Murray, 2011](#);

Federrath & Klessen, 2012; Grudic et al., 2019), with several surveys reporting a significant spread in ε_{ff} (Myers et al., 1986; Murray, 2011; Evans et al., 2014; Lee et al., 2016; Utomo et al., 2018; Grudic et al., 2019; Grisdale et al., 2019). However, deeper observations of GMCs in lensed star-forming galaxies suggest higher values of ε_{ff} at redshift $z \sim 1$ (Dessauges-Zavadsky et al., 2023). Similarly, observations of local starbursts also indicate elevated ε_{ff} values Fisher et al. (2022). In such environments, the physical conditions of the star-forming gas may resemble more closely those of early galaxies, as highlighted in various studies (Heckman et al., 1998; Petty et al., 2009; Silverman et al., 2015).

In Calura et al. (2022), the adopted value of $\varepsilon_{\text{ff}} = 0.1$ is motivated by previous cosmological simulations of MW-sized galaxies, which demonstrate that this choice aligns with direct observations of molecular clouds and successfully reproduces key scaling relations, such as the Kennicutt-Schmidt law, along with other observables (Agertz & Kravtsov, 2015). Subsequent studies of isolated MW-like systems further indicate that star formation models regulated by stellar feedback require $\varepsilon_{\text{ff}} = 0.1$ (Grisdale et al., 2019). In this work, I test $\varepsilon_{\text{ff}} = 0.1$ and $\varepsilon_{\text{ff}} = 1$, evaluating their impact on the formation of dense stellar aggregates. Notably, $\varepsilon_{\text{ff}} = 1$ is chosen as the reference value in the following sections. It is important to highlight that ε_{ff} is a parameter that encapsulates unresolved physical processes in the simulations, such as gas dynamics and feedback mechanisms. Adopting a fixed value for ε_{ff} is likely unsuitable and its optimal value may depend on the resolution of the simulation. Future investigations will explore the effects of different ε_{ff} values, considering its relationship with resolution and its role in a more realistic modeling of star formation, as discussed in Chapter 5.

3.1.3 Stellar Feedback

In this work, the stellar feedback model follows the approach of Calura et al. (2024), assuming that individual stars with masses in the range $8 M_{\odot} \leq m \leq 40 M_{\odot}$ contribute to feedback by injecting mass and energy into the interstellar medium during both the pre-SN and SN phases.

Multiple studies suggest that pre-SN feedback is fundamental in shaping the evolution of young stellar clusters and their environments (Hopkins et al., 2010; Kruijssen et al., 2019). Furthermore, previous studies indicate that the cumulative energy injected by massive stars during the pre-SN phase is comparable to that released by SN explosions (Castor et al., 1975; Rosen et al., 2014; Calura et al.,

2015; Fierlinger et al., 2016). Given these considerations, accurately modeling stellar feedback in the pre-SN phase is essential.

In the models implemented in this work, during the pre-SN phase and starting immediately after their formation, each massive star continuously injects mass and energy into the surrounding medium through stellar winds. The rates of mass and energy loss, denoted as \dot{M} and \dot{E} , respectively, are proportional to the initial stellar mass m_{ini} , expressed as:

$$\dot{M} = \eta \frac{m_{\text{ini}}}{\tau_m} \quad (3.13)$$

and

$$\dot{E} = \frac{\dot{M} v_w^2}{2}. \quad (3.14)$$

In Equations 3.13 and 3.14, η is a dimensionless parameter that controls the efficiency of mass loss. I set $\eta = 0.45$ Calura et al. (2024) while τ_m represents the adopted stellar lifetimes of Portinari et al. (1998). In this work, I used the analytical fit from Caimmi (2015) expressed as:

$$\frac{\tau}{\text{yr}} = 10 \left[C_1 (m_{\text{ini}}/M_{\odot})^{-C_2 + C_3} \right], \quad (3.15)$$

with $C_1 = 4.19$, $C_2 = 0.37$, $C_3 = 5.71$.

The terminal wind velocity is assumed to be $v_w = 2000 \text{ km s}^{-1}$ (Weaver et al., 1977; D’Ercole et al., 2008; Vink, 2018). Additionally, I do not assume any dependence of the mass return rate on stellar metallicity.

The spatial concentration of massive stars can be extremely high, leading to excessively large gas temperatures, which in turn result in prohibitively small timesteps in the simulation. To mitigate this issue, I impose an upper limit on the temperature ($T_{\text{max}} = 10^8 \text{ K}$) of the hot medium driven by stellar feedback.

3.1.4 Cooling prescriptions

In this thesis, I adopt the native, metal-dependent implementation of radiative cooling of RAMSES, based on equilibrium-thermochemistry and where the cooling and heating rates of the gas are computed as a function of the temperature, density and metallicity. The adopted cooling function in the absence of a UV background is shown in Figure 3.1 for various values of the metallicity Z .

When dealing with simulations, particularly those involving high, density regions of the ISM, such as the typical cold, star-forming gas the energy returned by massive stars can be artificially radiated away extremely quickly (Katz, 1992) due to efficient

cooling. One of the main consequences of rapid radiative cooling is the inefficiency of stellar feedback, leading to unregulated stellar mass growth. Such effects arise for several reasons, including inadequate resolution and the absence of physical processes associated with stellar feedback, such as radiative heating from young stars (Geen et al., 2016), radiation pressure (Murray, 2011), and other non-thermal processes (e.g., magnetic fields, turbulence, and cosmic rays; see Teyssier et al., 2013; Farcy et al., 2022).

For these reasons, various methods have been proposed to mitigate and prevent the immediate radiative loss of energy injected by massive stars (e.g., Thacker & Couchman, 2000; Agertz et al., 2013; Rosdahl et al., 2017). One possible way to address overcooling in these dense regions is to increase the resolution, if possible. In particular, Kim & Ostriker (2015) modeled the evolution of SN remnants to determine the required ideal cell size to prevent overcooling. They found that, in the case of a uniform medium, the ideal resolution must be at least three times smaller than the shell formation radius, defined as $r_{\text{SF}} = 22.1 n_0^{-0.4}$, where n_0 is the gas number density in units of cm^{-3} . In our case, the maximum density can be of the order of $n_0 \sim 10^5 \text{ cm}^{-3}$.

Apart from increasing the resolution, sub-grid methods are also used to prevent local overcooling. In this work, I temporarily switch off cooling in selected cells, following the general approach proposed by Teyssier et al. (2013). In this method, the feedback is released as thermal energy and simultaneously stored in a tracer, which is passively advected with the flow. Each time a massive star forms or a SN explodes, in addition to injecting thermal energy into the host cell, a "non-thermal" energy tracer is also accumulated on the grid in the form of a passive scalar ρ_{NT} , which can be regarded as some unresolved, 'turbulent' amount of energy. In the original implementation, designed primarily for modeling star particles, radiative cooling is switched off in cells where the local non-thermal velocity dispersion σ_{NT} exceeds a given threshold σ_{min} . Additionally, ρ_{NT} is assumed to decay over a dissipation timescale t_{diss} . This formalism involves two adjustable parameters: t_{diss} and σ_{min} . As described in Calura et al. (2022) and Calura et al. (2024), we choose to constrain these two parameters empirically, starting from known recipes from the literature tested at different regimes of mass and spatial resolution (Dubois et al., 2015).

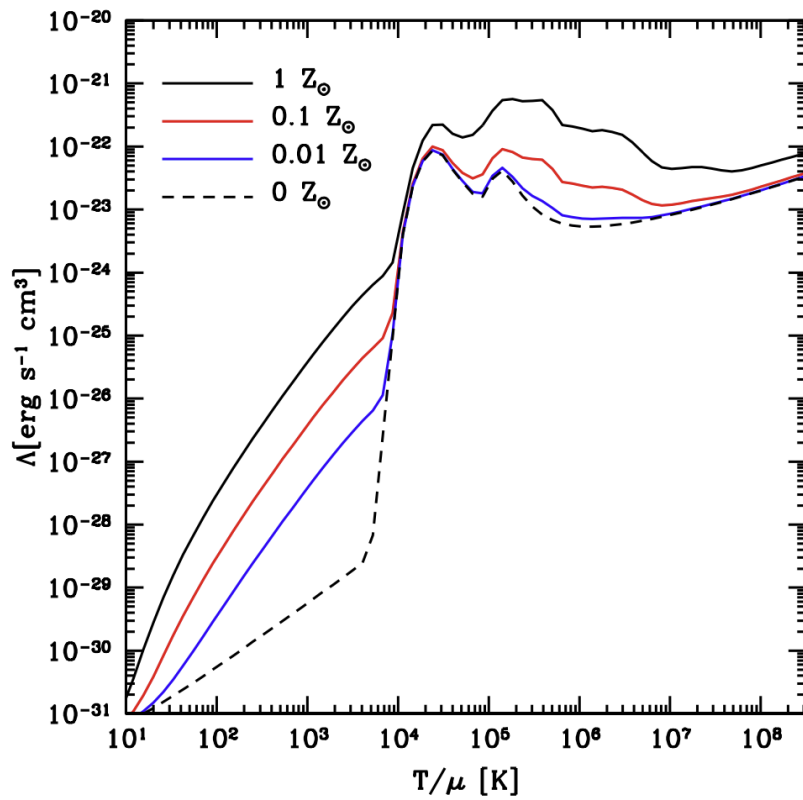


Figure 3.1: The cooling function implemented in the RAMSES code for $Z = 0, 0.01, 0.1$ and $1 Z_{\odot}$ in the absence of a UV background, image from [Agertz et al. \(2013\)](#).

3.2 Initial conditions

3.2.1 Gas

This thesis aims to model a potential interaction between Terzan 5 and a GMC within the MW's bulge, as explored similarly in the study [McKenzie & Bekki \(2018\)](#). The simulations performed in this thesis work considered a box with length of 40 pc. To test convergence, I performed simulations at two different maximum levels of refinement l_{\max} : a lower refinement level 7 and a higher level of 8. The results of Chapter 4 are based on the latter.

The GMC is modelled as a homogeneous distribution rather than a fractal structure as done in [McKenzie & Bekki \(2018\)](#) (or [Bekki, 2017](#)) and proposed in studies such as [Falgarone et al. \(1991\)](#) and [Kennicutt & Evans \(2012\)](#). GMCs exhibit a complex structure, which also leads to significant nomenclatural ambiguity. Their boundaries, identified through dust, CO emission, or extinction, can be characterized by a fractal nature ([Falgarone et al., 1991](#); [Scalo, 1990](#); [Stutzki et al., 1998](#)). When mapped with sufficient sensitivity and dynamic range, these clouds reveal a highly structured morphology, predominantly composed of filaments, within which denser, more compact cores are often embedded (e.g., [André et al., 2010](#); [Men'shchikov et al., 2010](#); [Molinari et al., 2010](#)). While clouds and cores are relatively well defined, intermediate structures remain more ambiguous. Here, however, for the sake of simplicity, I opted for a homogeneous structure.

In all the simulations that are presented, the interaction is described in a reference frame co-moving with Terzan 5. In this reference frame, the center of mass of Terzan 5 remains approximately stationary at the center of the simulation box, while the GMC enters from one side of it.

Once the The GMC enters the simulation box, its crossing is followed for a length of 100 pc, after which the simulation is interrupted. This simplified representation provides a controlled environment for studying the physical processes at play while still capturing the essential characteristics of a GMC.

Figure 3.2 shows a schematic set-up of the interaction, which is inspired to the 'wind tunnel' set-up adopted in [Calura et al. \(2019\)](#). In this configuration, the GMC is represented as gas entering the simulation box from the x -axis to the left, while Terzan 5, initially, is a self-gravitating stellar system within an ambient medium at very low density, mimicking the one of the Galactic bulge.

The ambient medium is initialized with a temperature of $\sim 10^4$ K which is typical

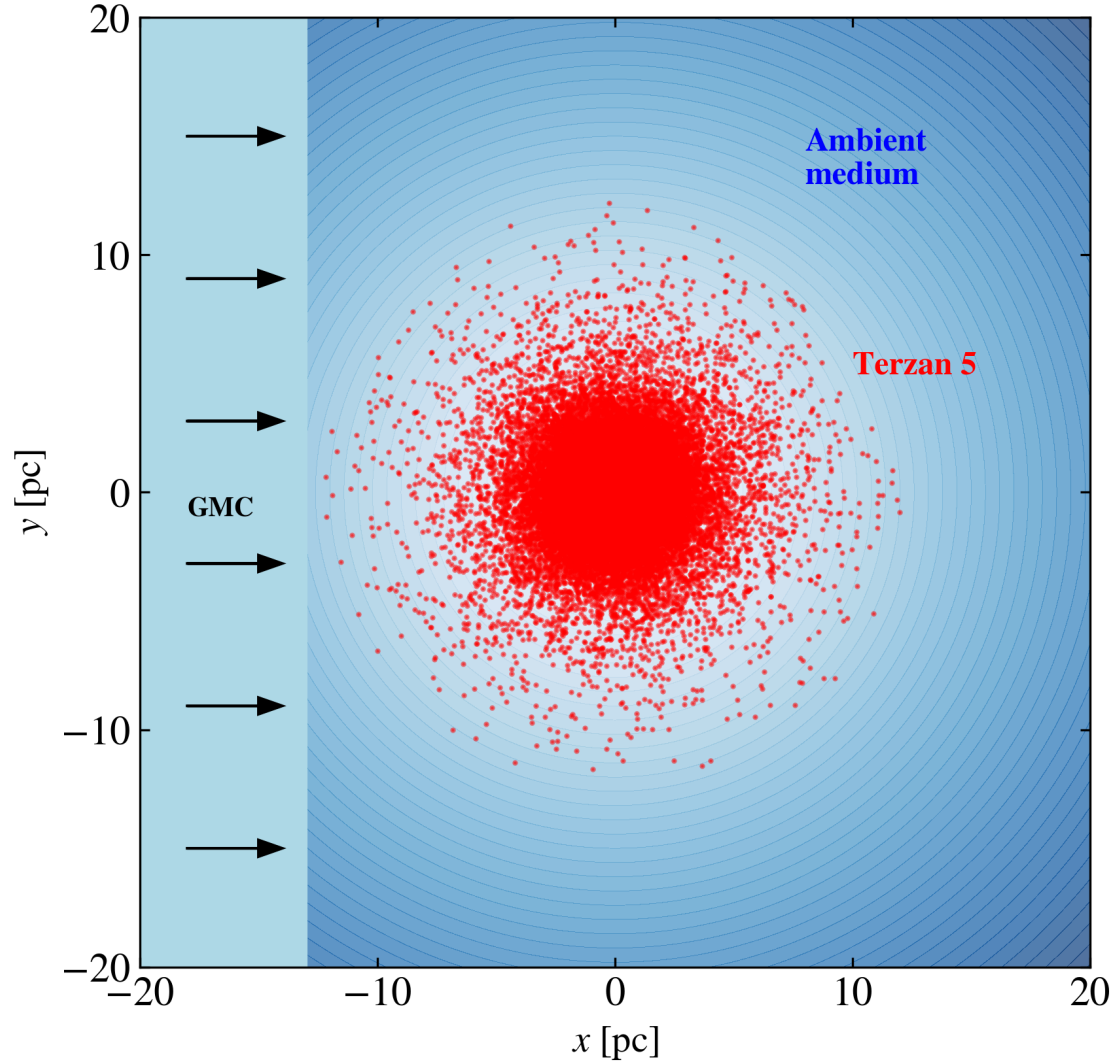


Figure 3.2: A schematic representation of the simulation set-up. At the beginning of the simulation ($t = 0$ Myr). Terzan 5 is located at the center of the simulation box, while the GMC is still outside, moving towards it. At this stage, the FG stars do not produce ejecta; they contribute only to the gravitational potential. As the GMC enters the box, its gas becomes available for the formation of SG stars. Due to the gravitational potential of the FG stars, the infalling gas is attracted toward the center, enhancing the conditions for SG star formation.

of the warm photoionised ISM (e.g., [Haffner et al., 2009](#)) and a density of 10^{-2} cm^{-3} ($\sim 10^{-26} \text{ g cm}^{-3}$). While for the GMC it has been adopted a temperature of 10^2 K , and a density of 10^2 cm^{-3} ($\sim 10^{-22} \text{ g cm}^{-3}$), which corresponds in term of mass considering the dimension assumed ($40 \text{ pc} \times 40 \text{ pc} \times 100 \text{ pc}$) to a GMC of mass $M_{\text{GMC}} \sim 2.35 \times 10^5 M_{\odot}$. For what concerns the metallicity, expressed here as the mass fraction of metals to maintain consistency with the notation used in the code, it has been specifically set to $Z = 0.03$ for the GMC and $Z = 0.001$ for the ambient medium. These values are summarized in [Table 3.1](#), while in [Figure 3.3](#) I show the initial density value at $t = 0 \text{ Myr}$. The other initial physical quantities specified in the caption are the pressure normalized to the Boltzmann constant (P/k_B in $\text{cm}^{-3} \text{ K}$), the temperature (T in K) and the gas velocity along the x -axis (v_{GMC} in km s^{-1}). This set of initial conditions serves as a general starting point for all simulation conditions presented in this thesis.

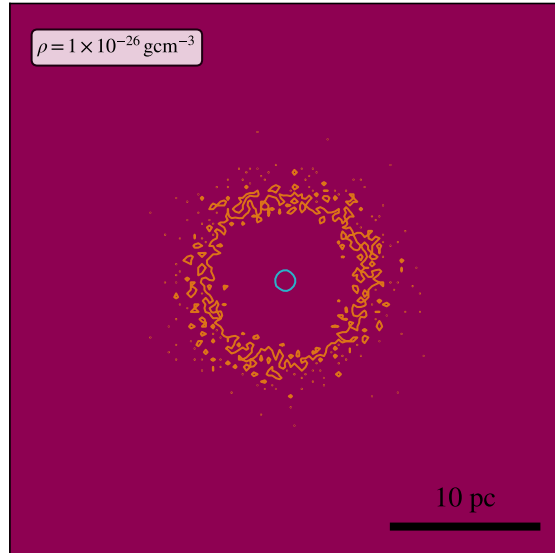


Figure 3.3: The two orange and cyan contour levels enclose the initial regions where the FG stellar density are 10^{-3} and 0.5 times the maximum value, respectively. Besides the initial gas density reported, the main physical quantities of the set-up are the pressure normalized to the Boltzmann constant $P/k_B = 10^2 \text{ cm}^{-3} \text{ K}$, the temperature $T = 10^4 \text{ K}$ and the gas velocity along the x -axis $v_{\text{GMC}} = 0 \text{ km s}^{-1}$. The physical scale is reported in the bottom right of the panel.

The simulations performed in this thesis work aim at exploring the influence that two main key parameters may have on the formation of the SG stars in Terzan 5: the initial mass of the FG stars and the velocity of the infalling gas. To evaluate their effects, I tested two different values for the total mass of the FG stars (specif-

ically $10^6 M_{\odot}$, similar to the current observed value, see Section 1.2 and $10^7 M_{\odot}$). At the same time I tested two different values for the infalling velocities of the gas: 10 km s^{-1} and 20 km s^{-1} . Both the FG mass and gas velocity are critical in determining whether the cluster can accumulate sufficient material to form a SG star system. The rationale for selecting these specific values is postponed to Section 3.3. In Chapter 5 possible variations to these parameters and other parameters, not treated in this work, are investigated.

3.2.2 FG Stars

In this thesis work, Terzan 5 is composed of two components, i.e. the FG and the SG. The FG star system has been considered with two different masses $M_{\text{FG}} = 10^6 M_{\odot}$ and $M_{\text{FG}} = 10^7 M_{\odot}$, while the SG is composed only of newly formed stars following the interaction of the GMC with the FG and is the object of our study. This section provides an overview on the main properties of the model used to describe the FG stars of Terzan 5, and it explores the method used to sample its initial conditions. Also, I introduce the fundamental concept of collisionless system (see Chapter 4 in [Binney & Tremaine, 2008](#) for an extended and detailed description).

Assessing whether a system is collisionless is intrinsically linked to its dynamical behavior, particularly its *two-body relaxation time* (t_{2b}). This timescale quantifies the rate at which stars in a system interact and exchange energy through gravitational encounters. The two-body relaxation time t_{2b} is defined as

$$t_{2b} = \frac{0.1N}{\ln N} t_{\text{cross}} , \quad (3.16)$$

where N is the number of particles in the system, t_{cross} is the crossing time given by R/v , characteristic time scale that a star with typical velocity v needs to cross the entire system of radius R . When the two-body relaxation time is much longer than the system's age, the system can be considered collisionless, with stellar orbits remaining unaffected by two-body interactions, considering that each star of the system moves under the influence of a continuous gravitational field.

As an example, in order to assess conservatively whether the system can be treated as collisionless, we can take into account a simple estimate of the two-body relaxation time by considering a typical GC with a mean mass of $M = 2 \times 10^5 M_{\odot}$ (therefore with a mass significantly lower than our models), and compute the number of objects $N = M/m_{\text{mean}}$, where $m_{\text{mean}} = 0.54 M_{\odot}$, the average mass for a Kroupa IMF ([Kroupa, 2001](#)), this gives:

$$N = \frac{2 \times 10^5 M_{\odot}}{0.54 M_{\odot}} = 3.7 \times 10^5 . \quad (3.17)$$

Then, considering the typical crossing time of a GCs ([Lanzoni et al., 2010](#)) as $t_{\text{cross}} \sim 10^5$ yrs we can use the formula for the two-body relaxation time Eq. 3.16 and we obtain:

$$t_{2b} \approx 0.3 \text{ Gyr} .$$

The simulation timescales are much shorter than t_{2b} , therefore, the system can be

considered as collisionless. In fact, the typical timescale evolution of the simulations is, at most, of $t \sim 12$ Myr, as I will explain in detail in Section 3.3.2.

Any collisionless stellar system is entirely described by its distribution function (DF). A DF is a probability density function that describes the probability of finding a star within the volume element $d^3\mathbf{x}d^3\mathbf{v}$ of phase space. A DF must satisfy certain conditions: it must be everywhere positive, the integral over the entire phase space must be finite, and it must be a solution of the Collisionless Boltzmann Equation

$$\frac{df(\mathbf{x}, \mathbf{v}, t)}{dt} = 0, \quad (3.18)$$

where I have called f the DF. On timescales much shorter than the two-body relaxation time, the dynamic evolution of the system due to particle interactions and any potential variation in the gravitational field over time can be neglected. Under these conditions, the system is said to be in a steady state, and the DF does not evolve with time. In the treatment of the FG stars in Terzan 5, I considered this to be the case, since the relaxation time is much longer than the characteristic timescale of the interactions I aim to represent with the simulations in this thesis. Once the DF of a system is known, every quantity (e.g. density, mass, potential, velocity distributions) can be directly computed from the DF. In my specific case, the knowledge of the DF that describes the FG stars is also crucial because it allows to easily sample the initial conditions, i.e. a set of N particles with known position, velocity and mass, to be used in the simulations.

Plummer and King models

I have assumed that the phase-space distribution of the FG stars in Terzan 5 follow a [Plummer \(1911\)](#) model. In particular, in such model the three dimensional spatial distribution is given by

$$\rho_{\star}(r) = \frac{3M_{\text{FG}}}{4\pi a^3} \left(1 + \frac{r^2}{a^2}\right)^{-\frac{5}{2}}, \quad (3.19)$$

where M_{FG} represents the mass of the FG stars and a is a characteristic radius. For the Plummer distribution a corresponds to the model's effective radius, i.e. the radius that encloses half of the projected mass. One of the advantages of using a Plummer over other models is that its DF is fully analytical, together with many other relevant model's quantities as the projected stellar density and mass distributions, or the system velocity dispersion. As I discuss in the following Section, this simplifies the generation of the initial conditions of the FG stars in the simulation.

Considering a Plummer model, where the potential is defined as

$$\Phi = -\frac{GM_{\text{FG}}}{\sqrt{r^2 + a^2}} \quad (3.20)$$

and the Poisson equation (Eq. 2.10) I can derive the mass in function of the radius $M(r)$, defined as

$$M(< r) = \frac{M_{\text{FG}}r^3}{\sqrt{(r^2 + a^2)^3}} . \quad (3.21)$$

In case of a Plummer model (Eq. 3.19), the DF is known analytically and it writes

$$f(\mathcal{E}) = \frac{24\sqrt{2}}{7\pi^3} \frac{a^2}{G^5 M_{\text{FG}}^4} \mathcal{E}^{7/2} , \quad (3.22)$$

where M_{FG} and a are defined as in Eq. 3.19.

As shown in Figure 3.4, the FG stars and the analytical Plummer profile (with a Plummer radius of $a = 1.0$) exhibit a good agreement. The Plummer profile here represents the initial mass distribution of Terzan 5 before the formation of SG stars. For comparison, I also include in the figure the King profile (King, 1966), derived from the actual observational data from Terzan 5, considering its FG and SG (see Table 1.1).

The King profile depends on the half-mass radius and on another parameter, that can be either the dimensionless central potential W_0 or c , the concentration parameter defined $c = \log\left(\frac{r_t}{r_0}\right)$, where r_0 is the King radius, a characteristic scale length of the model.

3.2.3 Generation of the FG stars

Once the DF of a stellar system is known, the phase-space positions of any set of particles can be sampled directly from its DF. In the specific case of the simulation presented in this thesis, I sampled a set of N particles representing the FG stars of Terzan 5 with a three-step algorithm that I present below.

1. At first, the positions of the FG stars are drawn from the model's mass distribution;
2. then, the velocities are assigned by using the system's DF;
3. finally, to each particle it is assigned a mass.

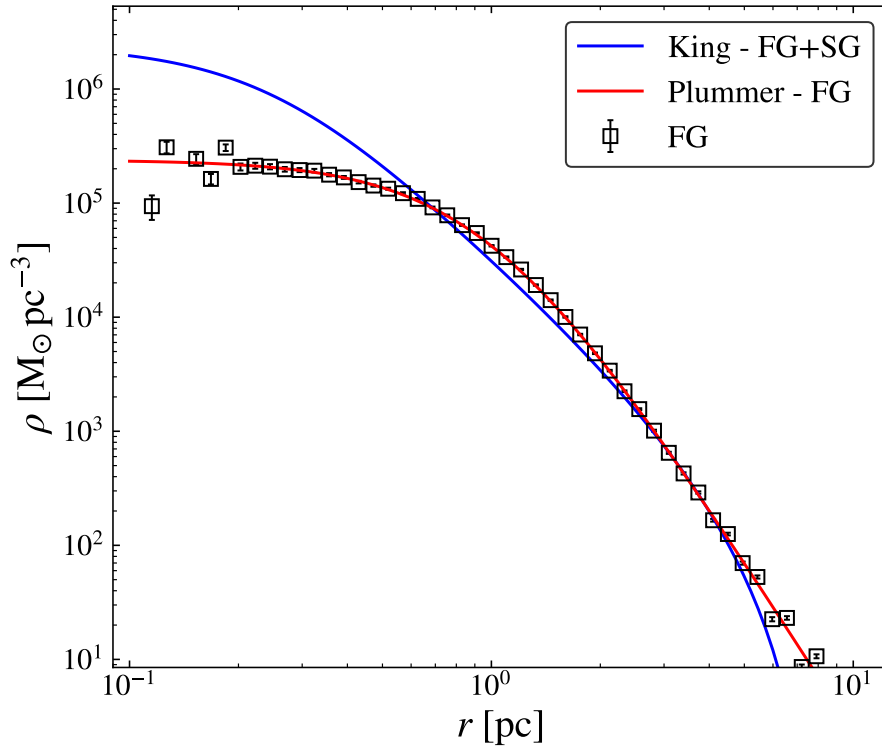


Figure 3.4: Comparison between the density profiles for the system of FG stars with a total mass of $10^6 M_{\odot}$, at $t = 0$ Myr, is performed against the King (total Terzan 5 FG and SG stars, as reported in Table 1.1) and Plummer (FG only) profiles, the Plummer radius assumed is $a = 1.0$. This analysis provides insights into the structural properties of the stellar system and assesses its deviation from these well-established theoretical models.

I have assumed a total mass M_{tot} for the FG stars of Terzan 5, so $M_{\text{FG}} = 10^6 M_{\odot}$, while I have considered a number particles $N = 10^5$. Considering that each particle has the same mass m_p , thus

$$m_p = \frac{M_{\text{tot}}}{N} = 10 M_{\odot} . \quad (3.23)$$

Position assignment

For the sake of clarity, I first define the spherical coordinates:

$$\begin{cases} x = r \sin \theta \cos \phi \\ y = r \sin \theta \sin \phi \\ z = r \cos \theta \end{cases} \quad (3.24)$$

where (x, y, z) are the Cartesian coordinates in which $r \in [0, \infty[$, $\theta \in [0, \pi[$ and $\phi \in [0, 2\pi[$. In spherical coordinates, assigning a position to each point translates into

creating N triplets (r, θ, ϕ) . Since the system is spherically symmetric, ρ depends only on r , therefore

$$\int_0^x dx \int_0^y dy \int_0^z dz \rho(x, y, z) = \int_0^\pi d\theta \sin \theta \int_0^{2\pi} d\phi \int_0^r dr r^2 \rho(r). \quad (3.25)$$

The sampling of the variables r , θ and ϕ can be performed independently from one another, as can be noted from Eq. 3.25. For a set of N particles, r must be sampled from the probability density distribution $P(r) = r^2 \rho(r) dr$, θ from $P(\theta) = \sin \theta d\theta$, and ϕ from $P(\phi) = d\phi$. To sample the radial coordinate r , the inverse mass function method is used. This method requires first computing the cumulative probability function, proportional to the total mass $M(r)$ for the term r , while for ϕ and $\sin \theta$, it remains constant. The cumulative probability function for r is normalized to unity, defining the dimensionless mass parameter $q(r)$ ($0 \leq q \leq 1$). Since $q(r)$ is a growing function of r , it can be inverted to obtain $r(q)$. This inversion is performed through linear interpolation of $r(q)$, where q is sampled on a grid of points q_i evenly spaced in the logarithm of the variable. Then, N values of q are drawn from a uniform distribution. The corresponding radii are then assigned by evaluating $r(q)$ for each sampled q . For ϕ , values are uniformly sampled in $[0, 2\pi[$, while for θ , values are uniformly sampled in $[-1, 1[$ and then transformed using the arcsin function. Finally, the spherical coordinates (r, θ, ϕ) are converted into Cartesian coordinates (x, y, z) using Eq. 3.24.

Velocity assignment

To assign velocities to each position \mathbf{x}_i a rejection sampling algorithm have been employed to extract the velocities from the DF at fixed positions. Generally, once the position \mathbf{x}_i , given a DF $f(\mathbf{x}, \mathbf{v})$, the corresponding velocity probability function also referred to as Velocity Distribution (VD), is

$$\text{VD}(\mathbf{x}_i, \mathbf{v}) = \frac{f(\mathbf{x}_i, \mathbf{v})}{\int d^3\mathbf{v} f(\mathbf{x}_i, \mathbf{v})} = \frac{f(\mathbf{x}_i, \mathbf{v})}{\rho(\mathbf{x})}. \quad (3.26)$$

For a system with finite mass, as the one describing the FG stars of Terzan 5 in this thesis, the escape velocity at a given position \mathbf{x}_i is defined as

$$v_{\text{esc}} = \sqrt{-2\Phi(\mathbf{x}_i)}. \quad (3.27)$$

The procedure for sampling velocities proceeds as follows. For each position \mathbf{x}_i , three velocity components are sampled from a uniform distribution in the range $[0, v_{\text{esc}}]$. These components form the test velocity \mathbf{v}_{temp} . Additionally, a number k

is sampled from a uniform distribution within $[0, f_{\max}]$, where f_{\max} represents the maximum value of the velocity distribution $\text{VD}(\mathbf{x}_i, \mathbf{v})$. For a steady-state, spherical, and isotropic system, f_{\max} is given by $f_{\max} = \text{VD}(\mathbf{x}_i, \mathbf{0})$. The test velocity \mathbf{v}_{temp} is accepted as the velocity at \mathbf{x}_i if the condition $k < \text{VD}(\mathbf{x}_i, \mathbf{v}_{\text{temp}})$ holds and if the magnitude $|\mathbf{v}_{\text{temp}}| \leq v_{\text{esc}}$. If the condition is not satisfied, i.e., if $k > \text{VD}(\mathbf{x}_i, \mathbf{v}_{\text{temp}})$, then \mathbf{v}_{temp} is rejected, and the process is repeated. In case of a Plummer model Eq. 3.19, the DF is known analitically Eq. 3.22 and easily enables the computation of $\text{VD}(\mathbf{x}_i, \mathbf{v})$ for any \mathbf{v} .

3.3 Simulation parameters

In this section, I present the simulation parameters, including resolution (Section 3.3.1) and physical parameters, providing a more detailed description of those previously introduced (Section 3.3.2), summarizing them in Table 3.1. Finally, in Section 3.3.3 I discuss the tests performed to prepare the final model.

3.3.1 Resolution

In all simulations, the computational box is set to 40 pc. The maximum resolution achieved depends on the highest refinement level, which determines the smallest cell size that can be resolved. The grid is initially divided at the coarsest refinement level, and then AMR (Section 2.2.1) is applied, allowing for increased resolution in selected regions. In the performed simulations I consider different values for the minimum and maximum refinement level as follows:

- in the low-resolution simulation, I consider $l_{\min} = 4$ and $l_{\max} = 7$;
- then I consider a higher resolution case with $l_{\min} = 5$ and $l_{\max} = 8$.

The two maximum refinement levels correspond to different spatial resolutions, as increasing l_{\max} enables the resolution of smaller physical scales Δx , according to the relation:

$$\Delta x = \frac{L}{2^{l_{\max}}} , \quad (3.28)$$

where L is the size of the computational box (40 pc). Consequently, the values $l_{\max} = 7$ and $l_{\max} = 8$ correspond to spatial resolutions of 0.30 pc and 0.15 pc, respectively. The preliminary tests presented in this chapter have been performed with a maximum refinement level of $l_{\max} = 7$.

Achieving sub-pc resolution is essential to capture rapid, small-scale processes such as tidal shocks and the turbulent nature of SF (Renaud et al., 2013; Renaud, 2020). Only a few studies have achieved this level of detail to investigate the physical conditions in which star clusters originate, though they still face notable limitations. For example, while some simulations successfully model star cluster formation, the resulting cluster sizes are typically larger than observed. This discrepancy arises primarily from limited resolution (Ma et al., 2020). In some very high-resolution simulations, the stellar component is represented using stellar particles intended to approximate entire stellar populations (Kimm et al., 2016; Garcia et al., 2023).

However, as resolution increases, the reliability of sub-grid star formation models using particle-based approaches becomes more challenging.

3.3.2 Physical parameters

The first step is to define the physical parameters for the simulation to reflect realistic astrophysical conditions of the Galactic bulge and the GMC. It is essential for accurately modeling both the ambient medium and the infalling GMC. I adopted an initial homogeneous number density distribution for the ambient medium within the simulation box and imposed the density for the GMC four orders of magnitude higher with respect to the ambient medium, as anticipated in Section 3.2. The adopted values are based on relevant works from the literature [McKee & Ostriker \(1977\)](#), [Cox \(2005\)](#), [Tielens \(2005\)](#) and [Asplund et al. \(2021\)](#) for the metallicity. The specific values used in this thesis are summarised in Table 3.1.

Parameter	Adopted values
M_{FG}	$10^6 M_{\odot} - 10^7 M_{\odot}$
ρ_{GMC}	10^2 cm^{-3}
T_{GMC}	10^2 K
M_{GMC}	$\sim 2.35 \times 10^5 M_{\odot}$
Z_{GMC}	0.03
v_{GMC}	$10 \text{ km s}^{-1} - 20 \text{ km s}^{-1}$
ρ_{amb}	10^{-2} cm^{-3}
T_{amb}	10^4 K
Z_{amb}	0.001

Table 3.1: Summary of the physical parameters of the simulation for the ambient medium and the GMC. The parameters include: M_{FG} (stellar mass of the FG), ρ_{GMC} (density of the GMC), T_{GMC} (temperature of the GMC), M_{GMC} (mass of GMC), Z_{GMC} (metallicity of the GMC), v_{GMC} (x -velocity of the GMC), ρ_{amb} (density of the ambient medium), T_{amb} (temperature of the ambient medium), and Z_{amb} (metallicity of the ambient medium).

As previously mentioned, the conditions explored in this study differ from those in McKenzie & Bekki (2018). Their analysis considers various factors, including the impact parameter, relative velocities, the masses and sizes of the interacting systems, and the number of GMCs present in the bulge during a possible merger event. In contrast, this work focuses specifically on the velocity of the GMC (representing the infall velocity) and the mass of the FG.

The two velocities along the x -axis examined in this study are $v_{\text{GMC}} = 10 \text{ km s}^{-1}$ and a higher value of $v_{\text{GMC}} = 20 \text{ km s}^{-1}$, which falls within the range of $\sim 5 \text{ km s}^{-1}$ to 30 km s^{-1} investigated in their work. Due to computational constraints, only these two velocity values have been tested so far (see Chapter 5), but they already demonstrate that variations in the initial wind tunnel velocity significantly affect the results (see Chapter 4). In particular, it is important to note that the duration of each simulation varies depending on the chosen setup, more specifically, on the velocity considered. Two different evolutionary timescales are observed in these simulations, determined by the following relation:

$$time = \frac{(L + boxlen/2)}{v_x}, \quad (3.29)$$

considering the GMC size as approximately $L \sim 100 \text{ pc}$, and the selected box length as 40 pc . As a result, depending on the velocity of the infalling GMC, set to 20 km s^{-1} and 10 km s^{-1} , two distinct simulation times emerge: $\sim 6 \text{ Myr}$ and $\sim 12 \text{ Myr}$, respectively.

While, for what concerns the mass of the FG the values have been guided by observational and theoretical studies of systems like Terzan 5, in which it has been concluded that to retain SN ejecta within its potential well the system must have been much more massive in the past with respect to what we observe today (Lanzoni et al., 2010). For this reason, a higher initial mass of the system at the center would be able to produce a higher potential well, leading to the possibility of retaining gas. The higher mass system considered here ($10^7 M_{\odot}$) is meant to represent one of the possible progenitors of the most massive GGCs, which had suffered mass-loss during the cluster's early and long-term dynamical evolution (see D'Ercole et al., 2008).

3.3.3 Tests

To gain practical experience with the code, I conducted various tests, examining the results for each model component. These tests include the feedback model, focusing

on SN explosions and wind feedback, the star formation model, the delayed cooling model, and the wind tunnel set-up.

Here, in Figure 3.5 and Figure 3.6 I present the tests conducted for different values of v_{GMC} in a simulation box containing only the ambient medium, without FG stars, feedback, or star formation; this test was fundamental for the implementation of the wind-tunnel setup as in Calura et al. (2019). As shown in the Figure 3.5 each snapshot includes four sets 2D slice map showing a specific gas quantity: gas density (in g cm^{-3}), pressure normalized to the Boltzmann constant (k_B , in $\text{cm}^{-3} \text{K}$), temperature (in K) and the gas velocity along the x -axis (in km s^{-1}), from top to bottom, respectively. The selected slices are considered on the $x - y$ plane at $z = 0$ pc, with the GMC entering the simulation box from the x -axis and the center of mass of Terzan 5 FG stars initially at $(x, y, z) = (0 \text{ pc}, 0 \text{ pc}, 0 \text{ pc})$, i.e. at the center of the simulation domain, following Figure 3.2. The first row is showing gas density maps at different times, and considering the colorbar in the right side of the panels, it is possible to see that the highest density region (the gas from GMC) is the one entering from the left.

In Figure 3.7 and Figure 3.9 I present the performed tests on the equilibrium of the FG star system, and the results show maps of different quantities at different times. For simplicity, I report just three representative snapshots to have an idea of the equilibrium, which is maintained for the FG star system, in a relatively short (2 Myr) evolutionary time with respect of the results shown in Chapter 4. In this regard, we can observe that the two iso-density regions are colored cyan and orange, not varying significantly. Furthermore, Figure 3.8 and Figure 3.10 show the radial densities profiles of the FG stars being constant in function of time.

I performed the same check considering the FG system with $10^7 M_{\odot}$. However, comparing Figure 3.9 to Figure 3.7, it is evident that a lower initial mass, and consequently a shallower potential well, results in different results in the physical quantity maps.

After completing the initial set-up and conducting preliminary tests on individual simulation mechanisms, like the wind-tunnel and the stability of the system, all physical processes and components must be integrated. The *final model* is constructed by placing FG stars at the center of the simulation box, initially gas-free, with the GMC infalling from the left (see Figure 3.2 for a schematic description) and including star formation and feedback processes.

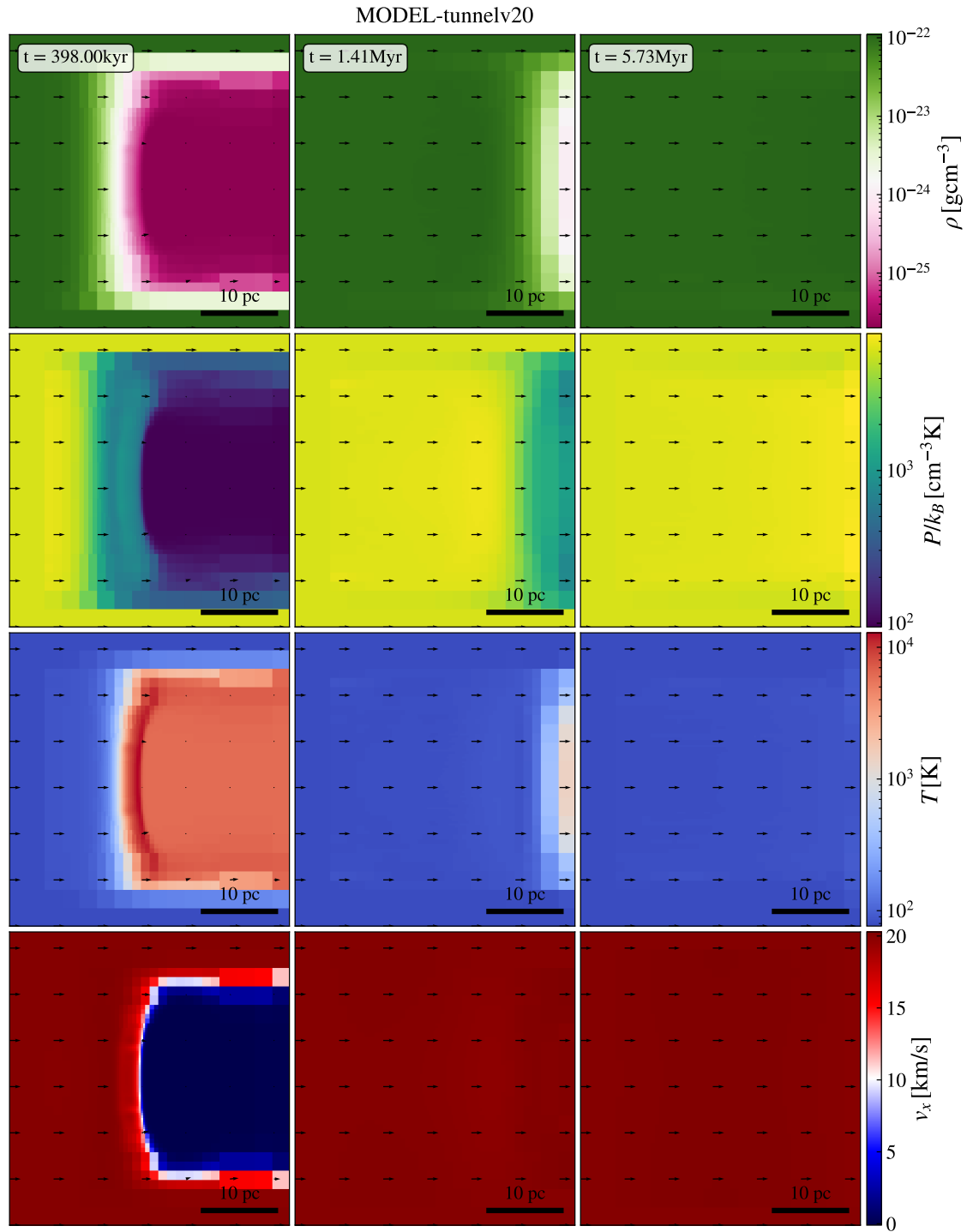


Figure 3.5: Test of the set-up for the GMC entering the simulation box, without feedback, star formation, or FG stars, with a velocity v_{GMC} , along the x -direction of 20 km s^{-1} . The arrows, representing the direction of the velocity field, go from the left toward the right part of the box. From top to bottom: 2Dslices maps of density, pressure, temperature, and velocity.

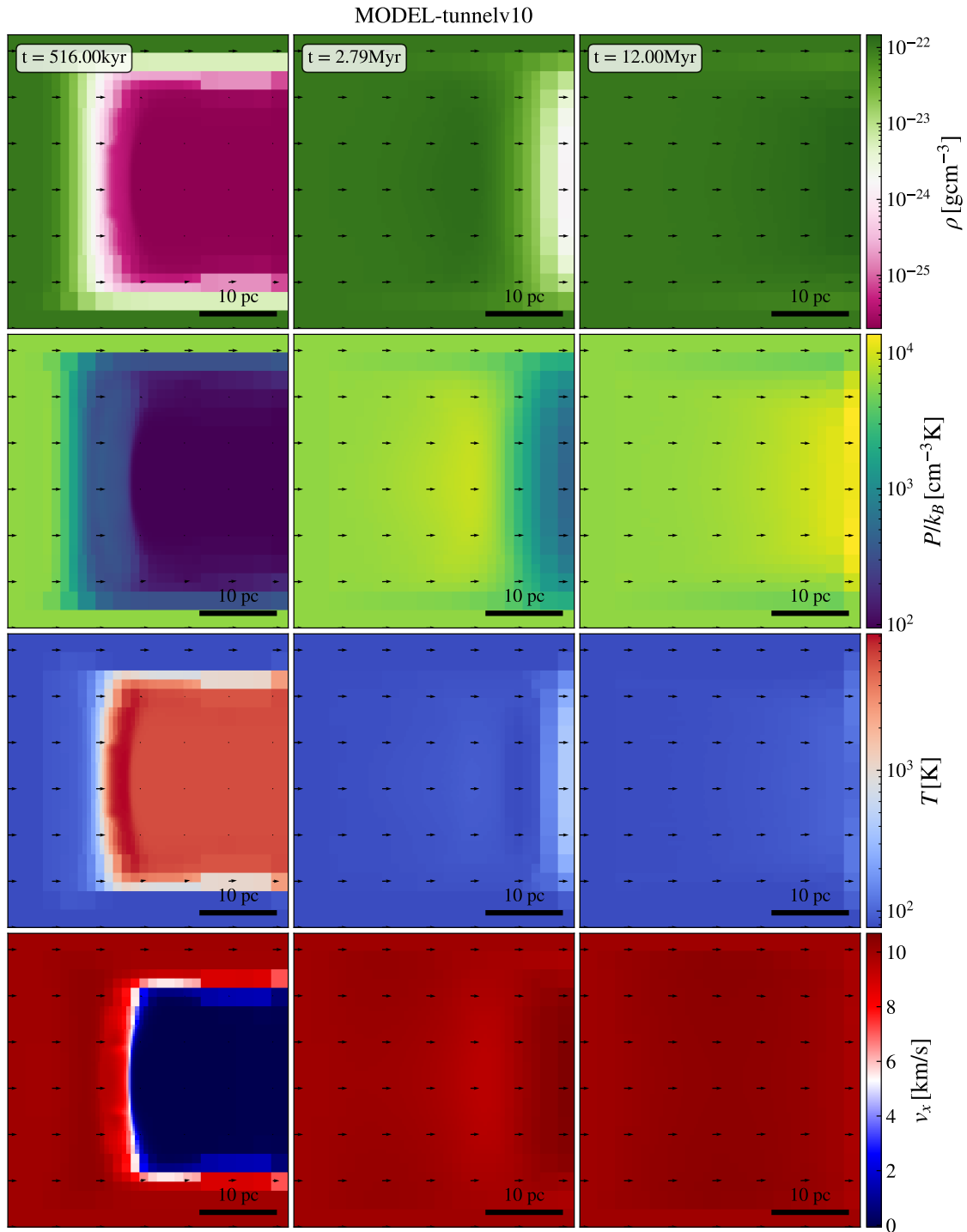


Figure 3.6: Same as Fig. 3.5, but considering an infalling velocity $v_{GMC} = 10 \text{ km s}^{-1}$.

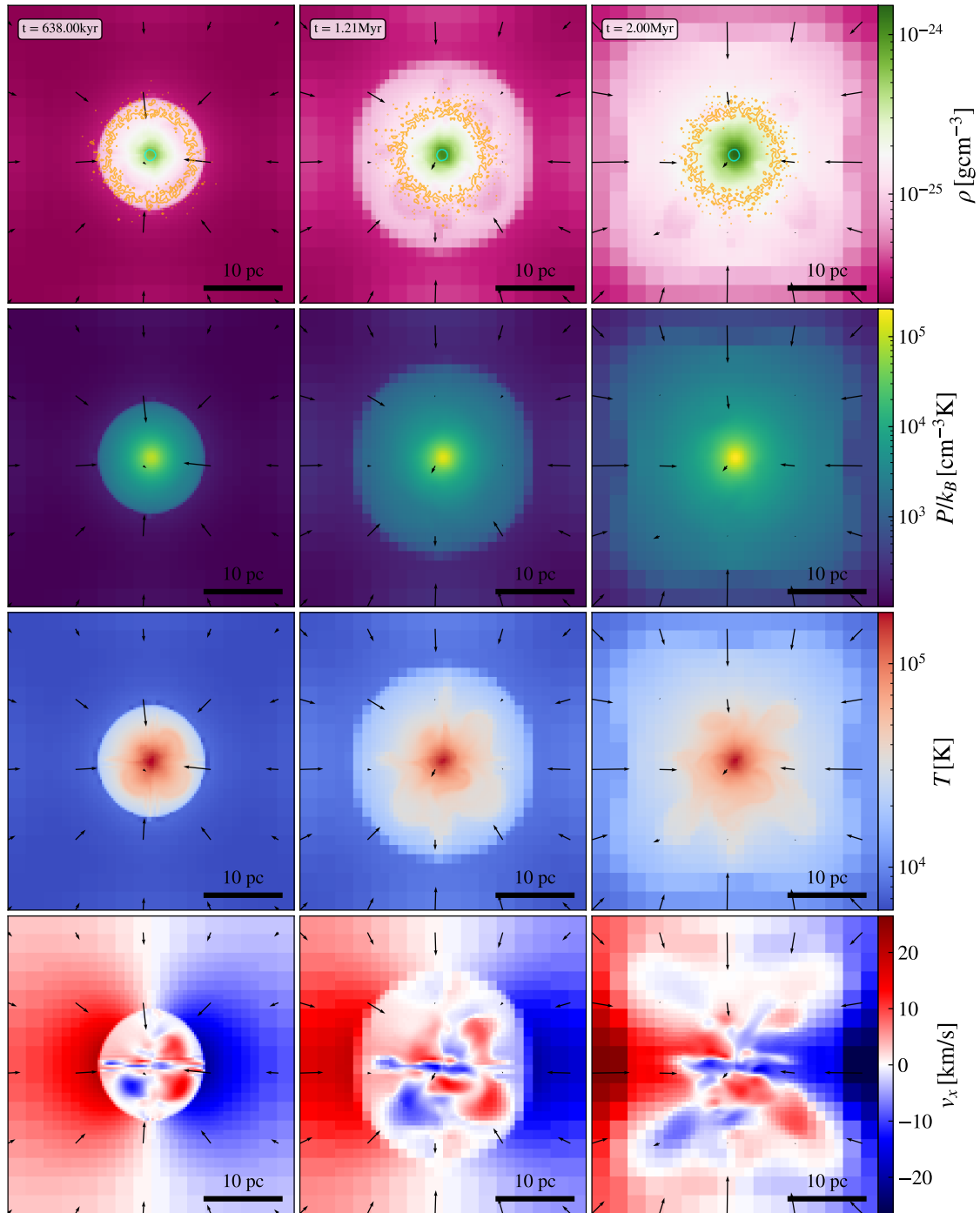


Figure 3.7: 2D Maps of the density, pressure, temperature and velocity along the x axis in a run including gravity with $M_{\text{FG}} = 10^6 M_{\odot}$, without considering star formation, cooling, or feedback mechanisms. In the first row the orange and cyan contours describe regions where the FG stellar density is $> 10^{-3}$ and > 0.5 times the maximum value. The first column represents the set-up of our initial conditions. The black arrows represent the velocity field along the x -axis.

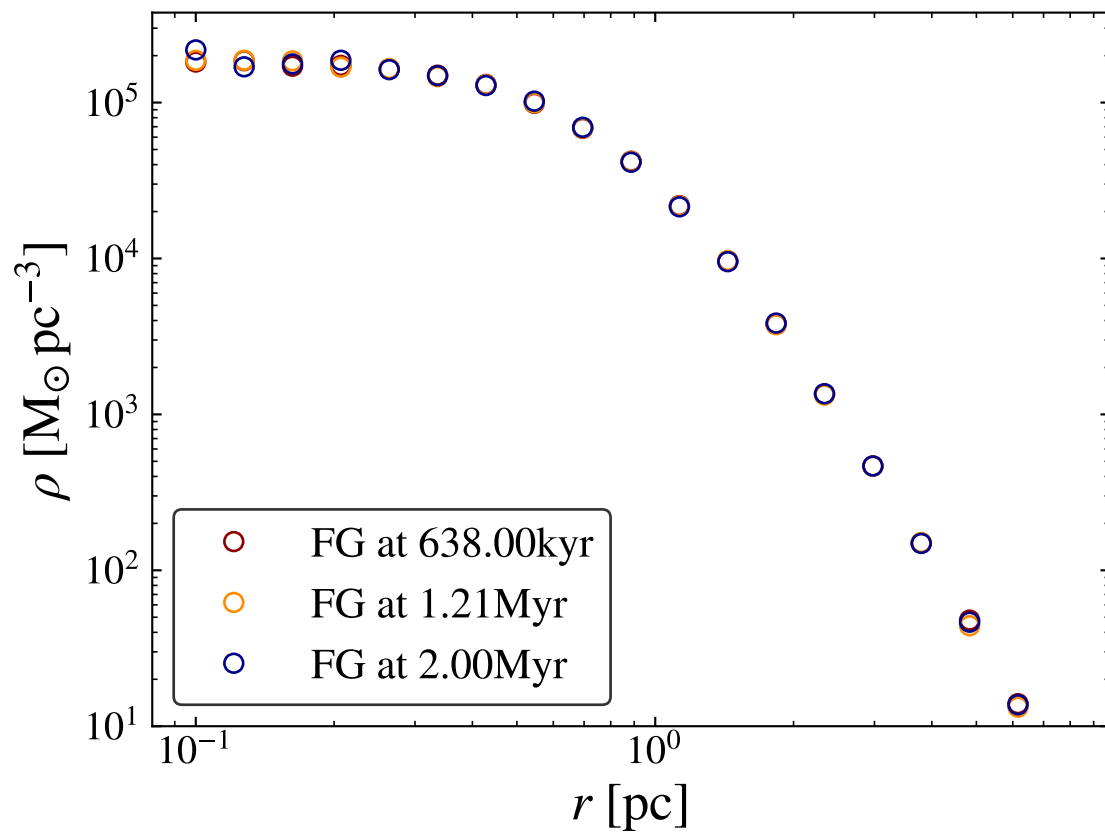


Figure 3.8: Density profiles at different snapshots (same of Fig. 3.7) to check the equilibrium of the FG stars system.

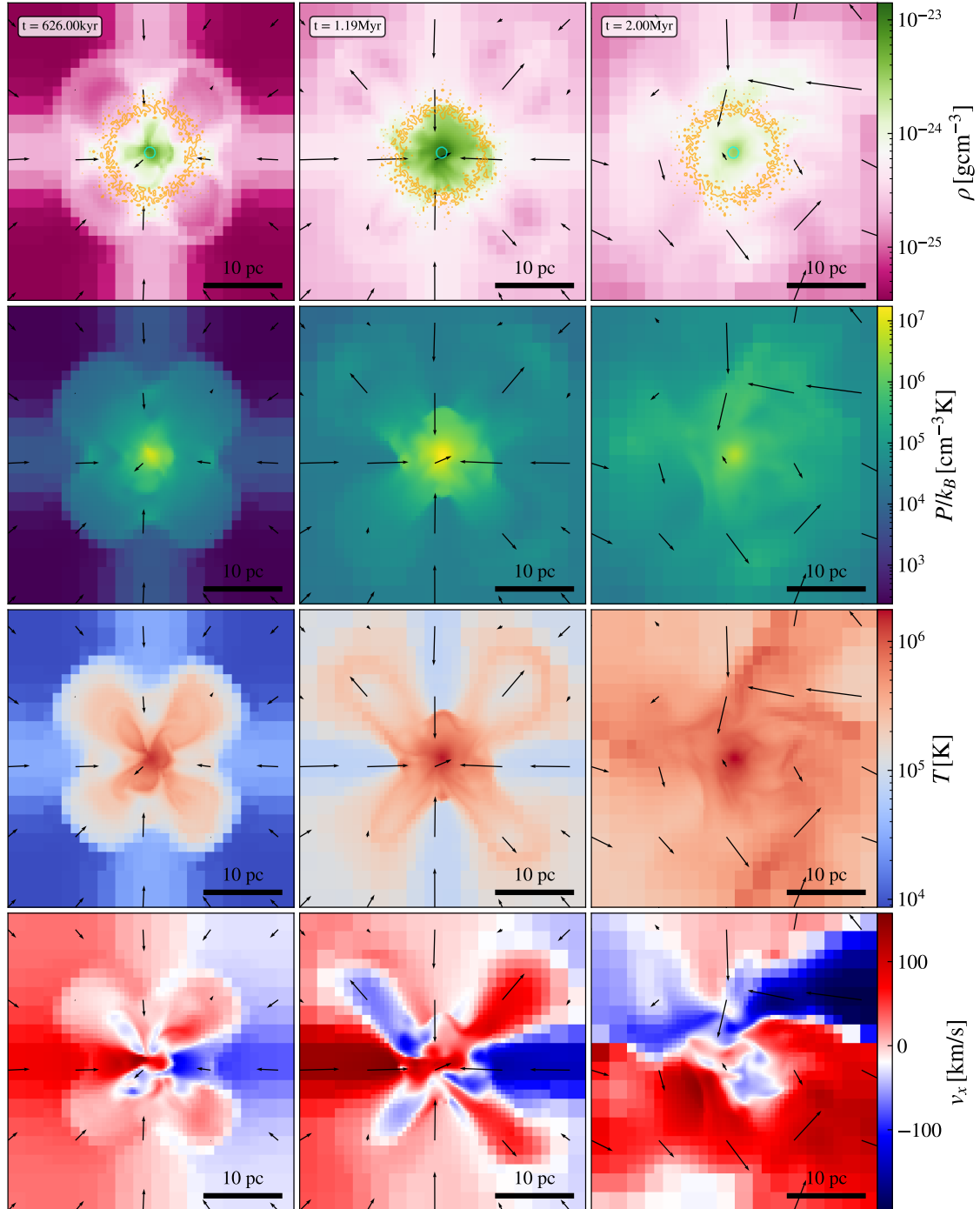


Figure 3.9: Same plot as 3.7, considering a mass $M_{\text{FG}} = 10^7 M_{\odot}$.

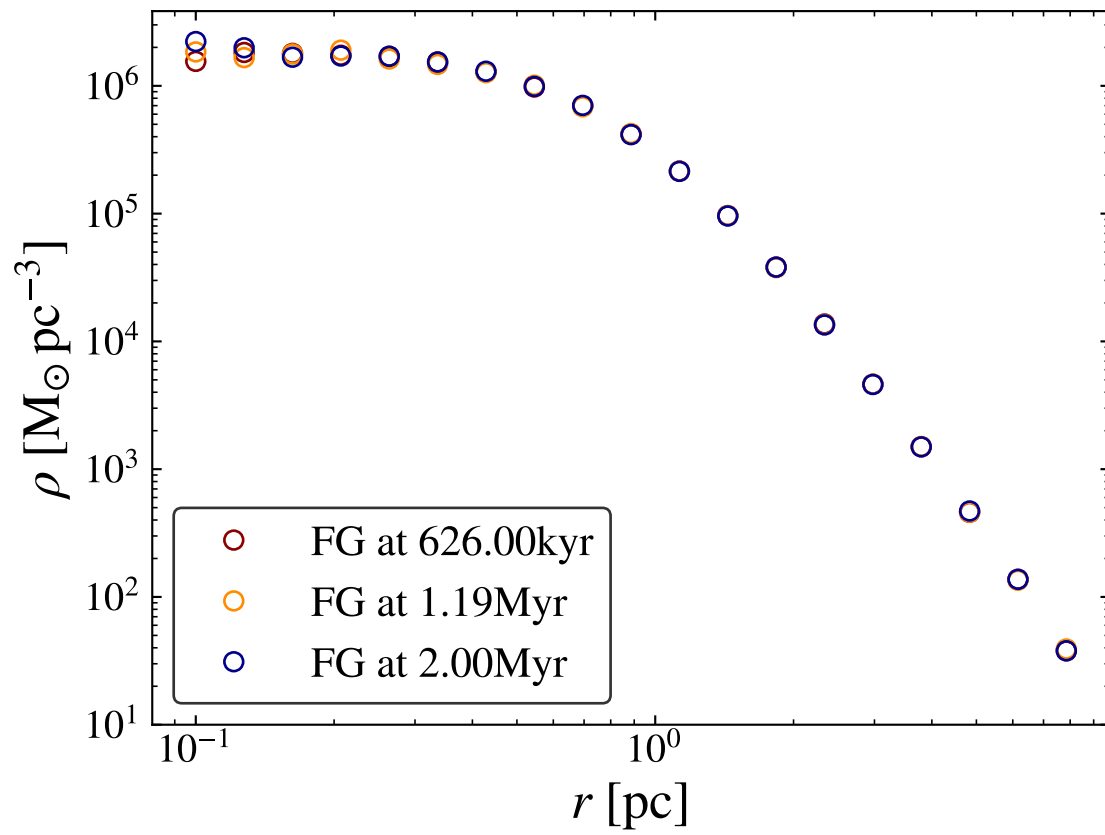


Figure 3.10: Same plot as 3.8, considering a mass $M_{\text{FG}} = 10^7 M_{\odot}$.

Chapter 4

Results

In this chapter, I present the results of the hydrodynamical simulations performed and described in the previous Chapter. Table 4.1 summarizes the main properties of all the simulations performed during this work, specifying the main input parameters (as the FG mass, the velocity of the GMC, the simulation resolution) and the main output parameters, as the mass of SG stars formed, M_{SG} . For the sake of brevity, in the following Sections I discuss only the results obtained from simulations performed at the maximum resolution (0.15 pc, corresponding at a maximum refinement level $l_{\text{max}} = 8$). Specifically, in Section 4.1 I focus on the models with a FG mass of $10^6 M_{\odot}$, while in Section 4.2 on the models with a FG mass of $10^7 M_{\odot}$. In Section 4.3 I present the radial density and cumulative mass profiles of the simulations at the maximum refinement level $l_{\text{max}} = 7$ (corresponding to a resolution of 0.30 pc), with the aim of performing convergence tests. In Section 4.4, I discuss the main limitations of the simulations implemented in this work, in particular those related to the model of star formation. Finally, in Section 4.5 I discuss my results comparing them with the literature.

4.1 Simulation model M6

For clarity, throughout this Chapter, I will refer to different simulation runs with the name MX-vY-LZ, where X represents the order of magnitude of the mass of the FG star system of Terzan 5 (6 or 7, corresponding to $M_{\text{FG}} = 10^6 M_{\odot}$ or $M_{\text{FG}} = 10^7 M_{\odot}$, respectively), Y the relative velocity of the GMC ($v_{\text{GMC}} = 10 \text{ km s}^{-1}$ or $v_{\text{GMC}} = 20 \text{ km s}^{-1}$) and Z the maximum level of refinement (7 or 8). In this Section I present the model M6-v10-L8 and M6-v20-L8. Some of the main parameters used to run these simulations are provided in the upper part of Table 4.1, along with the resulting SG masses M_{SG} formed in each different model.

Model name	M_{FG}	v_{GMC} [km/s]	l_{max}	Resolution [pc]	$M_{\text{SG}}[M_{\odot}]$
<i>M6 – v10 – L7</i>		10	7	0.3	7.10×10^1
<i>M6 – v20 – L7</i>	1×10^6	20	7	0.3	3.60×10^1
<i>M6 – v10 – L8</i>		10	8	0.15	9.37×10^2
<i>M6 – v20 – L8</i>		20	8	0.15	1.78×10^3
<i>M7 – v10 – L7</i>		10	7	0.3	2.45×10^3
<i>M7 – v20 – L7</i>	1×10^7	20	7	0.3	2.81×10^4
<i>M7 – v10 – L8</i>		10	8	0.15	6.16×10^2
<i>M7 – v20 – L8</i>		20	8	0.15	1.58×10^3

Table 4.1: Main parameters for the different simulations. In the top portion of the table I present the parameters of the simulations with a total mass of FG star of $10^6 M_{\odot}$, while in the bottom part I report the parameters corresponding to a total mass of FG star of $10^7 M_{\odot}$.

4.1.1 Gas Evolution Maps in the M6-v10-L8 model

In Figure 4.1 I present the maps of different hydrodynamical variables extracted from the M6-v10-L8 model. Each column corresponds to a different time, particularly $t \simeq 0.9$ Myr (left column), $t \simeq 4.47$ Myr (central column) and $t \simeq 11.8$ Myr (right column), in such a way to cover the entire simulation evolutionary time (12 Myr for this model, see Chapter 3). For reference, the theoretical position of the GMC infall front is given by $x = v_{\text{GMC}} \times t_{\text{snap}}$. Accordingly, the front is located at 10 pc from the left side of the box, in the first time shown, at the right edge of the box in the second time, and beyond the box in the third considered time, meaning that Terzan 5 is fully immerse within the GCM .

Each column corresponds to a set of four 2D slice maps showing a specific gas quantity: gas density (in g cm^{-3}), pressure normalized to the Boltzmann constant (k_B , in $\text{cm}^{-3} \text{ K}$), temperature (in K) and the gas velocity along the x -axis (in km s^{-1}), from top to bottom, respectively. The selected slices are considered on the $x - y$ plane at $z = 0$ pc, with the GMC entering the simulation box from the x -axis and the center of mass of Terzan 5 FG stars initially at $(x, y, z) = (0 \text{ pc}, 0 \text{ pc}, 0 \text{ pc})$, i.e. at the center of the simulation domain.

In Figure 4.1, the first snapshot at $t \sim 1$ Myr shows that although the gas infall has not fully started to cross the system yet, the GMC has already begun to experience a strong gravitational pull from Terzan 5 FG stars, which attracts the gas towards its central regions. The effect is clear looking at the gas velocity field overlaid in each panel and pointing towards the center of Terzan 5. This accretion is also visible by looking at the bottom panel, showing the v_x velocity map. Here, the positive velocities to the left (red-colored) result from the accretion of the GMC, while the negative velocities to the right (blue-colored) are driven by the accretion of material from the ambient medium on the right-hand side of the box. In a localized region at the center of Terzan 5 (~ 2 pc), the density and pressure start showing a substantial increase.

In the second snapshot, the gas is actively accreting toward the center, and the GMC front has crossed the center. The accretion can be appreciated by observing the compression and concentration of gas at center, where it has grown by different orders of magnitude, reaching a value of the order of $\sim 10^{-19} \text{ g cm}^{-3}$. The increase in density is followed by an increase in both pressure (up to $\sim 10^{10} \text{ cm}^{-3} \text{ K}$) and temperature (up to $\sim 10^5 \text{ K}$) in the same region.

In upper middle panel a gas clump originating from the center of Terzan 5 is

visible extending toward the right-hand side of the box. This stream is characterized by an high density ($\sim 10^{-19} \text{ g cm}^{-3}$) and low temperature ($< 10^4 \text{ K}$), and, as indicated by the velocity map in the bottom panels, it exhibits a negative v_x velocity, suggesting that it is infalling toward the center. By analyzing previous snapshots it is possible to appreciate the formation of an accretion column which this gas clump is the remnant of. The accretion column quickly dissipates, and it contributes to the resulting roundish shape observed on the right of the density, pressure and temperature maps.

Given the conditions of high density and low temperature, according to the star formation model adopted and described in Chapter 3, at the very center of the Terzan 5-like system, star formation is triggered. Here, the formation of SG stars can be observed in the top panels of Figure 4.1, where these newly formed objects are marked as red dots. At the center of the simulation, after the formation of the first massive stars ($> 8 M_\odot$), the gas is quickly heated by the injection of energy due to stellar winds. The sudden increase in temperature causes an increase in pressure which, in turn, causes this region to expand. As a result, in the last time reported, this region has expanded on a larger scale ($\simeq 10 \text{ pc}$ wide).

Examining the pressure and temperature panels of the second snapshot, a distinct curved region appears on the left-hand side of the box center. This region, characterized by higher temperature and pressure compared to the surrounding environment, suggests the presence of a shock between the infalling GMC and the gas already present in proto-Terzan 5. However, the pressure and temperature in this region remain lower than those found at the center of the box, where the gas is heated and at higher pressure and is going to interact with the accreting gas at lower temperature.

From the velocity panels, we observe that the velocity increases from the left toward the center, reaching a maximum (approximately 80 km s^{-1}) in the first panel from the left. In the last time, we observe a decrease in velocity when the infall has crossed the center of the box, reaching a value of approximately 20 km s^{-1} in the left bow-shaped region. In the central region, turbulence appears to dominate, resulting in a more complex velocity field.

In the final snapshot, it is evident, especially looking at the density map of Figure 4.1, that the FG star system's position has slightly shifted toward the rightmost side of the box due to its interaction with the infalling gas.

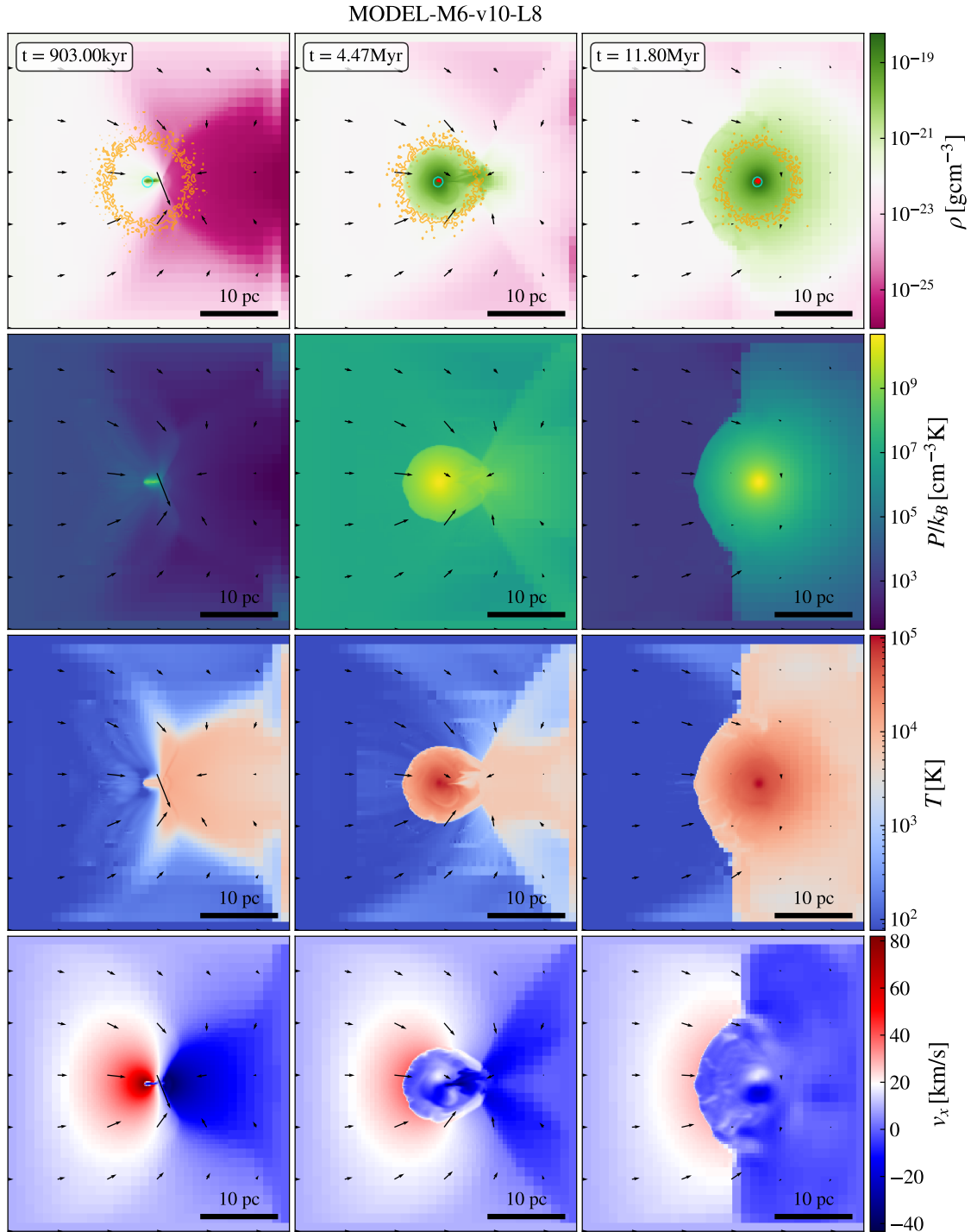


Figure 4.1: Evolution of the gas component in the simulation with $M_{\text{FG}} = 10^6 M_{\odot}$, considering a velocity $v_{\text{GMC}} = 10 \text{ km s}^{-1}$. The figure presents different evolutionary times, reported at the top left of each panel of the first row. Specifically $t \simeq 0.9 \text{ Myr}$, $t \simeq 4.47 \text{ Myr}$, and $t \simeq 11.8 \text{ Myr}$, from the left to the right columns, respectively. From top to bottom, slice 2D maps in the x - y plane at $z = 0 \text{ pc}$, showing slices of density, pressure, temperature, and v_x velocity. In the first row the orange and cyan contours describe regions where the FG stellar density is $> 10^{-3}$ and > 0.5 times the maximum density value, respectively. In the first row are reported, in red, the newly formed SG stars. The simulation box of each panel extends for 40 pc , with a reference scale in the bottom right. The black arrows in each panel represent the gas velocity field.

4.1.2 Gas Evolution Maps in the M6-v20-L8 model

The results from the M6-v10-L8 model are here compared to those obtained from the M6-v20-L8 model, with a relative velocity of the infalling GMC of $v_{\text{GMC}} = 20 \text{ km s}^{-1}$ (see Figure 4.2). The comparison is essential to understand how a different velocity influences the ability to form SG stars within Terzan 5. The simulation is evolved for a shorter time, 6 Myr, as discussed in Chapter 3. The times reported in Figure 4.2 are at $t \simeq 0.48 \text{ Myr}$, when the infall has not crossed the center of the simulation box yet, $t \simeq 2.75 \text{ Myr}$ (the infall front has crossed the simulation box entirely) and $t \simeq 5.63 \text{ Myr}$, almost at the end of the simulation.

In the first time considered, the front corresponding to the beginning of the GMC is approximately located at 10 pc from the left side of the box. At the center of the simulation box we can observe a small region ($< 1 \text{ pc}$) of increasing density, pressure and temperature, similarly to what happens in the model M6-v10-L8. Once again, this is clear observing the v_x map in the bottom panel, where a precise division of the simulation box in a positive velocity region (red-colored) is shown, directed toward the center from the left-hand side of the box and a negative velocity region (blue-colored) directed toward the center from the right-hand side of the box, with the center of Terzan 5 exactly between the two.

As time progresses ($t \simeq 2.75 \text{ Myr}$), the front fully crosses the simulation box, with gas accreting toward the center. The increased infall velocity at the center leads to the formation of a dense, high-pressure, and high-temperature region on the right side of the box, spanning approximately 10 pc. This region is characterized by a negative velocity directed toward the center, with a speed of -50 km s^{-1} . The density at the center has grown by several orders of magnitude, reaching $\sim 10^{-18} \text{ g cm}^{-3}$. This is further confirmed by the velocity field superimposed on the map, which clearly shows gas moving toward the center of Terzan 5.

As in the M6-v10-L8 model, we can witness to the formation of SG stars (red dots in the density maps) already from the $t \simeq 2.75 \text{ Myr}$.

At the final time, the high-density, pressure, and temperature region has expanded, as a consequence of the strong winds from the newly formed massive stars that keep heating the surrounding gas. The velocity distribution becomes more irregular, indicating increased turbulence, probably due the interaction between the infalling gas and the high-temperature gas injected into the medium by massive stars.

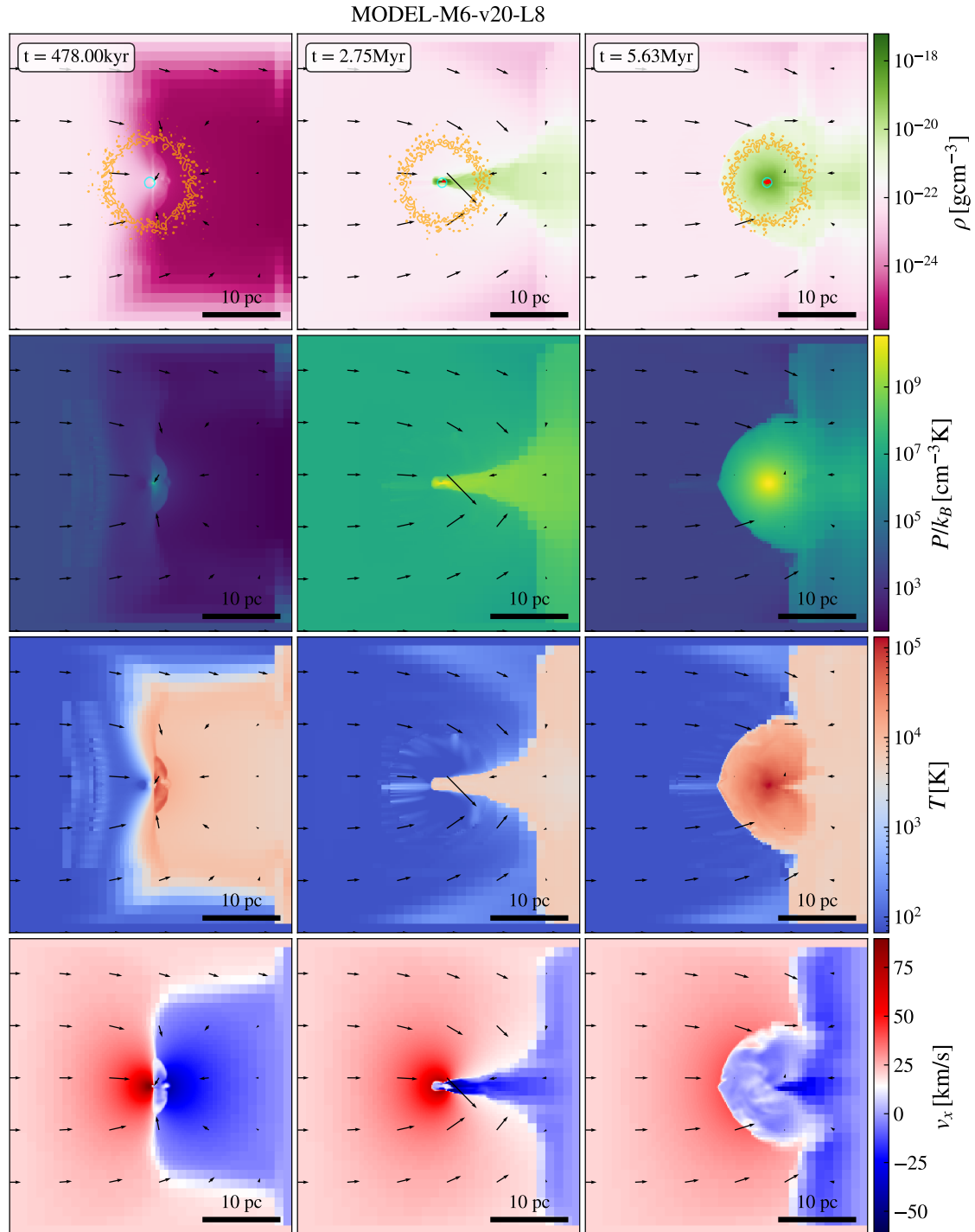


Figure 4.2: Same figure as Fig. 4.1 but considering $v_{\text{GMC}} = 20 \text{ km s}^{-1}$, the panels represent different evolutionary timescales. From left column to the right $t \simeq 0.48 \text{ Myr}$, $t \simeq 2.75 \text{ Myr}$ and $t \simeq 5.63 \text{ Myr}$.

4.1.3 Density and cumulative mass profiles

Figure 4.3 shows the radial density and cumulative mass profiles of the SG stars in the M6 models. At first, to compute the radial density and mass profiles, I recalculate the center of mass of Terzan 5 FG stars at each time. The choice is motivated by the fact that the system’s center of mass shifts as a result of the interaction with the GMC. To evaluate the center of mass, I used the shrinking sphere method (SSM; Power et al., 2003), an iterative scheme for determining the center of mass of a given set of particles with known masses and positions. At the iteration $i+1$, the algorithm computes the center of mass considering all the particles enclosed within a sphere centered on the i -th estimate of the center of mass, with radius $r_{i+1} = Kr_i$, where r_i is the radius of the sphere at the i -th iteration and $0 < K < 1$ is a constant, assumed 0.9 in this case. The algorithm stops when the sphere contains a predetermined number of particles, in my case the threshold is set to $0.05N = 5 \times 10^3$, where N is the number FG stars, 10^5 .

The method used to derive the density profiles is the following: I center the system at the center of mass previously calculated, then I divide the space into spherical shells, each with a width of Δr . The radial bins are evenly spaced in logarithmic intervals. For each shell, I sum the mass of the particles within the shell and divide it by the shell’s volume. In this way, I obtained the (volumetric) density as a function of the distance from the center of the system. In Figure 4.3a and Figure 4.3b, for each density measurement, I associate an error that is the Poissonian error. Specifically, the error on the i -th bin is calculated as

$$\sigma = \frac{\sqrt{N_{count,i}}}{V_{shell,i}} m_p \quad (4.1)$$

where $N_{count,i}$ is the number of particles in the i -th bin, m_p is the particle mass, equal for all the particles for the FG stars, while assumed as the mean mass per bin in the case of the SG stars, and $V_{shell,i}$ is the volume of the i -th shell. To derive the cumulative mass profiles, I calculated the sum of the mass inside the spherical radius r .

The bottom panel of Figure 4.3a shows the radial density profiles of the SG stars in the model M6-v10-L8, alongside the radial density profile of the FG stars (at $t = 0$ Myr). The bottom panel shows the corresponding cumulative stellar mass profile. The profiles are shown starting from the second snapshot of Figure 4.1.1. The reason behind this choice is given by the fact that in the first snapshot of Figure 4.1 there is no active star formation, consequently there is no density and

cumulative mass profile for the SG. This also holds for Figure 4.3b, focusing on the M6-v20-L8 model, which shows only the second and third evolutionary times with respect to Figure 4.2.

As shown in Figure 4.3a (bottom panel), the cumulative mass of the SG stars reaches a value of approximately $\simeq 10^3 M_{\odot}$, which remains nearly constant across the whole simulation, implying that star formation is not active. More specifically, this indicates that no new stars are formed after the second time. The only difference that it can be noticed is in the shape of the radial distribution, which is more centrally segregated at early times rather than at later times. This is also shown in Figure 4.1, where the red dots are more concentrated in the first evolutionary time compared to the last one. In the model M6-v20-L8 star formation is still active between the second and third snapshots reported, as demonstrated by the different values of the SG star total mass.

However, the total amount of SG stars formed during these two runs is negligible when compared to the total mass of the FG. The total mass of the SG stars is approximately $10^3 M_{\odot}$ in both the M6-v10-L8 and M6-v20-L8 models, against $10^6 M_{\odot}$ of the FG stars. These values are significantly different, more than 2 order of magnitude from the actual mass of SG stars observed in Terzan 5, which is $8 \times 10^5 M_{\odot}$. This finding challenges the previous perspective presented by McKenzie & Bekki (2018), where it was suggested that a SG star system comparable to the observed one could actually form in a scenario similar to the one presented.

4.1.4 SFHs

SFHs are essential for understanding the system's evolution. In particular, in the M6-v10-L8 and M6-v20-L8 models, as shown in Figure 4.4, star formation occurs in two distinct and short-lived episodes, each lasting less than 0.5 Myr. These episodes remain isolated in both simulations, with no indications of continuous or extended star formation. These periods start at different timescales in the different simulations, in particular star formation begins at ~ 2 Myr, in the M6-v10-L8 model and at ~ 2.5 Myr in the M6-v20-L8 model. In the latter, star formation begins later compared to the simulation with lower velocity, this delay arises because the higher velocity of the infalling gas inhibits its rapid accumulation toward the central region of the simulation box. As a result, the gas takes longer to reach the density and temperature conditions required for star formation, postponing the onset of the process.

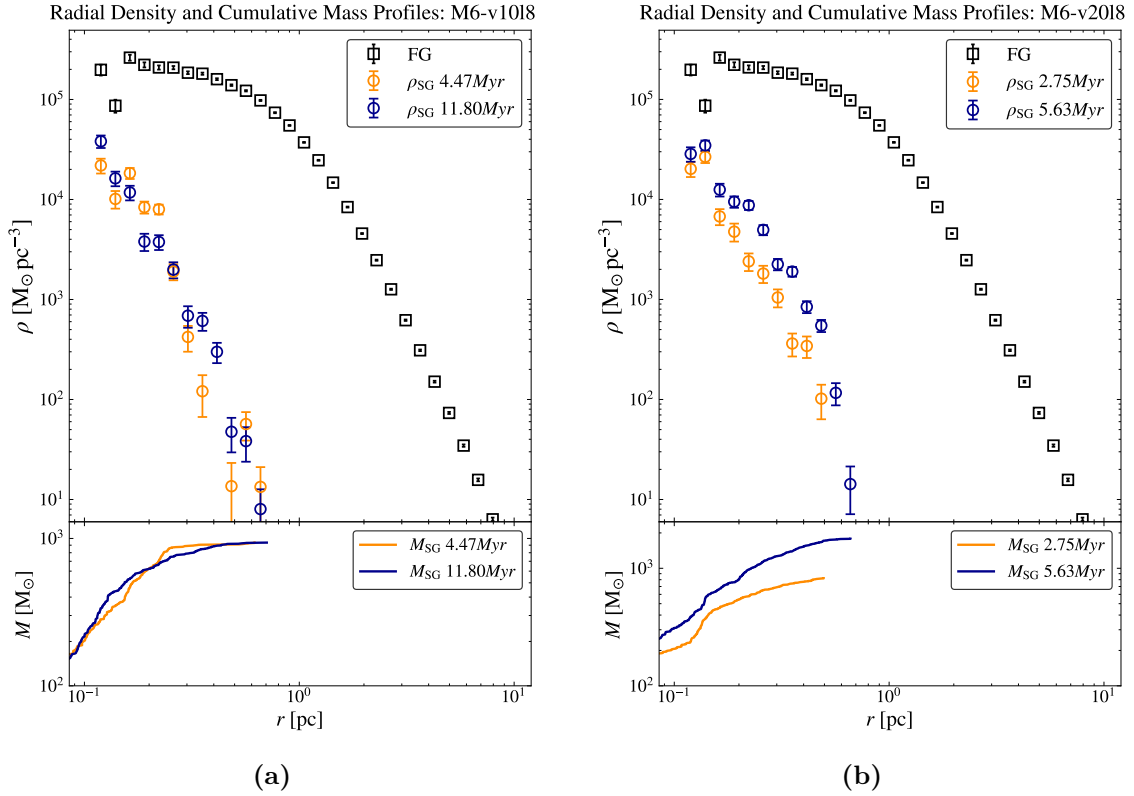


Figure 4.3: Comparison of density and cumulative mass profiles for models with a FG stars mass of $10^6 M_{\odot}$ (see Table 4.1) for two different GMC infall velocities: $v_{\text{GMC}} = 10 \text{ km s}^{-1}$ (left panels) and $v_{\text{GMC}} = 20 \text{ km s}^{-1}$ (right panels). *Top panels:* density profile of FG stars computed at $t = 0 \text{ Myr}$ (black squares), while orange, and blue circles correspond to SG stars at: $t \simeq 4.47 \text{ Myr}$, and $t \simeq 11.8 \text{ Myr}$ for the model M6-v10-L8 (left) and at $t \simeq 2.75 \text{ Myr}$, and $t \simeq 5.63 \text{ Myr}$ for the model at M6-v20-L8 (right). The density evolution of SG stars follows different growth rates depending on the GMC velocity. Error bars indicate Poissonian uncertainty. *Bottom panels:* Cumulative mass profiles computed at the same timescales as the density profiles in the top panels.

The subsequent quenching of star formation is, instead, due to the formation of three massive stars at the center of Terzan 5, with masses higher than $8 M_{\odot}$. Once these stars form, they begin to interact with the surrounding gas by releasing energy in the form of stellar winds that heat the surrounding medium, increasing its temperature and pressure, and causing the gas to expand. This expansion prevents further accumulation of gas, and the gas reaches higher temperature effectively suppressing subsequent star formation. The mass of the SG stars formed in the simulations is reported in Table 4.1. In my simulations, the difference in mass between the two populations - observed SG and simulated one - is nearly $10^3 M_{\odot}$, highlighting the limited efficiency in forming SG stars under these conditions and underscoring the strong impact of pre-SN feedback.

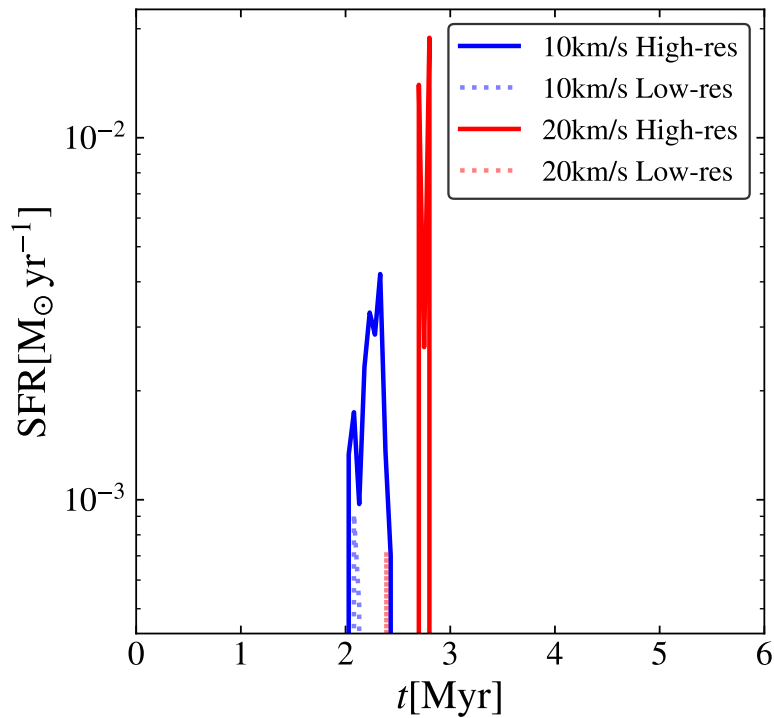


Figure 4.4: Star formation rate as a function of time for the simulation of model M6 considering the two velocities $v_{\text{GMC}} = 10 \text{ km s}^{-1}$ (in blue) and $v_{\text{GMC}} = 20 \text{ km s}^{-1}$ (in red). The results from the lower ($l_{\text{max}} = 7$) and higher ($l_{\text{max}} = 8$) resolutions are reported, respectively as dashed and solid lines.

4.2 Simulation model M7

In this Section I present the models M7-v10-L8 and M7-v20-L8, corresponding to simulations with a total stellar mass in FG stars of $10^7 M_\odot$, and velocities of 10 km s^{-1} and 20 km s^{-1} , respectively. The parameters used to run these simulations are provided in the bottom part of Table 4.1.

4.2.1 Gas Evolution Maps in the M7-v10-L8 model

In Figure 4.5 I report the maps of different hydrodynamical variables for the simulation with $v_{\text{GMC}} = 10 \text{ km s}^{-1}$. The snapshots are at different timescales, similarly to the ones considered for model M6-v10-L8 and M6-v20-L8 shown in the previous Section. For simplicity, I selected only three representative snapshots: $t \simeq 0.38 \text{ Myr}$, $t \simeq 6.88 \text{ Myr}$ and $t \simeq 11.1 \text{ Myr}$.

Figure 4.5 presents a scenario different from the ones previously discussed. Here, the deeper potential well generated by the FG stellar system significantly influences the evolution of the gas, leading to notable effects on the overall environment, the GMC and the star formation. At the first considered time, although the GMC has not even reached the system - the theoretical position of the front is at 4 pc from the left side - the gravitational pull of Terzan 5 is so intense that it starts attracting the gas from the ambient medium and from the GMC toward the central regions. All panels in the first column clearly show how the accreted gas is generating a flow that fuels the center of the FG stars system. Here, the density panel reveals an increase in density (up to $\sim 10^{-21} \text{ g cm}^{-3}$). This increase in density is followed by an increase in pressure ($\sim 10^8 \text{ cm}^{-3} \text{ K}$). As for the temperature, the gas flow exhibits a lower temperature ($\sim 10^4 \text{ K}$) compared to both the gas accreting from the right-hand side of the box and the gas accreting perpendicularly to the x -axis. Gas to the right-hand side reach higher temperatures (up to $\sim 10^6 \text{ K}$), due to heating by compression caused by the strong accretion.

The bottom-left panel illustrates the v_x velocity map, revealing a clear asymmetry in the gas dynamics. In the central region, gas velocities reach positive values up to 200 km s^{-1} , a strong indication of the intense gravitational attraction exerted by the massive FG stars. The region associated with higher temperatures exhibits a complex velocity structure, which arises from the interplay between two distinct accretion flows: the initial GMC gas infall and the concurrent accretion from the right-hand side of the box.

In the second snapshot the GMC has fully crossed the box. The gas velocity field reveals how the gas continues to accrete toward the center. This effect is particularly evident in a disk-like region in the center (~ 5 pc wide) of the x - y plane, where the gas density has increased by two orders of magnitude, reaching a value of approximately 10^{-19} cm $^{-3}$.

The physical conditions in the previously described disk-like region - characterized by high gas density and lower temperature - create a favorable environment for star formation. This is clear in the upper central and right panels of Figure 4.5, where newly formed stars are shown by red dots. Differently from the models discussed in the previous sections, where star formation is suppressed due to the formation of massive stars, in this case, the absence of such massive stars prevents the quenching of star formation due to feedback. The reason behind the lack of stars with mass higher than $8 M_{\odot}$ will be discussed in detail in Section 4.4, and it represents a limitation of the star formation model I adopted. Indeed, in some cases, the gas density within a given cell may be insufficient to form a star with a mass greater than $8 M_{\odot}$ at a given timestep, and this phenomenon, can result in an artificial truncation of the IMF. However, as will be addressed in the following Section, despite the lack of formation of massive stars, the mass of SG stars formed remains limited.

Between the last two snapshots, no significant differences are observed. The only noticeable variation, already discussed in the previous models, is the gradual displacement of the FG star system, as shown in the top row of Figure 4.5.

4.2.2 Gas Evolution Maps in the M7-v20-L8 model

This section is a description of the M7-v20-L8 model (Figure 4.6). In this case, the simulation has been evolved for 6 Myr, with the considered snapshots corresponding to $t \simeq 0.94$ Myr, $t \simeq 3.68$ Myr, and $t \simeq 5.94$ Myr. At the first time reported, the GMC front is at the center of the box, while in the other two snapshots it has already crossed the box.

From the first snapshot, an extended (~ 2 pc), high-density 10^{-18} cm $^{-3}$, and high-pressure region (up to $\sim 10^9$ cm $^{-3}$ K) forms at the center of the simulation box relatively soon, when the GMC front starts being accreted. Here, the gas temperature does not show a significant increase ($< 10^4$ K), while, on the right-hand side of the center, a sharp, elongated structure with negative velocity forms, which may appear as a small accretion flow. The left-hand side shows, instead, a more curved and diffuse structure due to the interaction with the infalling GMC

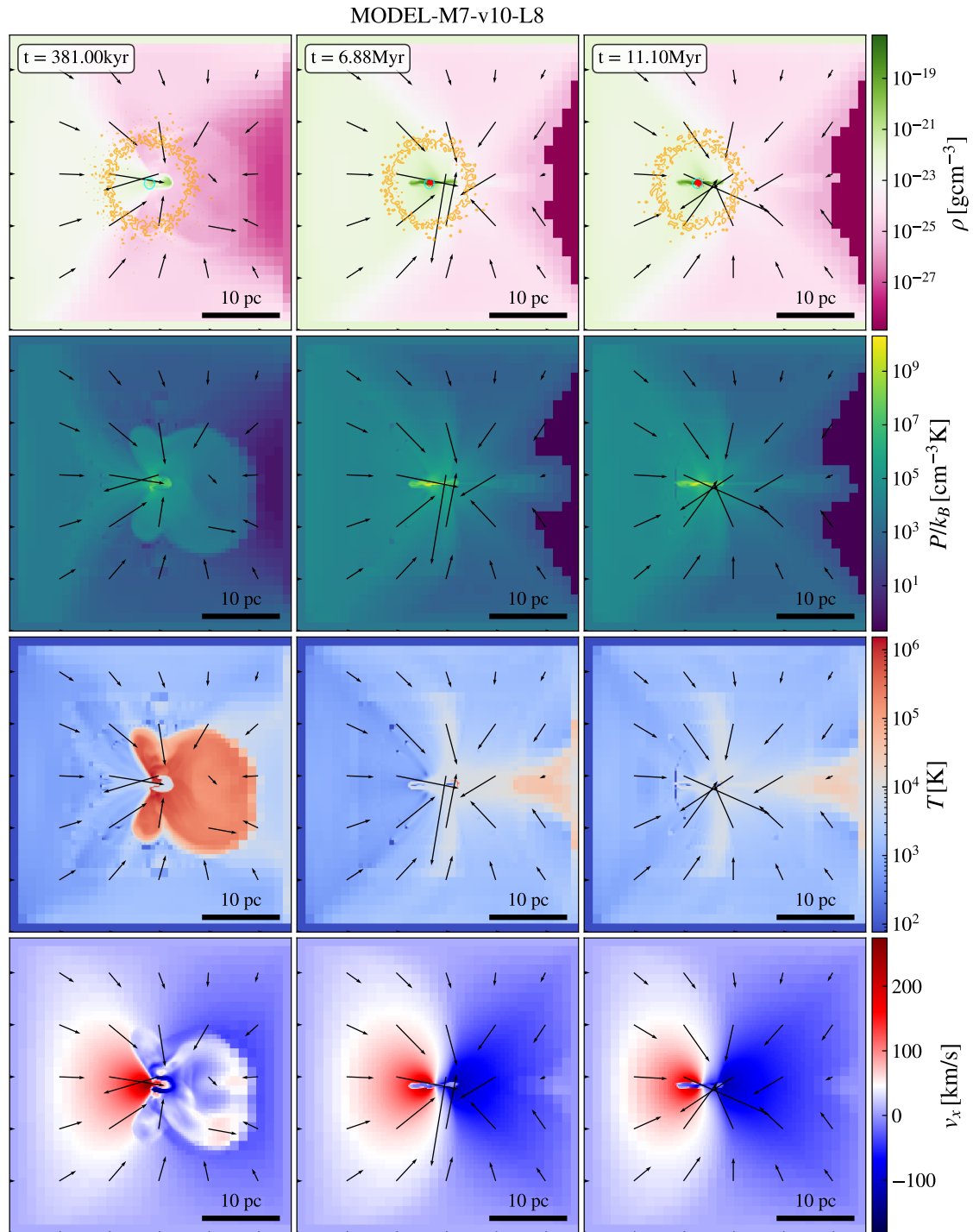


Figure 4.5: Evolution of the gas component in the simulation with $M_{\text{FG}} = 10^7 M_{\odot}$, considering a velocity $v_{\text{GMC}} = 10 \text{ km s}^{-1}$. The figure presents snapshots at different evolutionary times, reported in the top panel of each column. Specifically $t \simeq 0.38 \text{ Myr}$, $t \simeq 6.88 \text{ Myr}$, and $t \simeq 11.1 \text{ Myr}$, from the left to the right columns, respectively. From top to bottom, slice 2D maps in the x - y plane at $z = 0 \text{ pc}$, showing of density, pressure, temperature, and velocity are shown. In the first row the orange and cyan contours describe regions where the FG stellar density is $> 10^{-3}$ and > 0.5 times the maximum density value, respectively. In the first row are reported, in red, the newly formed SG stars. The simulation box of each panel extends for 40 pc , with a reference scale in the bottom right. The black arrows in each panel represent the gas velocity field.

from that side.

As observed from the gas velocity field, the gas is directed toward the center from both the left and right-hand sides of the box. The v_x velocity map shows a high positive velocity (up to 200 km s^{-1}) toward the center from the left-hand side, while a negative velocity (up to -100 km s^{-1}) from the right. It is interesting to note that the described region has a disk-like structure (on the x - y plane); actually, this structure forms at an earlier time ($t \sim 0.5 \text{ Myr}$) compared to the one presented here. This structure is further highlighted in the velocity panel, in which, even at the first reported time, it reveals a positive velocity region on the upper part (in red) and a negative velocity region on the lower part (in blue). This central structure remains almost unchanged between the second and third snapshots. In the third snapshot, the rotating disk becomes only more pronounced, as indicated by the v_x velocity map, which shows a clearer and more widespread division of velocities across the central region.

The disk is also evident looking at density and pressure panels, where it can be appreciated the formation of high density and pressure region (similar to the one observed at the first time step). This region has a size of approximately 4 pc. In the temperature panel, the values show a decrease as the gas spirals toward the center. As in the previously described model, these conditions - high density and low temperature - are crucial to triggering star formation. Specifically, the central region is where star formation is observed.

4.2.3 Density and cumulative mass profiles

Figure 4.7a shows the radial density profiles of SG stars. Unlike the gas maps discussed earlier, the evolutionary times reported here do not include the first snapshot shown in Figure 4.5. Instead, the first evolutionary times presented corresponds to the one in which star formation started, respectively second and third snapshot of Figure 4.5, allowing one to appreciate the radial density and cumulative mass profile.

As illustrated in Figure 4.7a and Figure 4.7b (bottom panels), the cumulative mass profiles exhibit a continuous increase, in contrast what is observed in the M6-L8 models. In the current scenario, the cumulative mass continues to grow throughout the entire evolutionary timeline, with a consistent and noticeable rise in mass. By further studying the SFHs in Section 4.2.4, we can observe that there is no formation of objects more massive than $8 M_{\odot}$ able to quench the star formation, as previously observed in Section 4.1. Nevertheless, the total SG mass formed in the two models,

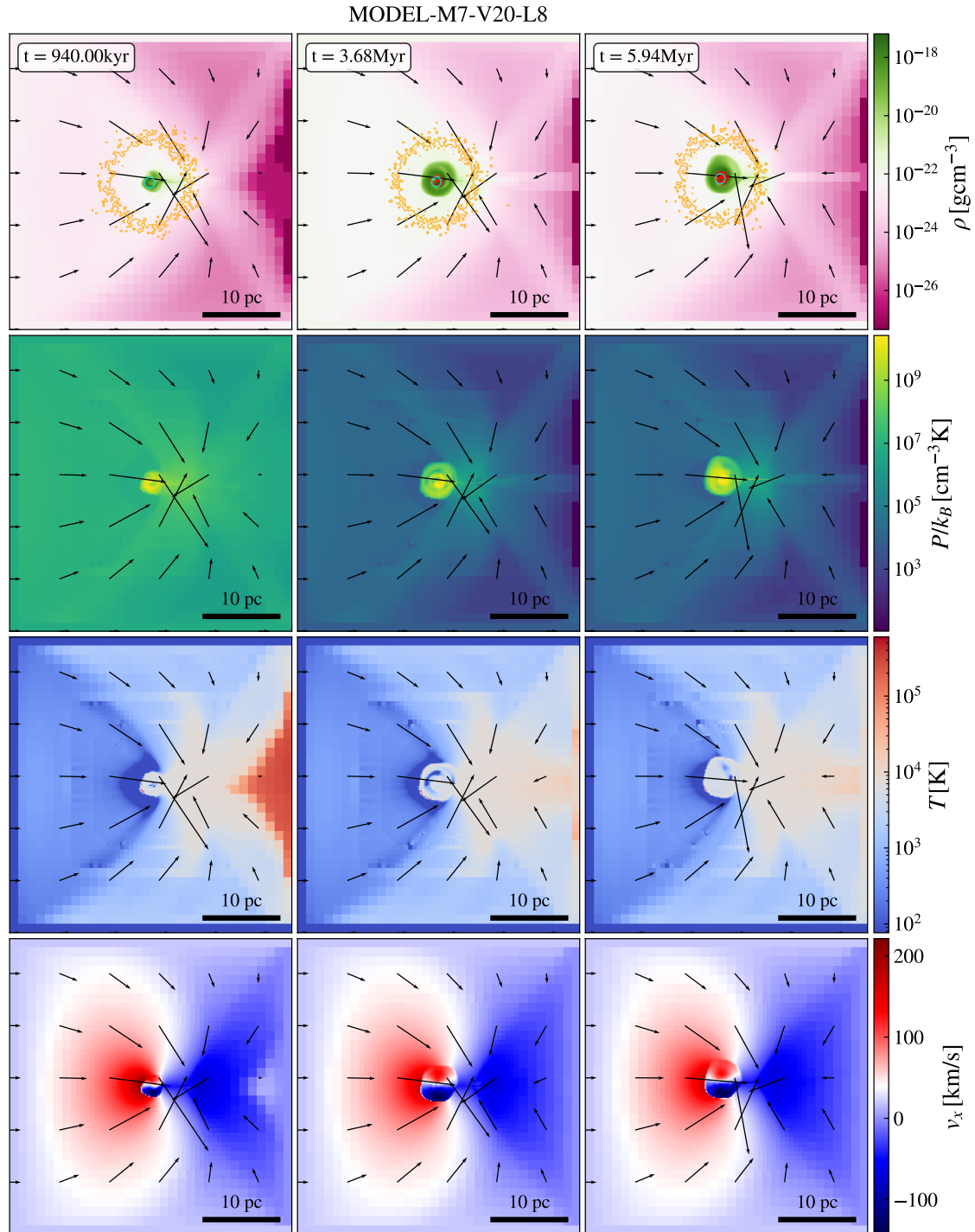


Figure 4.6: Same figure as Fig. 4.5 but considering $v_{\text{GMC}} = 20 \text{ km s}^{-1}$. The panels represent different evolutionary timescales, from the left column to the right one, $t \simeq 0.94 \text{ Myr}$, $t \simeq 3.68 \text{ Myr}$ and $t \simeq 5.94 \text{ Myr}$.

M7-v10-L8 and M7-v20-L8 (of the order $\simeq 10^3 M_\odot$), is not comparable to the FG of Terzan 5, and neither to the SG of Terzan 5 ($8 \times 10^5 M_\odot$) by more than two order of magnitude.

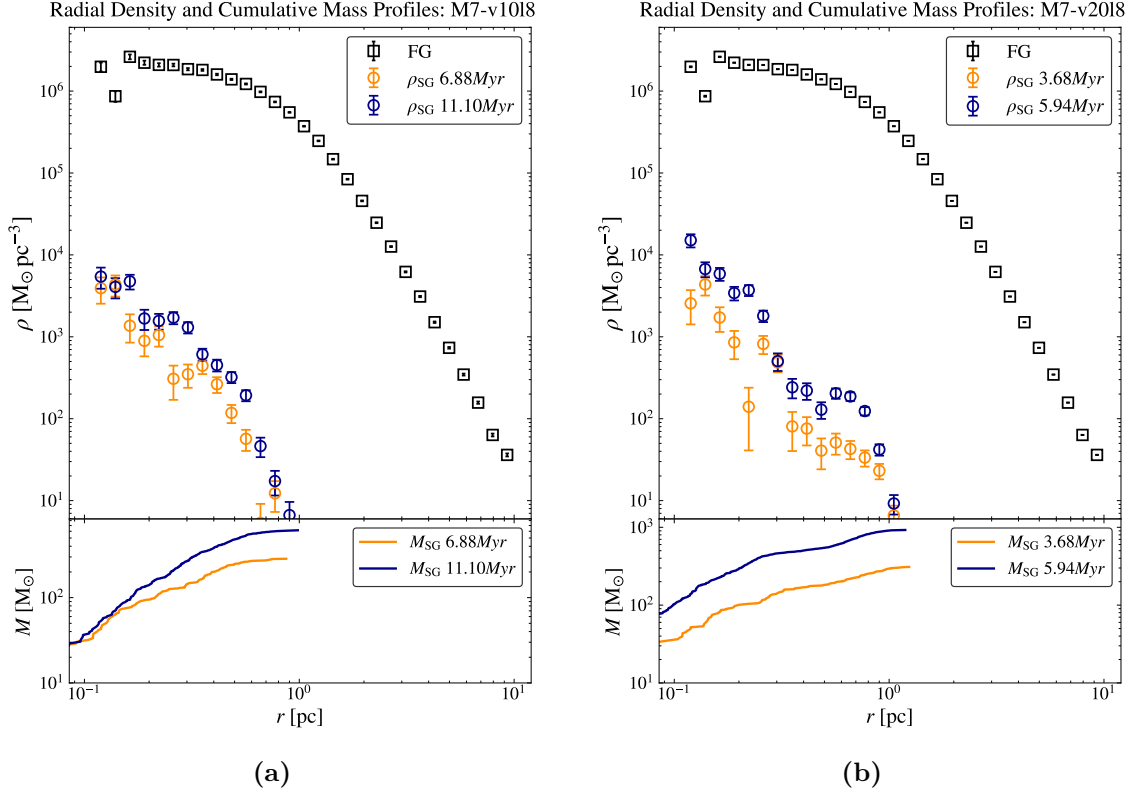


Figure 4.7: Comparison of density and cumulative mass profiles for model M7-L8 (see Table 4.1) for two different GMC infall velocities: $v_{\text{GMC}} = 10 \text{ km s}^{-1}$ (left panels) and $v_{\text{GMC}} = 20 \text{ km s}^{-1}$ (right panels). In both figures, the *top panels* show the density profile of FG stars computed at $t = 0 \text{ Myr}$ (black squares), while the red, orange, and blue circles correspond to SG stars at different evolutionary timescales: $t \simeq 6.88 \text{ Myr}$, and $t \simeq 11.1 \text{ Myr}$ for the model M7-v10-L8 (left) and at $t \simeq 3.68 \text{ Myr}$, and $t \simeq 5.94 \text{ Myr}$ for the model at M7-v20-L8 (right). The density evolution of SG stars follows different growth rates depending on the GMC velocity. Error bars indicate Poissonian uncertainty. *Bottom panels:* Cumulative mass profiles computed at the same timescales as the density profiles in the top panels, showing the accumulation of stellar mass over time.

4.2.4 SFHs

Figure 4.8 shows the SFHs for the set of simulations with $M_{\text{FG}} = 10^7 M_\odot$, for both the cases at $v_{\text{GMC}} = 10 \text{ km s}^{-1}$ and $v_{\text{GMC}} = 20 \text{ km s}^{-1}$. Here, in contrast to model M6, the SFHs are less intense and last longer. This is a confirmation that in these

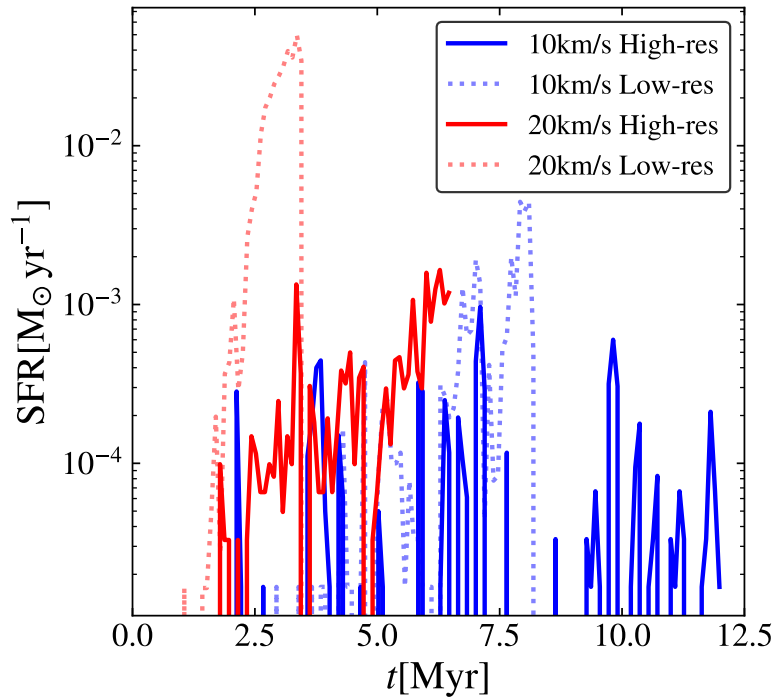
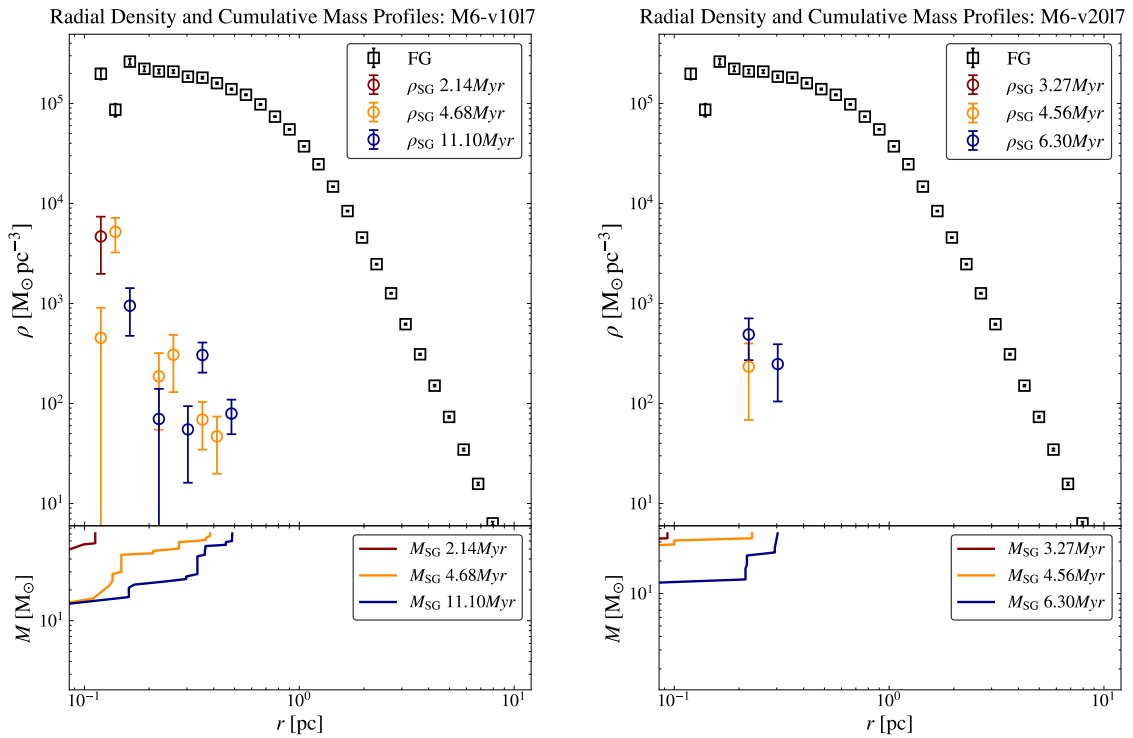


Figure 4.8: Star formation rate as a function of time for the simulation of M7 models considering the two velocities $v_{\text{GMC}} = 10 \text{ km s}^{-1}$ (in blue) and $v_{\text{GMC}} = 20 \text{ km s}^{-1}$ (in red). The results from the lower ($l_{\text{max}} = 7$) and higher ($l_{\text{max}} = 8$) resolutions are reported, respectively as dashed and solid lines.

cases no objects more massive than $8 M_{\odot}$ are formed, and thus a star formation quenching is not observed. Furthermore, the periods of star formation in both simulations are not isolated; they continue up to the maximum simulation times set, of the order of 6 Myr and 12 Myr, respectively. In these simulations, the onset of star formation is not delayed as in the previous set of models, it begins almost simultaneously, with the higher velocity simulation starting slightly earlier. This could be due to the deeper potential well generated by the system with $M_{\text{FG}} = 10^7$, in contrast to model M6, where star formation in the higher velocity simulation was delayed. Here, as in the previous M6-L8 models, the total mass of the SG stars (reported in Table 4.1) is not significant with respect to the FG and SG stars of Terzan 5; with differences of $\sim 10^2 M_{\odot}$.

4.3 Lower resolution models

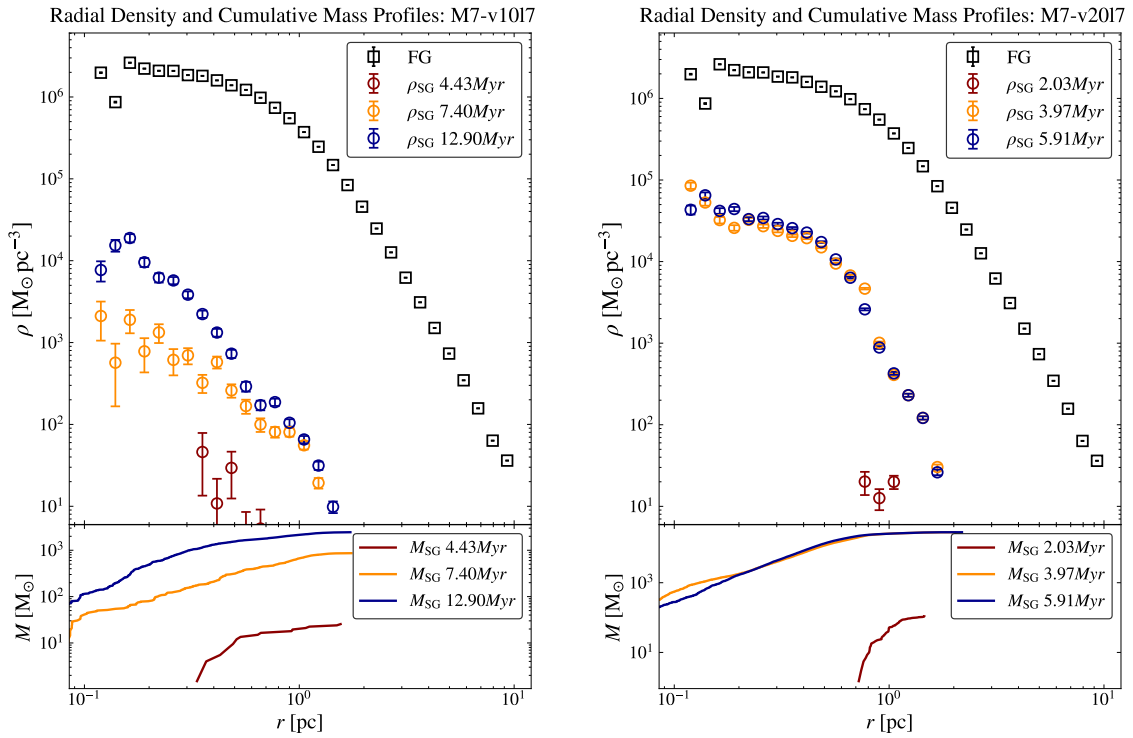
In this section, I report the tests related to the M6-L7 and M7-L7 models, specifically the radial density and cumulative mass profiles, as a convergence test with the L8 models. For both models, the two velocities $v_{\text{GCM}}=10 \text{ km s}^{-1}$ and 20 km s^{-1} have been studied. Here, for each of the models M6-v10-L7, M6-v20-L7, M7-v10-L7, and M7-v20-L7, star formation is able to form objects more massive than $8 M_{\odot}$, which consequently halts the subsequent star formation. Even in these cases, for each of the observed models, the total quantity of SG stars is not comparable to the observed SG population of Terzan 5. It is important to note that the plots shown are illustrative, and the results of these L7 simulations are found to be very similar to those of the L8 simulations, exhibiting comparable trends in both the radial density and cumulative mass profiles with a similar mass of SG stars.



(a) Density and cumulative mass profiles for model M6-v10-L7. The profiles are shown at three different evolutionary timescales: $t \simeq 2.14 \text{ Myr}$, $t \simeq 4.68 \text{ Myr}$, and $t \simeq 11.1 \text{ Myr}$.

(b) Density and cumulative mass profiles for model M6-v20-L7. The profiles are shown at three different evolutionary timescales: $t \simeq 3.27 \text{ Myr}$, $t \simeq 4.56 \text{ Myr}$, and $t \simeq 6.3 \text{ Myr}$.

Figure 4.9: Same as Figure 4.3 but for model M6-L7.



(a) Density and cumulative mass profiles for model M7-v10-L7. The profiles are shown at three different evolutionary timescales: $t \simeq 4.43$ Myr, $t \simeq 7.4$ Myr, and $t \simeq 12.9$ Myr

(b) Density and cumulative mass profiles for model M7-v20-L7. The profiles are shown at three different evolutionary timescales: $t \simeq 2$ Myr, $t \simeq 3.97$ Myr and $t \simeq 5.91$ Myr

Figure 4.10: Same as Figure 4.7 but for model M7-L7.

4.4 Limitation of the model

In this section, I briefly describe the main limitations of the model, which are related to the fact that, as presented in Section 4.2, in some cases star formation is unable to produce stars with masses higher than $8 M_{\odot}$. The problem can be easily visualized examining Figure 4.11 and Figure 4.12, where I show the IMFs of the SG stars formed in all the highest resolution simulations considered in this thesis.

Specifically, from Figure 4.11, we can observe the distinction in IMF for the M6-L7 (blue histogram) and M6-L8 (red histogram) models. Here, the comparison should be done with respect to the Kroupa IMF (black line reported in Figure 4.11). The model shows an overproduction of low-mass stars ($2 M_{\odot} \leq M \leq 3 M_{\odot}$) with respect to the analytic Kroupa (2001) IMF (described in Section 3.1.1); at higher masses, these differences become more evident in all models, regardless of the FG mass and relative velocity. The Kroupa IMF is not correctly reproduced, with some mass bins not being sampled at all. Furthermore, the IMF seems truncated, since stars more massive than $10 M_{\odot}$ are absent.

Similar differences between the analytic IMF and the models are visible in Figure 4.12b, where the discrepancy at the largest masses is even more serious.

To improve the modeling of the star formation process, a different type of star formation implementation via *sink particles* is required. In this method, a contracting high-density region is replaced by a single Lagrangian particle once the numerical resolution limit in the simulation is reached (Bleuler & Teyssier, 2014). Despite the absence of massive star formation ($> 8 M_{\odot}$), the total mass of SG stars formed in the M7-L8 models remains limited. This leads to the conclusion that the scenario described in hypothesis (4) (Section 1.4) is not a feasible mechanism for generating the SG of Terzan 5.

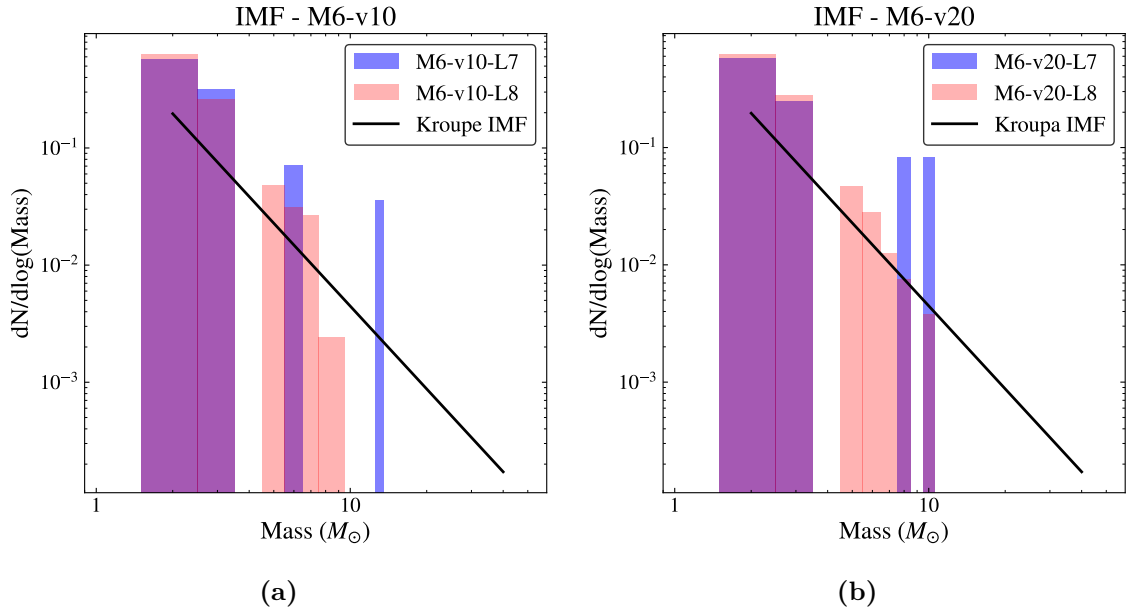


Figure 4.11: IMF of the SG stars of the models with a FG stars mass $10^6 M_{\odot}$. On the left, the simulations with relative velocity $v_{\text{GMC}} = 10 \text{ km s}^{-1}$ model, and on the right, the simulations with relative velocity 20 km s^{-1} . Different colors represent different maximum refinement level: 7 (blue histogram) and 8 (red histogram). The black curve represents the high-end mass tail of a Kroupa (2001) IMF.

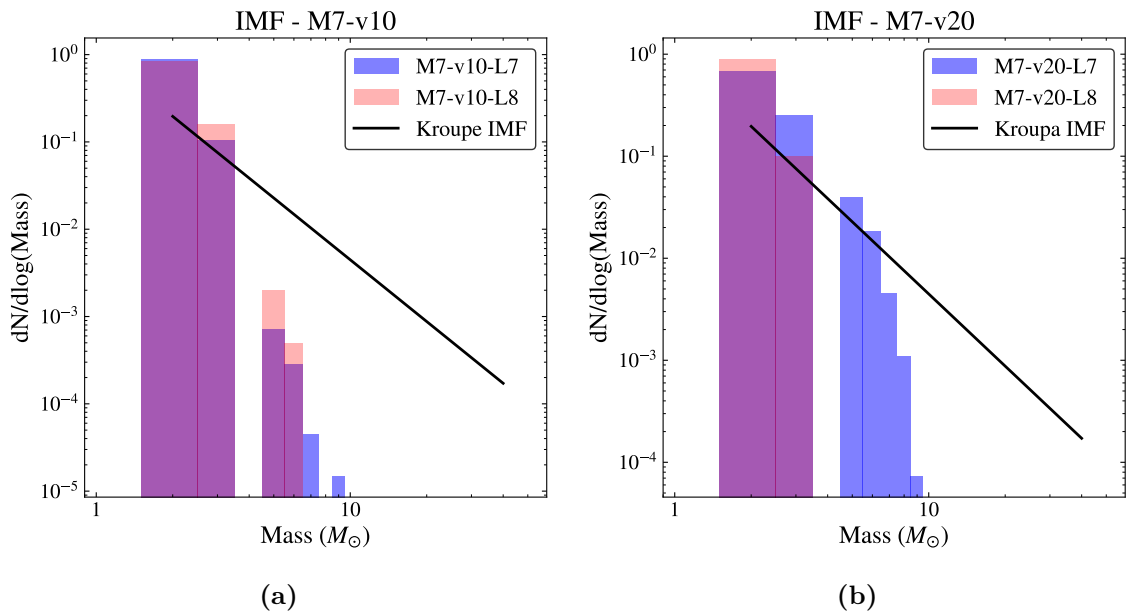


Figure 4.12: Same figure as Figure 4.11, considering the M7 models.

4.5 Comparison with McKenzie & Bekki (2018)

As presented in Section 1.4, this thesis aims to model the possible formation of the SG stars within Terzan 5 as the result of the interaction and accretion of a GMC. This work takes direct inspiration from McKenzie & Bekki (2018), building upon their simulations and introducing several key modifications as variations in the feedback model by accounting for pre-SN feedback (see Section 3.1.3), which was neglected in their study, and implementing the formation of individual stars. Given this strong connection, a direct comparison with McKenzie & Bekki (2018) is necessary.

Compared to the work of McKenzie & Bekki (2018), the implementation of pre-SN feedback is a fundamental ingredient. As we have shown throughout this Chapter - particularly in the models with a FG star mass of $10^6 M_{\odot}$ - the quenching of the star formation process is due to the formation of massive objects ($> 8 M_{\odot}$). These massive objects emit strong stellar winds that inject energy into the surrounding gas. This process heats the dense regions where star formation would typically occur, increasing its temperature and turbulence. As a result, the conditions required for star formation are no longer met.

The SFHs and cumulative mass profiles of the M6 models clearly show that star formation was halted relatively soon after the GMC passed through the existing FG star system. For the M7 models, even if star formation is not immediately quenched, it continues at a rate that is still insufficient to form a SG stars comparable to the one observed in Terzan 5, as demonstrated by Figure 4.7a and Figure 4.8. For comparison, in Figure 4.13 I report the SFH of the fiducial model M1 from McKenzie & Bekki (2018). This model considers an initial FG mass of $\sim 1 \times 10^7 M_{\odot}$, an infalling GMC of approximately $10^6 M_{\odot}$, and an infall velocity of $v = 20 \text{ km s}^{-1}$. These parameters are comparable to those adopted in model M7-v20 of this thesis. However, as can be observed from the Figure 4.13 the SFH is prolonged (up to 14 Myr) and reaches peak rates as high as $0.7 M_{\odot} \text{ yr}^{-1}$, exceeding those obtained in my models, always below $10^{-2} M_{\odot} \text{ yr}^{-1}$. Additionally, for completeness, in Figure 4.14 I also report the SFH of the fiducial model M2 from McKenzie & Bekki (2018), which corresponds to an initial FG star mass of $\sim 3 \times 10^6 M_{\odot}$, a GMC of $\sim 10^6 M_{\odot}$, and an infall velocity of $v = 10 \text{ km s}^{-1}$, similar to the model M6-v10 presented in this work. In Figure 4.14, the SFH is concentrated between 3 and 11 Myr, reaching peaks up to $3 M_{\odot} \text{ yr}^{-1}$, significantly higher than the $10^{-2} M_{\odot} \text{ yr}^{-1}$ obtained in my models.

In fact, in contrast to the simulations presented here, their results show the formation of a SG, with a mass of $\sim 1.4 \times 10^5 M_{\odot}$ for model M1 and $\sim 2.2 \times 10^5 M_{\odot}$ for model M2, which is more than two orders of magnitude larger than the values obtained in this thesis. This provides clear evidence that their model, which does not account for pre-SN feedback, leads to significantly different outcomes in terms of SG formation.

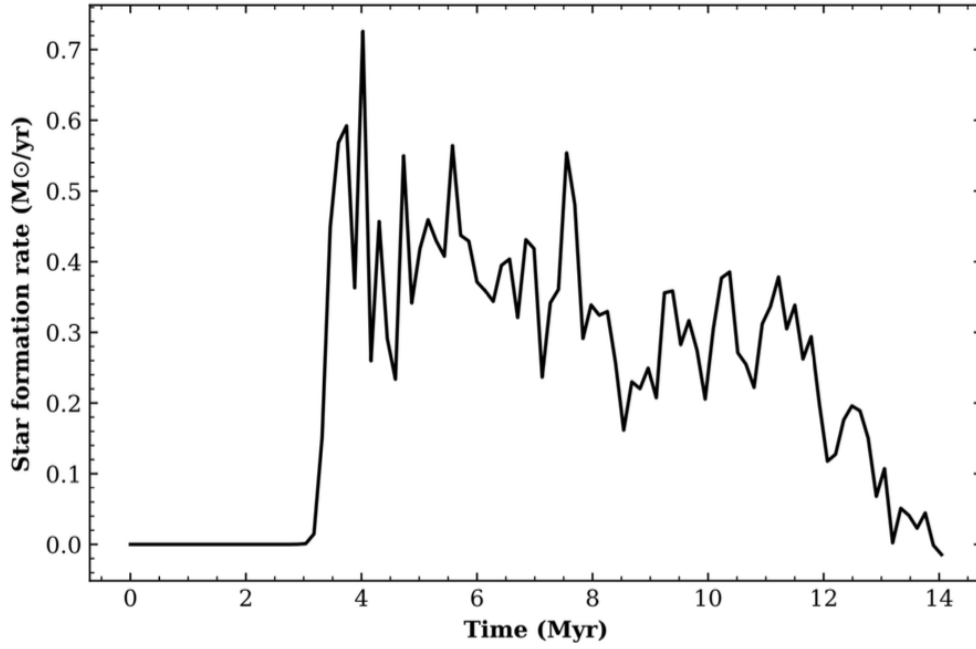


Figure 4.13: SFH of McKenzie & Bekki (2018) fiducial model M1. The simulation is evolved for 14 Myr, the GMC has a mass of the order of $10^6 M_{\odot}$, an initial FG mass of $\sim 1 \times 10^7 M_{\odot}$, and a relative initial velocity between Terzan 5 and the GMC of $v_{\text{GMC}} = 20 \text{ km s}^{-1}$.

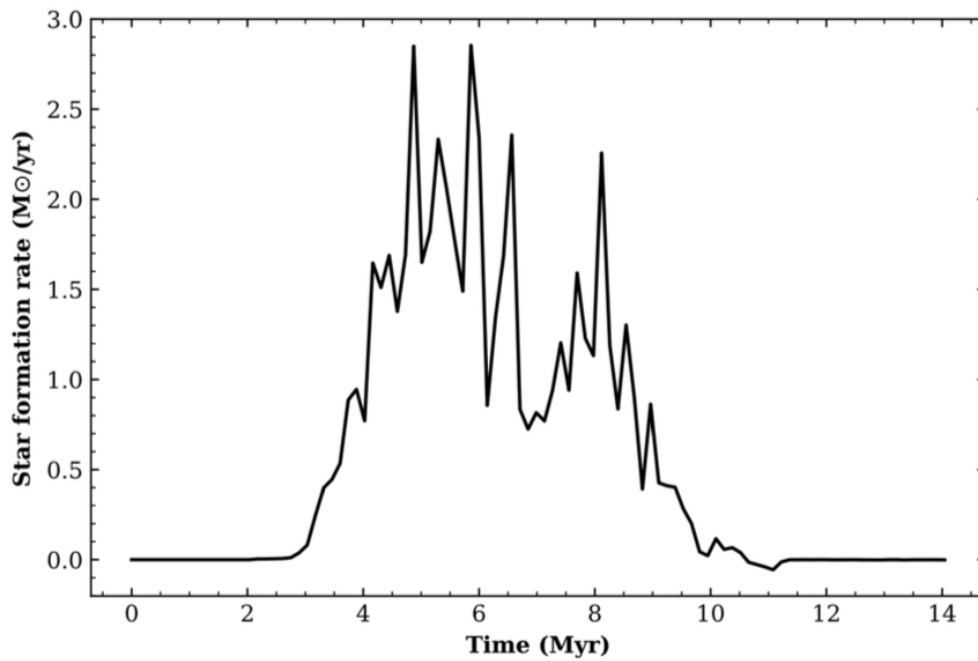


Figure 4.14: SFH of McKenzie & Bekki (2018) fiducial model M2. The simulation is evolved for 14 Myr, the GMC has a mass of the order of $10^6 M_{\odot}$, an initial FG mass of $\sim 3 \times 10^6 M_{\odot}$, and a relative initial velocity between Terzan 5 and the GMC of $v_{\text{GMC}} = 10 \text{ km s}^{-1}$.

Chapter 5

Conclusions

5.1 Summary

In this work, I have presented the results of detailed hydrodynamical N -body simulations aimed at exploring the possibility that the super-solar ($[\text{Fe}/\text{H}] = +0.3$), young (4.5 Gyr-old), and massive ($M = 8 \times 10^5 M_{\odot}$) SG population observed in the stellar system Terzan 5 was originated by the accretion of a GMC onto a genuine GC (hypothesis 4 in Section 1.4). This hypothesis was originally proposed and supported by hydrodynamical simulations by [McKenzie & Bekki \(2018\)](#). However, while their work is limited by the absence of the pre-supernova feedback - a process crucial for the evolution of massive clusters and star-forming regions - the simulations presented here represent a significant improvement by incorporating this mechanism in the form of feedback from winds from massive stars ($> 8 M_{\odot}$).

After describing the numerical methods implemented in the customized version of the hydrodynamical N -body code RAMSES (in Chapter 2), in Chapter 3 I outlined the initial conditions used to perform the 8 simulations described in Chapter 4. The simulations are divided as follows:

- four simulations that have been performed at a maximum physical resolution of 0.15 pc, corresponding to a maximum refinement level of $l_{\text{max}} = 8$ (here

labelled L8), given a box of a 40 pc size;

- four simulations at a maximum physical resolution of 0.30 pc, corresponding to a maximum refinement level of $l_{\max} = 7$ (labelled L7) to assess convergence.

The simulation set-up, including the configuration of the simulation box, its resolution, and the initial physical conditions of both the GMC and the proto-Terzan 5 system, is described in detail in Section 3.2 and Section 3.2.2. The different simulations aim to investigate the effects of varying two key parameters:

- the initial mass of the FG stars, set to either $10^6 M_{\odot}$ (M6 model) or $10^7 M_{\odot}$ (M7 model);
- the velocity of the infalling GMC, set to either $v = 10 \text{ km s}^{-1}$ (labelled v10) or $v = 20 \text{ km s}^{-1}$ (labelled v20).

Additionally, in the simulations I have implemented a star formation model able to form individual stars (see Section 3.1.1), a star-by-star feedback model (see Section 3.1.3) and a cooling model (see Section 3.1.4).

In Chapter 4 I provide a detailed analysis of the models with a maximum level of refinement 8:

- Specifically, M6-v10-L8 (in Section 4.1.1) and M6-v20-L8 (in Section 4.1.2). In both cases I observed the formation of stars more massive than $8 M_{\odot}$, which are able to produce pre-SN feedback. Consequently, the gas in their surrounding region is heated, effectively halting further star formation. The total mass of SG stars is of the order of $\simeq 10^3 M_{\odot}$;
- M7-v10-L8 (in Section 4.2.1) and M7-v20-L8 (in Section 4.2.2). In these cases, I did not observe the formation of stars more massive than $8 M_{\odot}$. However, despite the absence pre-SN feedback able to halt the star formation process, the total mass of SG formed is on the order of few $10^3 M_{\odot}$;

at the end of the Chapter some space is given to the L7 models, as convergence tests.

5.2 Conclusions

The main result of this work is that, regardless of the initial mass of the FG and the velocity infall of the GMC, the mass of the SG formed from the accretion of the

GMC always remains orders of magnitude below the observed value in Terzan 5. The results from the different simulations revealed that in the M6 models star formation is halted as soon as the system forms stars with masses greater than $8 M_{\odot}$, which are able, via the implemented pre-SN feedback model, to halt the star formation. In the M7 simulations, star formation continues, indicating that the different initial conditions of the FG star system significantly impact the simulation's evolution, however without producing a sufficient total SG mass to reproduce the observed one in Terzan 5.

The total mass of SG produced in the simulations is, at most, $1.78 \times 10^3 M_{\odot}$, for the models with an initial FG stars mass of $10^6 M_{\odot}$, and $1.58 \times 10^3 M_{\odot}$ in those cases where the initial FG stars mass is $10^7 M_{\odot}$, while the mass of SG observed in Terzan 5 is $8 \times 10^5 M_{\odot}$. This result is at odds with the findings of McKenzie & Bekki (2018) and it is attributed to the inclusion of pre-SN feedback from massive stars in the simulations, which has been found to play a crucial role in halting star formation.

Thus, the major conclusion of this work is that, once a more realistic description of the stellar feedback is incorporated hypothesis (4) (see Section 1.4) - i.e., that the Terzan 5 SG is the result of the accretion of a GMC - appears to be a much less viable possibility than previously thought.

5.3 Future perspectives

Future works could further expand the results of this thesis, focusing on refining the models presented here to gain a deeper understanding of the formation of BFFs. Below, I list a series of possible future improvements.

One of the improvement is the use of a more advanced star formation model, specifically the so-called *sink particles model*, first introduced by Bate et al. (1995) and further described in Bleuler & Teyssier (2014) and Sormani et al. (2017). This model offers the possibility to improve the stochastic sampling from the stellar initial mass function, as described in Section 3.1.1. In the sink particle approach, a contracting high-density region is replaced by a single Lagrangian particle once the numerical resolution limit in the simulation is reached. The particle inherits the mass, as well as the linear and angular momentum of the original region and, in many implementations, it can also accrete mass infalling at later times. If the resolution is high enough, each sink particle can represent a single star.

Another improvement could involve modifying the initial physical conditions with

respect to the set-up implemented here (described in Section 3.3.2), specifically by changing the GMC distribution in favor of a more realistic spatial distribution (as proposed in Section 3.2). In reality, GMCs exhibit a complex structure, unlike the homogeneous distribution assumed in this thesis. Moreover, a higher ISM density or different infalling velocities compared to the conditions explored in the previous chapters could significantly influence the cluster's ability to accumulate mass (Naiman et al., 2011).

As anticipated in Section 3.1.2 other possible improvements can be done exploring the effects of different ε_{ff} values, fixed to 1 in this thesis work, considering its relationship with resolution and its role in a more realistic modeling of star formation. Furthermore, additional improvements could be made to the feedback model. At the moment pre-SN feedback is included; however, the model could be refined considering the inclusion of feedback from ionizing radiation (see Yaghoobi et al., 2022a), which is currently not accounted for in the simulations.

Bibliography

- Adamo A., et al., 2024, Bound star clusters observed in a lensed galaxy 460 Myr after the Big Bang ([arXiv:2401.03224](https://arxiv.org/abs/2401.03224)), <https://arxiv.org/abs/2401.03224>
- Agertz O., Kravtsov A. V., 2015, *AJ*, 804, 18
- Agertz O., Kravtsov A. V., Leitner S. N., Gnedin N. Y., 2013, *AJ*, 770, 25
- Agertz O., et al., 2020, *MNRAS*, 491, 1656
- Alvarez Garay D. A., Mucciarelli A., Lardo C., Bellazzini M., Merle T., 2022, *ApJL*, 928, L11
- Alvarez Garay D., et al., 2024, X-shooter spectroscopy of Liller1 giant stars ([arXiv:2404.14130](https://arxiv.org/abs/2404.14130)), <https://arxiv.org/abs/2404.14130>
- Andersson E. P., Agertz O., Renaud F., 2020, *MNRAS*, 494, 3328
- André P., et al., 2010, *A&A*, 518, L102
- Asplund M., Grevesse N., Sauval A. J., Scott P., 2009, *A&A Rev.*, 47, 481
- Asplund M., Amarsi A. M., Grevesse N., 2021, *A&A*, 653, A141
- Baade W., 1946, *PASP*, 58, 249
- Bagla J. S., 2002, *Journal of Astrophysics and Astronomy*, 23, 185–196
- Balsara D. S., 2004, *AJSupplement Series*, 151, 149–184
- Barbuy B., Chiappini C., Gerhard O., 2018, *A&A Rev.*, 56, 223–276
- Barnes J., Hut P., 1986, *Nature*, 324, 446
- Bastian N., Lardo C., 2018, *A&A Rev.*, 56, 83

- Bastian N., Pfeffer J., 2021, *MNRAS*, 509, 614
- Bastian N., Lamers H. J. G. L. M., de Mink S. E., Longmore S. N., Goodwin S. P., Gieles M., 2013a, *MNRAS*, 436, 2398
- Bastian N., Cabrera-Ziri I., Davies B., Larsen S. S., 2013b, *MNRAS*, 436, 2852
- Bastian N., Cabrera-Ziri I., Salaris M., 2015, *MNRAS*, 449, 3333–3346
- Bate M. R., Bonnell I. A., Price N. M., 1995, *MNRAS*, 277, 362–376
- Baumgardt H., Makino J., 2003, *MNRAS*, 340, 227
- Baumgardt H., Vasiliev E., 2021, *MNRAS*, 505, 5957–5977
- Baumgardt H., Hilker M., Sollima A., Bellini A., 2018, *MNRAS*, 482, 5138–5155
- Baumgardt H., Hilker M., Sollima A., Bellini A., 2019, *MNRAS*, 482, 5138
- Baumgardt H., Sollima A., Hilker M., 2020, *Publications of the Astronomical Society of Australia*, 37
- Baumgardt H., Hénault-Brunet V., Dickson N., Sollima A., 2023, *MNRAS*, 521, 3991–4008
- Behrendt M., Burkert A., Schartmann M., 2016, *ApJL*, 819, L2
- Bekki K., 2017, *MNRAS*, 469, 2933
- Bekki K., Freeman K. C., 2003, *MNRAS*, 346, L11
- Bellini A., Milone A. P., Anderson J., Marino A. F., Piotto G., van der Marel R. P., Bedin L. R., King I. R., 2017, *ApJ*, 844, 164
- Bensby T., et al., 2013, *A&A*, 549, A147
- Berger M., Colella P., 1989, *JCP*, 82, 64
- Berger M. J., Olinger J., 1984, *JCP*, 53, 484
- Binney J., Tremaine S., 2008, *Galactic Dynamics: Second Edition*. Princeton series in astrophysics
- Bleuler A., Teyssier R., 2014, *MNRAS*, 445, 4015–4036
- Bondi H., Hoyle F., 1944, *MNRAS*, 104, 273

- Bournaud F., 2016, in Laurikainen E., Peletier R., Gadotti D., eds, *Astrophysics and Space Science Library* Vol. 418, Galactic Bulges. p. 355 ([arXiv:1503.07660](#)), [doi:10.1007/978-3-319-19378-6_13](#)
- Bournaud F., Elmegreen B. G., 2009, *ApJL*, 694, L158
- Bouwens R. J., Illingworth G. D., van Dokkum P. G., Ribeiro B., Oesch P. A., Stefanon M., 2021, *AJ*, 162, 255
- Breen P. G., 2018, *MNRAS*, 481, L110
- Bromm V., Larson R. B., 2004, *A&A Rev.*, 42, 79
- Brown G., Gnedin O. Y., 2021, *MNRAS*, 508, 5935–5953
- Brown G., Gnedin O. Y., Li H., 2018, *ApJ*, 864, 94
- Bryan G. L., et al., 2014, *ApJS*, 211, 19
- Caimmi R., 2015, *Applied Mathematical Sciences*, 9, 1311–1329
- Calura F., Few C. G., Romano D., D’Ercole A., 2015, *AJ*, 814, L14
- Calura F., D’Ercole A., Vesperini E., Vanzella E., Sollima A., 2019, *MNRAS*, 489, 3269
- Calura F., et al., 2021, *MNRAS*, 500, 3083
- Calura F., et al., 2022, *MNRAS*, 516, 5914
- Calura F., et al., 2024, *arXiv e-prints*, p. [arXiv:2411.02502](#)
- Carollo C. M., Scarlata C., Stiavelli M., Wyse R. F. G., Mayer L., 2007, *ApJ*, 658, 960
- Carretta E., 2015, *ApJ*, 810, 148
- Carretta E., et al., 2009a, *A&A*, 505, 117
- Carretta E., Bragaglia A., Gratton R., Lucatello S., 2009b, *A&A*, 505, 139
- Carretta E., Bragaglia A., Gratton R., D’Orazi V., Lucatello S., 2009c, *A&A*, 508, 695

- Carretta E., Bragaglia A., Lucatello S., Gratton R. G., D’Orazi V., Sollima A., 2018, [A&A](#), **615**, A17
- Castor J., McCray R., Weaver R., 1975, [ApJL](#), **200**, L107
- Cava A., Schaerer D., Richard J., Pérez-González P. G., Dessauges-Zavadsky M., Mayer L., Tamburello V., 2017, [Nature Astronomy](#), **2**, 76–82
- Chevance M., et al., 2022, [MNRAS](#), **509**, 272
- Chon S., Omukai K., Schneider R., 2021, [MNRAS](#)
- Cignoni M., et al., 2015, [ApJ](#), **811**, 76
- Clark P. C., Glover S. C. O., Klessen R. S., Bromm V., 2011, [ApJ](#), **727**, 110
- Clarke C., Carswell B., 2014, *Principles of Astrophysical Fluid Dynamics*. Cambridge University Press
- Colella P., 1990, [JCP](#), **87**, 171
- Colella P., Glaz H. M., 1985, [JCP](#), **59**, 264
- Combes F., Debbasch F., Friedli D., Pfenniger D., 1990, [A&A](#), **233**, 82
- Cottrell P. L., Da Costa G. S., 1981, [ApJL](#), **245**, L79
- Couchman H. M. P., 1991, [ApJL](#), **368**, L23
- Courant R., Friedrichs K., Lewy H., 1967, [IBM Journal of Research and Development](#), **11**, 215
- Cox D. P., 2005, [A&A Rev.](#), **43**, 337
- Crociati C., et al., 2023, [ApJ](#), **951**, 17
- Crociati C., et al., 2024, [A&A](#), **691**, A311
- Cummings J. D., Kalirai J. S., Tremblay P. E., Ramirez-Ruiz E., Choi J., 2018, [ApJ](#), **866**, 21
- D’Antona F., Caloi V., D’Ercole A., Tailo M., Vesperini E., Ventura P., Di Criscienzo M., 2013, [MNRAS](#), **434**, 1138

- D'Antona F., Vesperini E., D'Ercole A., Ventura P., Milone A. P., Marino A. F., Tailo M., 2016, *MNRAS*, 458, 2122
- D'Antona F., Ventura P., Fabiola Marino A., Milone A. P., Tailo M., Di Criscienzo M., Vesperini E., 2019, *ApJL*, 871, L19
- D'Ercole A., Vesperini E., D'Antona F., McMillan S. L. W., Recchi S., 2008, *MNRAS*, 391, 825
- D'Ercole A., D'Antona F., Ventura P., Vesperini E., McMillan S. L. W., 2010, *MNRAS*, 407, 854
- D'Ercole A., D'Antona F., Vesperini E., 2011, *MNRAS*, 415, 1304
- D'Ercole A., D'Antona F., Vesperini E., 2016, *MNRAS*, 461, 4088
- Dai W., Woodward P. R., 1994, *JCP*, 115, 485
- Dalessandro E., Lapenna E., Mucciarelli A., Origlia L., Ferraro F. R., Lanzoni B., 2016, *ApJ*, 829, 77
- Dalessandro E., et al., 2022, *AJ*, 940, 170
- Decressin T., Charbonnel C., Meynet G., 2007, *A&A*, 475, 859
- Dekel A., Tziperman O., Sarkar K. C., Ginzburg O., Mandelker N., Ceverino D., Primack J., 2023, *MNRAS*, 521, 4299–4322
- Deng Y., Li H., Liu B., Kannan R., Smith A., Bryan G. L., 2024, *A&A*, 691, A231
- Denissenkov P. A., Hartwick F. D. A., 2014, *MNRAS*, 437, L21
- Denissenkov P. A., Herwig F., 2003, *AJ*, 590, L99–L102
- Dessauges-Zavadsky M., et al., 2023, *MNRAS*, 519, 6222
- Dubois Y., Volonteri M., Silk J., Devriendt J., Slyz A., Teyssier R., 2015, *MNRAS*, 452, 1502
- D'Ercole A., D'Antona F., Ventura P., Vesperini E., McMillan S. L. W., 2010, *MNRAS*, 407, 854–869
- D'Ercole A., D'Antona F., Vesperini E., 2011, *MNRAS*, 415, 1304–1309

- D’Ercole A., D’Antona F., Carini R., Vesperini E., Ventura P., 2012, *MNRAS*, 423, 1521
- Efstathiou G., Eastwood J. W., 1981, *MNRAS*, 194, 503
- Eggen O. J., Lynden-Bell D., Sandage A. R., 1962, *ApJ*, 136, 748
- Elmegreen B. G., 2017, *ApJ*, 836, 80
- Elmegreen B. G., Bournaud F., Elmegreen D. M., 2008, *AJ*, 688, 67–77
- Elmegreen D. M., Elmegreen B. G., Marcus M. T., Shahinyan K., Yau A., Petersen M., 2009, *AJ*, 701, 306–329
- Emerick A., Bryan G. L., Mac Low M.-M., 2018, *MNRAS*, 482, 1304–1329
- Evans II N. J., Heiderman A., Vutisalchavakul N., 2014, *ApJ*, 782, 114
- Falgarone E., Phillips T. G., Walker C. K., 1991, *ApJ*, 378, 186
- Fanelli C., et al., 2024, Multi-iron subpopulations in Liller 1 from high resolution H-band spectroscopy ([arXiv:2408.12649](https://arxiv.org/abs/2408.12649)), <https://arxiv.org/abs/2408.12649>
- Farcy M., Rosdahl J., Dubois Y., Blaizot J., Martin-Alvarez S., 2022, *MNRAS*, 513, 5000
- Federrath C., Klessen R. S., 2012, *ApJ*, 761, 156
- Ferrara A., Salvaterra R., 2004, Feedback Processes at Cosmic Dawn ([arXiv:astro-ph/0406554](https://arxiv.org/abs/astro-ph/0406554)), <https://arxiv.org/abs/astro-ph/0406554>
- Ferraro F. R., Sollima A., Pancino E., Bellazzini M., Straniero O., Origlia L., Cool A. M., 2004, *AJ*, 603, L81–L84
- Ferraro F. R., et al., 2009, *Nature*, 462, 483
- Ferraro F. R., Massari D., Dalessandro E., Lanzoni B., Origlia L., Rich R. M., Mucciarelli A., 2016, *ApJ*, 828, 75
- Ferraro F. R., et al., 2021, *Nature Astronomy*, 5, 311
- Field G. B., Goldsmith D. W., Habing H. J., 1969, *ApJL*, 155, L149
- Fierlinger K. M., Burkert A., Ntormousi E., Fierlinger P., Schartmann M., Ballone A., Krause M. G. H., Diehl R., 2016, *MNRAS*, 456, 710

- Fisher D. B., Bolatto A. D., Glazebrook K., Obreschkow D., Abraham R. G., Kacprzak G. G., Nielsen N. M., 2022, *ApJ*, **928**, 169
- Fryxell B., et al., 2000, *ApJS*, **131**, 273
- Garcia F. A. B., Ricotti M., Sugimura K., Park J., 2023, *MNRAS*, **522**, 2495–2515
- Gatto M., et al., 2020, *MNRAS*, **499**, 4114–4139
- Geen S., Hennebelle P., Tremblin P., Rosdahl J., 2016, *MNRAS*, **463**, 3129
- Genzel R., et al., 2011, *ApJ*, **733**, 101
- Gieles M., et al., 2018, *MNRAS*, **478**, 2461
- Gingold R. A., Monaghan J. J., 1977, *MNRAS*, **181**, 375
- Glover S., 2005, *Space Science Reviews*, **117**, 445
- Godunov S. K., Bohachevsky I., 1959, *Matematičeskij sbornik*, **47(89)**, 271
- Gonzalez O. A., Rejkuba M., Zoccali M., Valent E., Minniti D., Tobar R., 2013, *A&A*, **552**, A110
- Gratton R., Sneden C., Carretta E., 2004, *A&A Rev.*, **42**, 385
- Gratton R. G., Carretta E., Bragaglia A., 2012, *A&A Rev.*, **20**, 50
- Gratton R., Bragaglia A., Carretta E., D’Orazi V., Lucatello S., Sollima A., 2019, *A&A Rev.*, **27**, 8
- Grisdale K., Agertz O., Renaud F., Romeo A. B., Devriendt J., Slyz A., 2019, *MNRAS*, **486**, 5482
- Grudic M., Hopkins P., Lee E., Murray N., Faucher-Giguère C., Johnson L., 2019, *MNRAS*, **488**, 1501
- Guo Y., et al., 2015, *ApJ*, **800**, 39
- Gutcke T. A., Pakmor R., Naab T., Springel V., 2021, *MNRAS*
- Haffner L. M., et al., 2009, *Reviews of Modern Physics*, **81**, 969–997
- Harris W. E., 2010, A New Catalog of Globular Clusters in the Milky Way ([arXiv:1012.3224](https://arxiv.org/abs/1012.3224)), <https://arxiv.org/abs/1012.3224>

- Harten A., Lax P. D., Leer B. V., 1983, *SIAM Review*, 25, 35
- Hasselquist S., et al., 2020, *AJ*, 901, 109
- Haywood M., Di Matteo P., Lehnert M., Snaith O., Fragkoudi F., Khoperskov S., 2018, *A&A*, 618, A78
- Heckman T. M., Robert C., Leitherer C., Garnett D. R., van der Rydt F., 1998, *AJ*, 503, 646–661
- Helmi A., Babusiaux C., Koppelman H. H., Massari D., Veljanoski J., Brown A. G. A., 2018, *Nature*, 563, 85–88
- Herwig F., 2004, *AJ*, 605, 425–435
- Hilker M., Baumgardt H., Sollima A., Bellini A., 2019, *Proceedings of the International Astronomical Union*, 14, 451–454
- Hirai Y., Fujii M. S., Saitoh T. R., 2021, *PASJ*, 73, 1036
- Hirano S., Bromm V., 2017, *MNRAS*, 470, 898–914
- Hockney R. W., Eastwood J. W., 1981, *Computer Simulation Using Particles*. CRC Press
- Hockney R. W., Goel S. P., Eastwood J. W., 1974, *JCP*, 14, 148
- Hopkins P. F., 2015, *MNRAS*, 450, 53–110
- Hopkins A. M., 2018, *PASA*, 35, e039
- Hopkins P. F., et al., 2010, *ApJ*, 715, 202
- Hopkins P. F., Kereš D., Murray N., Quataert E., Hernquist L., 2012, *MNRAS*, 427, 968
- Horta D., et al., 2020, *MNRAS*, 500, 1385–1403
- Hu C.-Y., et al., 2023, *AJ*, 950, 132
- Immeli A., Samland M., Gerhard O., Westera P., 2003, *A&A*, 413, 547–561
- Janhunen P., 2000, *JCP*, 160, 649
- Jeon M., Besla G., Bromm V., 2017, *ApJ*, 848, 85

- Jessop C. M., Duncan M. J., Chau W. Y., 1994, *JCP*, 115, 339
- Johnson C. I., Pilachowski C. A., 2010, *ApJ*, 722, 1373
- Johnson C. I., Rich R. M., Kobayashi C., Kunder A., Koch A., 2014, *AJ*, 148, 67
- Kapse S., de Grijs R., Kamath D., Zucker D. B., 2022, *ApJL*, 927, L10
- Karakas A., Lattanzio J. C., 2007, *Publications of the Astronomical Society of Australia*, 24, 103–117
- Katz N., 1992, *ApJ*, 391, 502
- Kennicutt R. C., Evans N. J., 2012, *A&A Rev.*, 50, 531
- Khokhlov A., 1998, *JCP*, 143, 519–543
- Kim C.-G., Ostriker E. C., 2015, *ApJ*, 802, 99
- Kim J.-h., et al., 2014, *ApJS*, 210, 14
- Kim J.-h., et al., 2016, *ApJ*, 833, 202
- Kimm T., Cen R., Rosdahl J., Yi S. K., 2016, *ApJ*, 823, 52
- King I. R., 1966, *AJ*, 71, 64
- Kirch G., 1682, *Gottfridi Kirchii Annus ... Ephemeridum Motuum Coelestium Ad Annum Aerae Christianae ... : Cum ortu and occasu diurno Planetarum, Occultationibusq[ue] tam Planetarum, quam illustriorum Stellarum Fixarum c. Ex Tabulis Rudolphinis, Ad Meridianum Uranoburgicum, In Freto Cimbrico Supputatus*, <http://dx.doi.org/10.25673/opendata2-32735>
- Klessen R. S., Glover S. C. O., 2023, *A&A Rev.*, 61, 65
- Klypin A. A., Shandarin S. F., 1983, *MNRAS*, 204, 891
- Krause M., Charbonnel C., Decressin T., Meynet G., Prantzos N., 2013, *A&A*, 552, A121
- Kravtsov A. V., Klypin A. A., Khokhlov A. M., 1997, *AJSupplement Series*, 111, 73–94
- Kroupa P., 2001, *MNRAS*, 322, 231

- Kruijssen J. M. D., et al., 2019, *Nature*, 569, 519–522
- Lacchin E., Calura F., Vesperini E., 2021, *MNRAS*, 506, 5951
- Lada C. J., Lada E. A., 2003, *A&A Rev.*, 41, 57
- Lahén N., Naab T., Johansson P. H., Elmegreen B., Hu C.-Y., Walch S., Steinwandel U. P., Moster B. P., 2020, *ApJ*, 891, 2
- Lahén N., et al., 2023, *MNRAS*, 522, 3092
- Lanzoni B., et al., 2010, *ApJ*, 717, 653
- Larsen S. S., Brodie J. P., Grundahl F., Strader J., 2014, *AJ*, 797, 15
- Larson R. B., 1998, *MNRAS*, 301, 569
- Laurikainen E., Peletier R., Gadotti D., eds, 2016, Galactic Bulges. Astrophysics and Space Science Library, Springer, doi:10.1007/978-3-319-19378-6
- Laurmaa V., Picasso M., Steiner G., 2016, *Computers & Fluids*, 131, 190
- Lee E. J., Miville-Deschênes M.-A., Murray N. W., 2016, *ApJ*, 833, 229
- Legnardi M. V., et al., 2022, *MNRAS*, 513, 735–751
- Li H., Gnedin O. Y., Gnedin N. Y., 2018, *ApJ*, 861, 107
- Lucy L. B., 1977, *AJ*, 82, 1013
- Ma X., et al., 2020, *MNRAS*, 493, 4315–4332
- Mackey J., 2023, in Vidotto A. A., Fossati L., Vink J. S., eds, IAU Symposium Vol. 370, Winds of Stars and Exoplanets. pp 205–216 (arXiv:2211.08808), doi:10.1017/S1743921322004501
- Mannucci F., et al., 2009, *MNRAS*, 398, 1915–1931
- Maraston C., 1998, *MNRAS*, 300, 872–892
- Marino A. F., et al., 2021, Solving the globular clusters multiple population enigma through JWST, JWST Proposal. Cycle 1, ID. #2560
- Marks M., Kroupa P., 2010, *MNRAS*, pp no–no
- Martocchia S., et al., 2018, *MNRAS*, 473, 2688

- Massari D., et al., 2012, *ApJL*, 755, L32
- Massari D., et al., 2014, *ApJ*, 795, 22
- Massari D., et al., 2015, *ApJ*, 810, 69
- Massari D., Breddels M. A., Helmi A., Posti L., Brown A. G. A., Tolstoy E., 2017, *Nature Astronomy*, 2, 156–161
- Massari D., Breddels M. A., Helmi A., Posti L., Brown A. G. A., Tolstoy E., 2018, *Nature Astronomy*, 2, 156
- Matteucci F., Brocato E., 1990, *ApJ*, 365, 539
- McKee C. F., Ostriker J. P., 1977, *ApJ*, 218, 148
- McKenzie M., Bekki K., 2018, *MNRAS*, 479, 3126
- Menon H., Wesolowski L., Zheng G., Jetley P., Kale L., Quinn T., Governato F., 2014, Adaptive Techniques for Clustered N-Body Cosmological Simulations ([arXiv:1409.1929](https://arxiv.org/abs/1409.1929)), <https://arxiv.org/abs/1409.1929>
- Men'shchikov A., et al., 2010, *Astronomy and Astrophysics*, 518, L103
- Messa M., Dessauges-Zavadsky M., Richard J., Adamo A., Nagy D., Combes F., Mayer L., Ebeling H., 2022, *MNRAS*, 516, 2420–2443
- Messa M., et al., 2025, *A&A*, 694, A59
- Mignone A., Bodo G., Massaglia S., Matsakos T., Tesileanu O., Zanni C., Ferrari A., 2007, *ApJS*, 170, 228
- Milone A. P., Marino A. F., 2022, Multiple Populations in Star Clusters ([arXiv:2206.10564](https://arxiv.org/abs/2206.10564)), <https://arxiv.org/abs/2206.10564>
- Milone A. P., et al., 2019, *MNRAS*, 484, 4046–4053
- Minniti D., Fernández-Trincado J. G., Ripepi V., Alonso-García J., Ramos R. C., Marconi M., 2018, *ApJL*, 869, L10
- Molinari S., et al., 2010, *A&A*, 518, L100
- Mucciarelli A., Origlia L., Ferraro F. R., Pancino E., 2009, *ApJL*, 695, L134
- Murray N., 2011, *ApJ*, 729, 133

- Myers P. C., Dame T. M., Thaddeus P., Cohen R. S., Silverberg R. F., Dwek E., Hauser M. G., 1986, *ApJ*, **301**, 398
- Mészáros S., et al., 2021, *MNRAS*, **505**, 1645–1660
- Naiman J. P., Ramirez-Ruiz E., Lin D. N. C., 2011, *ApJ*, **735**, 25
- Nardiello D., Piotto G., Milone A. P., Rich R. M., Cassisi S., Bedin L. R., Bellini A., Renzini A., 2019, *MNRAS*, **485**, 3076
- Nataf D. M., 2017, *Publications of the Astronomical Society of Australia*, **34**, e041
- Ness M., et al., 2013a, *MNRAS*, **430**, 836
- Ness M., et al., 2013b, *MNRAS*, **430**, 836
- Niederhofer F., et al., 2017, *MNRAS*, **465**, 4159
- Nogueras-Lara F., et al., 2020, *Nature Astronomy*, **4**, 377
- Norris J. E., Freeman K. C., Mighell K. J., 1996, *ApJ*, **462**, 241
- Origlia L., 2014, in Feltzing S., Zhao G., Walton N. A., Whitelock P., eds, *IAU Symposium Vol. 298, Setting the scene for Gaia and LAMOST*. pp 28–39, doi:10.1017/S1743921313006170
- Origlia L., Ferraro F. R., Bellazzini M., Pancino E., 2003, *AJ*, **591**, 916–924
- Origlia L., et al., 2011, *ApJL*, **726**, L20
- Origlia L., Massari D., Rich R. M., Mucciarelli A., Ferraro F. R., Dalessandro E., Lanzoni B., 2013, *ApJL*, **779**, L5
- Origlia L., et al., 2019, *ApJ*, **871**, 114
- Oswalt T. D., Gilmore G., 2013, *Planets, Stars and Stellar Systems: Volume 5: Galactic Structure and Stellar Populations*. Springer, doi:10.1007/978-94-007-5612-0
- Pancino E., Ferraro F. R., Bellazzini M., Piotto G., Zoccali M., 2000, *AJ*, **534**, L83
- Pascale R., et al., 2023, *Shaping the unseen: the influence of baryons and environment on low-mass, high-redshift dark matter haloes in the SIEGE simulations* (arXiv:2309.01742), <https://arxiv.org/abs/2309.01742>

- Petty S. M., de Mello D. F., Gallagher III J. S., Gardner J. P., Lotz J. M., Mountain C. M., Smith L. J., 2009, *AJ*, **138**, 362
- Pfeffer J., Lardo C., Bastian N., Saracino S., Kamann S., 2020, *MNRAS*, **500**, 2514–2524
- Piotto G., et al., 2015, *AJ*, **149**, 91
- Plummer H. C., 1911, *MNRAS*, **71**, 460
- Portail M., Gerhard O., Wegg C., Ness M., 2017, *MNRAS*, **465**, 1621
- Portinari L., Chiosi C., Bressan A., 1998, *A&A*, **334**, 505
- Power C., Navarro J. F., Jenkins A., Frenk C. S., White S. D. M., Springel V., Stadel J., Quinn T., 2003, *MNRAS*, **338**, 14
- Press W. H., Teukolsky S. A., Vetterling W. T., Flannery B. P., 1992, *Numerical recipes in FORTRAN. The art of scientific computing*. Cambridge
- Price D. J., et al., 2018, *PASA*, **35**, e031
- Queiroz A. B. A., et al., 2021, *A&A*, **656**, A156
- Rasera Y., Teyssier R., 2006, *A&A*, **445**, 1
- Renaud F., 2020, in Bragaglia A., Davies M., Sills A., Vesperini E., eds, *IAU Symposium Vol. 351, Star Clusters: From the Milky Way to the Early Universe*. pp 40–46 ([arXiv:1908.02301](https://arxiv.org/abs/1908.02301)), [doi:10.1017/S1743921319007312](https://doi.org/10.1017/S1743921319007312)
- Renaud F., et al., 2013, *MNRAS*, **436**, 1836
- Renaud F., Agertz O., Gieles M., 2017, *MNRAS*, **465**, 3622
- Renzini A., Buzzoni A., 1986, in Chiosi C., Renzini A., eds, *Astrophysics and Space Science Library Vol. 122, Spectral Evolution of Galaxies*. pp 195–231, [doi:10.1007/978-94-009-4598-2_19](https://doi.org/10.1007/978-94-009-4598-2_19)
- Renzini A., et al., 2015, *MNRAS*, **454**, 4197
- Renzini A., et al., 2018, *AJ*, **863**, 16
- Revaz Y., Jablonka P., 2012, *A&A*, **538**, A82
- Revaz Y., Arnaudon A., Nichols M., Bonvin V., Jablonka P., 2016, *A&A*, **588**, A21

- Rich R. M., 1998, in Sofue Y., ed., IAU Symposium Vol. 184, The Central Regions of the Galaxy and Galaxies. p. 11
- Rich R. M., et al., 2020, *MNRAS*, 499, 2340–2356
- Rodríguez M. J., Baume G., Feinstein C., 2020, *A&A*, 644, A101
- Roe P. L., 1986, *Annual Review of Fluid Dynamics*, 18, 337
- Romano D., Matteucci F., Tosi M., Pancino E., Bellazzini M., Ferraro F. R., Limongi M., Sollima A., 2007, *MNRAS*, 376, 405
- Romano D., et al., 2023, *ApJ*, 951, 85
- Rosdahl K. J., 2012, Theses, Université Claude Bernard - Lyon I, <https://theses.hal.science/tel-01127475>
- Rosdahl J., Teyssier R., 2015, *MNRAS*, 449, 4380
- Rosdahl J., Schaye J., Dubois Y., Kimm T., Teyssier R., 2017, *MNRAS*, 466, 11
- Rosen A. L., Lopez L. A., Krumholz M. R., Ramirez-Ruiz E., 2014, *MNRAS*, 442, 2701
- Ruiz-Lara T., Gallart C., Bernard E. J., Cassisi S., 2020, *Nature Astronomy*, 4, 965
- Ryu D., Jones T. W., 1995, *ApJ*, 442, 228
- Safraneck-Shrader C., Milosavljević M., Bromm V., 2014, *MNRAS*, 438, 1669–1685
- Saha A., et al., 2019, *Astrophysical Journal*, 874
- Salpeter E. E., 1955, *ApJ*, 121, 161
- Saltzman J., 1994, *JCP*, 115, 153
- Scalo J., 1990, in Capuzzo-Dolcetta R., Chiosi C., di Fazio A., eds, Physical Processes in Fragmentation and Star Formation. Springer Netherlands, Dordrecht, pp 151–177
- Scannapieco C., Tissera P. B., 2003, *MNRAS*, 338, 880–890
- Schmidt M., 1959, *ApJ*, 129, 243

- Senchyna P., Plat A., Stark D. P., Rudie G. C., 2023, GN-z11 in context: possible signatures of globular cluster precursors at redshift 10 ([arXiv:2303.04179](https://arxiv.org/abs/2303.04179)), <https://arxiv.org/abs/2303.04179>
- Shibuya T., Ouchi M., Kubo M., Harikane Y., 2016, *AJ*, 821, 72
- Shu F. H., Adams F. C., Lizano S., 1987, *A&A Rev.*, 25, 23
- Silverman J. D., et al., 2015, *ApJL*, 812, L23
- Sollima A., 2021, *MNRAS*, 502, 1974–1989
- Solomon P. M., Rivolo A. R., Barrett J., Yahil A., 1987, *ApJ*, 319, 730
- Sormani M. C., Treß R. G., Klessen R. S., Glover S. C. O., 2017, *MNRAS*, 466, 407
- Springel V., 2010, *MNRAS*, 401, 791
- Springel V., 2014, High performance computing and numerical modelling ([arXiv:1412.5187](https://arxiv.org/abs/1412.5187)), <https://arxiv.org/abs/1412.5187>
- Springel V., Yoshida N., White S. D., 2001, *New Astronomy*, 6, 79–117
- Stone J. M., Norman M. L., 1992, *ApJS*, 80, 753
- Stone J. M., Gardiner T. A., Teuben P., Hawley J. F., Simon J. B., 2008, *AJSupplement Series*, 178, 137–177
- Stone J. M., Tomida K., White C. J., Felker K. G., 2020, *AJSupplement Series*, 249, 4
- Stutzki J., Bensch F., Heithausen A., Ossenkopf V., Zielinsky M., 1998, *A&A*, 336, 697
- Teyssier R., 2002, *A&A*, 385, 337
- Teyssier R., Pontzen A., Dubois Y., Read J. I., 2013, *MNRAS*, 429, 3068
- Thacker R. J., Couchman H. M. P., 2000, *AJ*, 545, 728–752
- Tielens A. G. G. M., 2005, *The Physics and Chemistry of the Interstellar Medium*. Cambridge
- Toomre A., Toomre J., 1972, *ApJ*, 178, 623

- Toro E., 1977, *Riemann Solvers and Numerical Methods for Fluid Dynamics*. Springer, [doi:10.1007/b79761](https://doi.org/10.1007/b79761).
- Toro E. F., Spruce M., Speares W., 1994, *Shock Waves*, 4, 25
- Tosi M., Greggio L., Marconi G., Focardi P., 1991, *AJ*, 102, 951
- Tress R. G., Sormani M. C., Glover S. C. O., Klessen R. S., Battersby C. D., Clark P. C., Hatchfield H. P., Smith R. J., 2020, *MNRAS*, 499, 4455
- Truelove J. K., Klein R. I., McKee C. F., Holliman II J. H., Howell L. H., Greenough J. A., 1997, *ApJL*, 489, L179
- Utomo D., et al., 2018, *ApJL*, 861, L18
- Valenti E., Ferraro F. R., Origlia L., 2007, *The Astronomical Journal*, 133, 1287–1301
- Valenti E., Zoccali M., Renzini A., Brown T. M., Gonzalez O. A., Minniti D., Debattista V. P., Mayer L., 2013, *A&A*, 559, A98
- Valenti E., et al., 2016, *A&A*, 587, L6
- VandenBerg D. A., Stetson P. B., Brown T. M., 2015, *AJ*, 805, 103
- Vanzella E., et al., 2017, *AJ*, 842, 47
- Vanzella E., et al., 2019, *MNRAS*, 483, 3618
- Vanzella E., et al., 2021, *A&A*, 646, A57
- Vanzella E., et al., 2022, *ApJL*, 940, L53
- Ventura P., D’Antona F., 2011, *MNRAS*, 410, 2760
- Ventura P., D’Antona F., 2008, *A&A*, 479, 805–816
- Vesperini E., Heggie D. C., 1997, *MNRAS*, 289, 898–920
- Vink J. S., 2018, *A&A*, 619, A54
- Wadsley J., Stadel J., Quinn T., 2004, *New Astronomy*, 9, 137
- Walker A. R., 1999, *AJ*, 118, 432

- Wall J. E., Low M.-M. M., McMillan S. L. W., Klessen R. S., Zwart S. P., Pellegrino A., 2020, *AJ*, 904, 192
- Wang L., Kroupa P., Takahashi K., Jerabkova T., 2020, *MNRAS*, 491, 440
- Wang S., Chen B., Ma J., 2021, *A&A*, 645, A115
- Weaver R., McCray R., Castor J., Shapiro P., Moore R., 1977, *ApJ*, 218, 377
- Wegg C., Gerhard O., Portail M., 2015, *MNRAS*, 450, 4050
- Woosley S. E., Weaver T. A., 1995, *ApJS*, 101, 181
- Yaghoobi A., Calura F., Rosdahl J., Haghi H., 2022a, *MNRAS*, 510, 4330
- Yaghoobi A., Rosdahl J., Calura F., Khalaj P., Haghi H., 2022b, *MNRAS*, 517
- Yaghoobi A., Rosdahl J., Calura F., Ataiee S., 2024, *MNRAS*, 528, 5477
- Zachary A. L., Colella P., 1992, *JCP*, 99, 341
- Zanella A., et al., 2015, *Nature*, 521, 54
- Zanella A., et al., 2019, *MNRAS*, 489, 2792–2818
- Ziegler U., 2004, *JCP*, 196, 393
- Ziegler U., 2005, *A&A*, 435, 385
- Zoccali M., Valenti E., 2016, *PASA*, 33, e025
- Zoccali M., et al., 2014, *A&A*, 562, A66
- Zwart S. F. P., Makino J., McMillan S. L. W., Hut P., 2002, *AJ*, 565, 265–279
- de Mink S. E., Pols O. R., Langer N., Izzard R. G., 2009, *A&A*, 507, L1
- van Leer B., 1977, *JCP*, 23, 276
- van Leer B., 1979, *JCP*, 32, 101
- Álvaro Segovia Otero Agertz O., Renaud F., Kraljic K., Romeo A. B., Semenov V. A., 2024, Cosmic evolution of the star formation efficiency in Milky Way-like galaxies ([arXiv:2410.08266](https://arxiv.org/abs/2410.08266)), <https://arxiv.org/abs/2410.08266>